Lidar and Microwave Radiometer Synergy for High Vertical Resolution Thermodynamic Profiling.

María Barrera Verdejo

Lidar and Microwave Radiometer Synergy for High Vertical Resolution Thermodynamic Profiling.

This research has been financed by ITARS (www.itars.net), European Union Seventh Framework Programme FP7: People, ITN Marie Sklodowska Curie Actions Programme under grant agreement no 289923.

Lidar and Microwave Radiometer Synergy for High Vertical Resolution Thermodynamic Profiling.

Inaugural-Dissertation

zur

Erlangung des Doktorgrades

der Mathematisch-Naturwissenschaftlichen Fakultät

der Universität zu Köln

vorgelegt von

María Barrera Verdejo

aus Granada, Spanien

Köln

2016

Berichterstatter/in:

Prof. Dr. Susanne Crewell	Universität zu Köln
PD Dr. Ulrich Löhnert	Universität zu Köln
Prof. Dr. Bjorn Stevens	Max-Planck-Institute für Meteorologie

Tag der letzten mündlichen Prüfung: 27th of May 2016

A mi familia y a Jose. Ellos ya saben el resto.

Nothing in life is to be feared.
It is to be understood.
Now is the time to understand more,
so that we may fear less.

Marie S. Curie

Foreword

Planet Earth is simply fascinating, exhibiting countless ways of life. As a result of evolution, they fit and function seamlessly, in equilibrium. Earth's arrangement and complexity allow us to inhabit this place. Three large subsystems form this planet: its solid part (lithosphere), which is mainly covered by water (hydrosphere) and the gaseous component (atmosphere), which surrounds the two other. The three of them are strongly interrelated and their current configuration permit *life* on Earth.

For example, have you ever wondered what planet Earth would look like without atmosphere? For sure, it would be very different. And most probably, life as it is understood nowadays, would not be possible at all. The reason for that is simple: this most external layer is the *blanket* that tucks our planet. It creates a closed thermodynamic system that avoids icy nights and extremely hot days. In addition, thanks to the ozone layer, most of the ultraviolet radiation emitted by the Sun is absorbed. The atmosphere also acts as shield against meteorites. What else can we ask for? We owe a lot to our atmosphere.

More technically, the atmosphere is a *thin* shell around planet Earth that has a thickness greater than 100 km and a mass of $\sim 5.1 \cdot 10^{18}$ kg. It might be surprising to learn that 75% of the atmospheric mass is concentrated in the lowest ~11 km: the troposphere, which contains the 99% of the total atmospheric water vapor. In addition, the strongest atmospheric interactions take place in layers closest to the ground, where land surface energy exchanges make the full story a complex adventure. A lot of things are continuously going on in there: it is the *Times Square* of the atmosphere!

For these reasons and more, the lower troposphere awakens special interest in human beings. This interest is the basis for the current thesis, and probably the reason why we both are here: you, reading these words, and I, writing them.

Contents

Zusammenfassung

Kontinuierliche Beobachtungen thermodynamischer Vertikalprofile der Atmosphäre spielen für zahlreiche Anwendungen, wie etwa die Bestimmung der atmosphärischen Stabilität oder der Wolkenbildung, eine wichtige Rolle. Heutzutage stehen zahlreiche bodengebundene Sensoren zur Verfügung, um diese Vertikalprofile abzuleiten. Allerdings ist keines dieser Instrumente momentan in der Lage, gleichzeitig sowohl eine hohe vertikale und zeitliche Auflösung über den gesamten Höhenbereich zu gewährleisten, als auch bei allen Wetterbedingungen verlässliche Messwerte zu liefern. Aus diesen Gründen wurde in der Atmosphärenwissenschaft im letzten Jahrzehnt vermehrt der Fokus auf die Nutzung von Synergien verschiedener Instrumente gelegt, um die Qualität und Nutzbarkeit bestehender Messungen zu verbessern. Die hier vorgelegte Doktorarbeit stellt ein Verfahren vor, welches die Synergie von Mikrowellenradiometer (MWR) und Lidar nutzt, um spezifische Einschränkungen der einzelnen Messverfahren zu überwinden. Lidarmessungen sind in der Lage, Profile der Temperatur und des Wasserdampfs mit hoher vertikaler Auflösung zu liefern. Jedoch sind die Messungen beschränkt bezüglich der maximalen Messhöhe, bedingt durch die Problematik der Überlappungsfunktionen (OVF) und Beeinträchtigungen durch Sonnenlicht und Wolken. Dem gegenüber erlauben MWR die Ableitung von Temperatur- und Wasserdampfprofilen und Informationen über Wolken aus dem gesamten Troposphärenbereich, allerdings mit geringer vertikaler Auflösung. Der in dieser Arbeit vorgestellte Retrieval-Algorithmus „Lidar and Microwave Synergetic Optimal Atmospheric Profiler (LIME SOAP)" kombiniert die Beobachtungen dieser zwei Messgeräte basierend auf der sogenannten „Optimal Estimation" Methode (OEM). Der wesentliche Vorteil dieser Methode im Gegensatz zu anderen Ansätzen, wie etwa neuralen Netzen, Kalman-Filtern, usw., besteht darin, dass die OEM eine Fehlerabschätzung des abgeleiteten atmosphärischen Produktes erlaubt. In LIME SOAP werden Beobachtungen, d.h. MWR-Helligkeitstemperaturen und Lidar-Wasserdampfmischungsverhältnisse und/oder Temperaturprofile, mit a priori-Informationen der Atmosphäre kombiniert, wobei die Unsicherheiten in beiden Quellen berücksichtigt werden. Die

Methode wurde auf zwei unterschiedliche Datensätze angewendet, um vertikal hochaufgelöste Profile der absoluten Feuchte (AH), Temperatur (T), relativen Feuchte (RH) und Flüssigwasserpfad (LWP) abzuleiten. Ein bodengebundener Datensatz wurde während einer zweimonatigen Messkampagne in Deutschland aufgenommen. Ein zusätzlicher Flugzeugdatensatz entstand während einer Kampagne über dem tropischen und subtropischen Atlantik. Für alle erzeugten Retrievals ergaben die Untersuchungen des theoretisch erwartbaren Fehlers und der Freiheitsgrade des Signals, dass die Informationen der beiden Instrumente mit dieser Methode optimal kombiniert werden konnten. Des Weiteren konnte die Vertikalauflösung des abgeleiteten Produkts durch die MWR-Lidar-Synergie im Vergleich zum Einzelinstrument verbessert werden. In verschiedenen Experimenten wurden die Verbesserungen durch die Instrumentensynergie im Vergleich zu den Resultaten der einzelnen Messgeräte analysiert. Die Resultate für einen zweimonatigen, bodengebundenen Datensatz zeigen beispielsweise, dass der durchschnittliche theoretische Fehler im absoluten Feuchteprofil bei der LIME SOAP-Methode um 60% (38%) reduziert werden konnte in Bezug auf Resultate, welche ausschließlich MWR (Raman Lidar) Daten nutzen. Der Fehler der Temperaturmessung konnte um 47.1% (24.6%) reduziert werden im Vergleich zu den Methoden mit ausschließlich MWR (Raman Lidar), wobei die Profile nahegelegenen Radiosondenaufstiege als Referenz herangezogen wurden. Bei der Ableitung der RH wurden Korrelationen zwischen T und AH miteinbezogen, was zu Verbesserungen im abgeleiteten RH Profil führte im Vergleich zum RH-Profil basierend auf einer unabhängigen Ableitung von T und AH. Des Weiteren konnte gezeigt werden, dass das T Profil aus dem Raman Lidar nicht unbedingt notwendig für die abgeleiteten T- und RH-Profile ist, sondern dass bereits das T Profil aus den MWR-Messungen für die durchgeführten Fallstudien zu zufriedenstellenden Ergebnissen führt. Bei der Messgeometrie mit Messflugzeugen wie etwa HALO, liegt der nicht überlappende Messbereich des Lidars in der oberen Troposphäre, also in einem Bereich mit generell geringem Wasserdampfgehalt. Daher erzielen die MWR Messungen in dieser Region ohne Lidardaten einen geringeren positiven Effekt verglichen mit der bodengebundenen Messanordnung. Die Vorteile der Sensorkombination konnten in dieser Arbeit klar demonstriert werden, wobei sich die größten Verbesserungen in Höhenbereichen ergaben, in denen Lidarmessungen nicht verfügbar waren. In Bereichen, in denen beide Messgeräte Daten lieferten, dominierten die Lidarmessungen die kombinierten abgeleiteten thermodynamischen Profile.

Abstract

Continuous monitoring of thermodynamic atmospheric profiles is important for many applications, e.g. assessment of atmospheric stability and cloud formation. Nowadays there is a wide variety of ground-based sensors for atmospheric profiling. Unfortunately there is no single instrument able to provide a measurement with complete vertical coverage, high vertical and temporal resolution, and good performance under all weather conditions, simultaneously. For this reason, in the last decade instrument synergies have become a strong tool used by the scientific community to improve the quality and usage of the atmospheric observations. The current thesis presents the microwave radiometer (MWR) and lidar synergy, which aims to overcome the specific sensor limitations.

On the one hand, lidar measurements can provide water vapor or temperature measurements with a high vertical resolution albeit with limited vertical coverage, due to overlapping function (OVF) problems, sunlight contamination and the presence of clouds. On the other hand, MWRs receive water vapor, temperature and cloud information throughout the troposphere though their vertical resolution is poor. The retrieval algorithm combining these two instruments is called Lidar and Microwave Synergetic Optimal Atmospheric Profiler (LIME SOAP) and is based on an Optimal Estimation Method (OEM). The main advantage of this technique with respect to other retrieval algorithms, e.g. neural networks, Kalman filters, etc., is that an OEM allows for an uncertainty assessment of the retrieved atmospheric products.

LIME SOAP combines measurements, i.e. MWR brightness temperatures and lidar water vapor mixing ratio and/or temperature profiles, with a priori atmospheric information taking the uncertainty of both into account. The method is applied to two different scenarios, i.e. ground based measurements during a two months campaign in Germany, and airborne measurements over tropical and subtropical Atlantic Ocean, for retrieving high vertical resolution profiles of absolute humidity (AH), temperature (T), relative humidity (RH) and liquid water path (LWP). For all retrievals, the studies in terms of theoretical error and degrees of freedom per signal reveal

that the information of the two sensors is optimally combined. In addition, the vertical resolution of the products is improved when the MWR+lidar combination is performed with respect to the instruments working alone.

Different experiments are performed to analyze the improvements achieved via the synergy compared to the individual retrievals. Results show that, for example, when applying the LIME SOAP for ground-based AH profiling, on average the theoretically determined absolute humidity uncertainty is reduced by 60% (38%) with respect to the retrieval using only-MWR (only-Raman lidar) data, for two-months data analysis. For temperature, it is shown that the error is reduced by 47.1% (24.6%) with respect to the only-MWR (only-Raman lidar) profile, when using a collocated radiosonde as reference.

When retrieving RH, correlation between T and AH is included, which leads to improvements in the retrieved RH with respect to the case when T and AH are calculated independently. In addition it is shown that the Raman lidar T profile is not essential for the T and RH retrievals and using only the MWR temperature information provides products satisfactory for the specific case study. From the airborne perspective of HALO, the lidar non-overlap region is situated in the upper troposphere, where the amount of water vapor is reduced. Thus, the MWR improvement in the *blind* lidar region has less impact than in the ground based scenario.

The benefits of the sensor combination are demonstrated, being especially strong in regions where lidar data is not available, whereas if both instruments are available, the lidar measurements dominate the retrieval.

1

Introduction

Climate change is one of the largest challenges for mankind. Still, the changes to be expected in the distribution of temperature and precipitation strongly vary between different climate models. How clouds and the formation/suppression of precipitation will develop is a long lasting question and a major reason for the differences between models. But which — if any — is giving the truth? What role do environmental conditions like water vapor and temperature play?

In order to answer these questions, it is essential to better understand the atmospheric phenomena. Observations are essential for the understanding of atmospheric processes, since for a long time hardly any quantitative measurements of atmospheric parameters existed. Because *in situ* measurements are not possible everywhere, one must resort to remote sensing techniques, whose development has been fostered only in recent times by technological progress.

1.1 Motivation

Water vapor and temperature are essential variables required for the understanding of many atmospheric phenomena. According to Hoff and Hardesty (2012), temperature and moisture profiling in the lower troposphere are central to some of the most important research and operational goals in atmospheric and Earth system studies, mesoscale numerical weather prediction, and monitoring of regional climate variability. Water vapor is not only the most important greenhouse gas, but also its radiative properties influence the planetary albedo, and hence Earth's surface temperature, as well as the hydrological cycle and the thermodynamic structure of the troposphere (Stevens and Bony, 2013).

Already twenty years ago, Crook (1996) stated that variations in boundary layer temperature and moisture within 1° C and 1 g/kg respectively, can make the difference in prediction models between no initiation and intense convection, which hints at the accuracy needed for the observations. More recent research (Hoff and Hardesty, 2012) summarizes the requirements for

measurements in order to be able to resolve short time scale processes, i.e. 30 meters in horizontal and vertical resolution, with a repeatability of 1 second and precision of 5% and 0.2 K for humidity and temperature respectively. These requirements present a challenge to tackle despite the fact that a wide variety of ground based, airborne and satellite remote sensing instruments that sense atmospheric parameters exist.

Remote sensing instruments measure passively or actively different atmospheric features in several spectral domains (infrared, visible, microwave, etc.), each providing different and complementary information about the atmospheric state. Nevertheless, even if there is a wide variety of atmospheric sensors, there is none which can provide all of the following requirements simultaneously: complete vertical coverage, high vertical and temporal resolution of the atmospheric profiles and satisfactory performance under all weather conditions. Specifically, processes on short time scales such as convection, cloud formation or boundary layer turbulence cannot be resolved completely by any single instrument alone. In order to overcome this limitation, the scientific community started in the last decade to perform instrument synergies, merging data from different sensors.

In the present thesis, the synergy between two different remote sensing instruments is presented: lidar and Microwave Radiometer (MWR). They are used to retrieve temperature and humidity atmospheric profiles. Both instruments present several advantages and drawbacks. Nevertheless, it is possible to overcome some of the disadvantages in the single devices and enhance their benefits by combining them in an optimal and new retrieval algorithm: the Lidar and Microwave Synergetic Optimal Atmospheric Profiler (LIME SOAP).

On the one hand, lidar systems provide highly vertically resolved measurements of atmospheric humidity profiles. For this reason, lidars have become a strong tool for active observations in the last years and new retrieval algorithms optimally exploiting the information content are developed (Sica and Haefele, 2015; Povey et al., 2014). However, the lidar technique presents important weaknesses, which might hinder its operational application. For example, lidars cannot provide information above and within optically thick clouds, as the radiation emitted by the lidar quickly extinguishes once the laser beam reaches a cloud. Moreover, day time measurements can be affected by background solar radiation, which strongly reduces the vertical range of the measurements. The continuous and effective detection of lidar signals, which are typically weak, requires robust and stable receiving systems. Daytime operation is not possible in all cases and requires the use of powerful lasers whose continuous operation is technically demanding. Additionally, most of the lidars need to be calibrated. This calibration is usually performed based on the use of radiosounding data, which presents some caveats. First, the balloon might measure a different air volume due to its drift. Second, it implies both a high human and instrument cost. The calibration of the lidar is a key point that still represents a scientific challenge (Foth et al., 2015). In addition, the information of the layers closest to the instrument typically cannot be used, due to the presence of a blind region associated with the overlap function (OVF) of the

system.

On the other hand, the MWR allows continuous passive data acquisition and it is a robust operational instrument (Rose et al., 2005), measuring unattended in a 24/7 mode. In contrast to lidars, the instrument offers a much more limited vertical resolution of the retrieved atmospheric profiles, especially in higher layers of the atmosphere (i.e. 1 km away from the instrument) (Löhnert et al., 2007). Nevertheless, MWR performs best for measurements close to the instrument, where there are no lidar data. MWR also provides accurate integrated quantities such as Integrated Water Vapor (IWV) or Liquid Water Path (LWP) . The calibration of this instrument is performed with internal references with known temperature (hot load-cold load) or by observing the atmosphere under different elevation angles (i.e. sky tipping) (Maschwitz et al., 2013). Another advantage of the MWR is the capability of measuring in almost all weather conditions (also cloudy cases) except for rainy scenarios, where the received signal must be discarded in most of the cases.

1.2 State of the art

Several ground-based synergies have been performed previously. For example, Stankov (1998) combined ground- and space- base remote sensing measurements, i.e. passive radiometric, radar, and in situ observations, to estimate the temperature and humidity profiles. Her retrieval has two stages, the first starting with a simple linear statistical inversion using ground-based measurements, whose result serves as a priori information for the second stage. The latter is a traditional physical one step algorithm to iteratively adapt brightness temperatures to atmospheric profiles. The author uses space-based radiance measurements from polar-orbiting satellites. When brightness temperature difference is below the instrument noise, convergence is achieved. The presented results were a real advance at that time: the retrieved temperature profiles present a bias of -0.27°C and a standard deviation of 1.56 °C.

Humidity profiles have been also retrieved by Bianco et al. (2005), combining microwave radiometry and wind profiler radar measurements. Their combination of passive and active sensors relies on the relationship between the gradients of specific humidity, potential refractivity and potential temperature in the atmosphere (Stankov et al., 2003). This technique has the advantage that it is independent from in situ measurements, relying only on remote sensing information. Nevertheless, it is limited to work well only during convective periods, when turbulence is well developed. The authors present also several unsatisfactory cases in which the combined technique did not have good performance. For the derivation of humidity profiles from the remote sensing observations, they use an analytical method, but discuss the possibility of using a statistical method similar to the one implemented by Stankov (1998), which might be more robust. In addition, they use the integrated water vapor content by the MWR as constraint for their retrievals.

The two latter retrieval techniques present some weaknesses: first, the retrieved atmospheric profile is not optimally calculated and second, the retrieval methods do not allow a posteriori uncertainty assessment of the result.

A synergetic optimal method, based also on the OEM, was performed by Löhnert et al. (2004). The authors describe the Integrated Profiling Technique, in which they retrieve physically consistent profiles of temperature, humidity, and cloud liquid water content. They achieve it by combining ground-based multichannel microwave radiometer, cloud radar, lidar-ceilometer and ground-level measurements of standard meteorological properties. Nevertheless, in this study the vertical resolution of the retrieved humidity profiles is restricted to the MWR information content.

Not only from the ground based perspective, instrument synergies are also performed for airborne and satellite applications. For example, Delanoe and Hogan (2008), where the authors combine ground-based and spaceborne radar, lidar and infrared radiometer. Their method is also based on an OEM for retrieving profiles of extinction coefficient, ice water content and effective radius in ice clouds. The algorithm uses the radar and lidar data together to find the combination of microphysical variables that best forward models the observations. They test it on synthetic profiles generated from aircraft microphysical observations and on real ground-based data. Unfortunately, the instruments they use do not provide any information on the humidity and temperature profiles, though the authors suggest in their conclusions that the inclusion of more observations could be incorporated into their scheme for such aim, which would allow the full cloud profile to be retrieved.

A method to combine Raman lidar (RL) and MWR was also proposed by Han et al. (1997), where the authors developed a two-stage algorithm to derive water vapor atmospheric profiles. In the first stage, a Kalman filtering algorithm was applied using surface in situ and RL measurements. In the second stage, a statistical inversion technique was applied to combine the Kalman retrieval with the integrated water vapor of a two-channel MWR and climatological data. Their method showed that the synergy of these two sensors compensates for the individual sensor's drawbacks. A continuation of this work was carried out by Schneebeli (2009). The author still followed the Kalman filter two-stage configuration, substituting the second step for an inversion based on an OEM. The observation vector in the OEM consists of the MWR brightness temperatures, and the lidar profile resulting from the Kalman filter is introduced as a priori information. The method is applied to synthetic measurements and only one real measurements case study. In both Han et al. (1997) and Schneebeli (2009), only water vapor profiles were retrieved.

Most recently, Navas-Guzmán et al. (2014) presented the water vapor and relative humidity profiles from lidar and microwave radiometry. The authors use an iterative method to calibrate the water vapor mixing ratio profiles retrieved from Raman lidar measurements with the MWR. In addition they present a method to combine these water vapor Raman lidar profiles with temperature profiles retrieved with the MWR. Their results are presented for 1 year data in

Granada, though their lidar only measures during night-time. However, their method does not combine the MWR and lidar measurements in an optimal way and does not provide an a posteriori uncertainty assessment.

1.3 Goals of the thesis

In this thesis a new flexible method to combine lidar and MWR measurements is developed for the retrieval of thermodynamic profiles: LIME SOAP. The algorithm is a new approach based on an Optimal Estimation Method (OEM), an iterative optimal and physically consistent method which provides the most probable atmospheric state. One of the main advantages of this method with respect to other retrieval techniques is that OEM allows for the retrieval uncertainty assessment and a posteriori evaluation of the retrieval information content.

First, LIME SOAP is applied to the ground-based perspective for humidity and temperature retrievals. For that, the data collected during HOPE ($HD(CP)^2$ Observational Prototype Experiment) is used, where a multitude of ground-based remote sensing instruments for the investigation of boundary layer and cloud processes were operated (Steinke et al., 2014a; Behrendt et al., 2015; Foth et al., 2015). Second, LIME SOAP is applied to the airborne perspective of HALO (High Altitude and Long range research Aircraft) (Mech et al., 2014), which flew during the NARVAL (Next-Generation Aircraft Remote sensing for Validation Studies) campaign.

The main goal of this thesis is to quantify the value of the MWR and RL synergy for different viewing geometries and atmospheric conditions. For said purpose, in this work the details of how to perform an optimal MWR and RL synergy are explained. After the overview provided by the introduction, chapter 2 gives a general description of the field campaigns and the instruments used in this thesis. The MWR working principle and the radiative transfer equation are explained (section 2.2.1) together with the characteristics of the HATPRO (Humidity and Temperature Profiler, section 2.2.2) and HAMP (HALO Microwave Package, section 2.2.3) MWRs, operated during HOPE and NARVAL campaigns respectively. Two types of lidar are used and presented in this thesis: a Raman lidar, i.e. BASIL (section 2.3.2), and a Differential Absorption lidar (DIAL), i.e. WALES (section 2.3.3). Section 2.4 explains the auxiliary data sources, e.g. reanalysis model data or radiosondes, which serve for retrieval evaluation or a priori information calculation in further chapters.

Chapter 3 provides a description of the synergetic algorithm. It first starts presenting the general theory of an OEM, describing what are its main parts: a priori information, instrument measurements, forward models and the retrieval information content assessment, i.e. averaging kernels, theoretical error and degrees of freedom. The application of the OEM to the lidar and MWR synergy for thermodynamic profiling is LIME SOAP. Section 3.2 describes the details on how LIME SOAP components are modified, depending on the application, i.e. the retrieval of different atmospheric variables, atmospheric scenarios or instrument geometry. Questions

related to the definition of a priori information or a forward model for each specific LIME SOAP application, are addressed in this part.

The application of LIME SOAP to the absolute humidity (AH) retrievals under clear sky conditions from the ground based perspective are presented in chapter 4. In order to demonstrate the MWR+lidar synergy, retrievals comparing the single instrument performance (i.e. LIME SOAP using only-RL data or using only-MWR data) to the combination of both (i.e. LIME SOAP using MWR+RL information) are presented. A case study profile first illustrates the synergy benefit in section 4.1. After that, section 4.2 presents the statistical assessment for the results of applying LIME SOAP to the complete HOPE period.

Because the two instruments have the capability of providing temperature (T) information, LIME SOAP is also applied to the T retrieval. That leads to the possibility of retrieving relative humidity (RH) information, which becomes especially valuable in the vicinity of clouds to study cloud formation. The T retrieval is described in chapter 5, together with the RH calculation (section 5.2). Comparisons to RS highlight the synergy benefits for T retrievals in section 5.1.1, followed by statistical assessment presented for a set of ~150 retrieved profiles (section 5.1.2).

In addition, by including some information on cloud geometry, LIME SOAP can be extended to cloudy conditions, where the strongest synergy benefit is expected. The evaluation of the method applied to a simple cloudy scenario is described in chapter 6, where the MWR+RL signal turns essential to retrieve complete vertical T, AH and RH profiles. Results for a time series of these thermodynamic profiles are discussed in section 6.2.1. To provide information on the amount of water in the cloud, the liquid water path (LWP) is retrieved, together with integrated water vapor (IWV) calculations (section 6.2.2).

Completed the full ground based scenario, the synergy applied to the airborne perspective of HALO is exploited. The results of this application are discussed in chapter 7, where comparisons with auxiliary measurements and theoretical a posteriori studies show the synergy benefits. Finally chapter 8 presents an overview of the thesis, highlighting the main results and opening new ideas for further studies.

2

Instrumentation and data

Two major field campaigns offer the opportunity to apply and test LIME SOAP using lidar and microwave radiometer (MWR) data. Firstly HOPE, deployed in Germany during spring 2013. Second, the NARVAL-South experiment, carried out flying through the tropical regions in December 2013. The two field experiments provide both lidar and MWR measurements, as well as auxiliary data for evaluation.

Firstly, this chapter will present these two field experiments (section 2.1). Second, the instruments used in this thesis, focusing on the MWR (section 2.2) and lidar systems (section 2.3), whose working principle will be described in more detail, and completed with auxiliary data (section 2.4).

2.1 Measurement campaigns

2.1.1 *HD*(*CP*)^2 Observational Prototype Experiment: HOPE

HOPE was a field campaign in Nordrhein-Westfalen, Germany, held from April to June 2013, as part of the HD(CP)2 project [1]. The main goal of the campaign was to provide a complete high resolution picture of the clouds' lifetime and evolution. During the measurement period, three supersites operated, distributed in the surroundings of Forschungszentrum Jülich (50.905N, 6.411944E), see figure 2.1. The supersites were situated at ~4 km distance from each other. Each of them was composed of numerous remote sensing instruments, coordinated with different scanning strategies that allow the 3D study of clouds. A total of five Humidity and Temperature Profiler (HATPRO) radiometers and 3 lidar systems were operated, among other instruments.

[1] HD(CP)2 (High Definition Clouds and Precipitation for Climate Prediction) is a major German-wide research initiative to improve the understanding of cloud and precipitation processes and their implication for climate prediction. For more information: `http://hdcp2.zmaw.de`).

At the permanent supersite JOYCE (Jülich ObservatorY for Cloud Evolution) (Löhnert et al., 2014), measurements by the University of Basilicata Raman Lidar system (BASIL) and a HATPRO MWR were carried out. Auxiliary data from other instruments is available, such as ceilometers, cloud radar, micro-rain radar, total-sky imager, etc. Furthermore, more than 200 radiosondes (RS) were launched only ~4 km away from JOYCE, at the KITCube supersite. The radiosondes were launched at least twice a day: at 11 and 23 UTC, and additionally launched during intensive observation periods.

Section 2.2.2 will describe the HATPRO radiometer in detail. In section 2.3.2, the Raman lidar (RL) BASIL will be presented. The additional data used for validation of the algorithm is described in section 2.4.

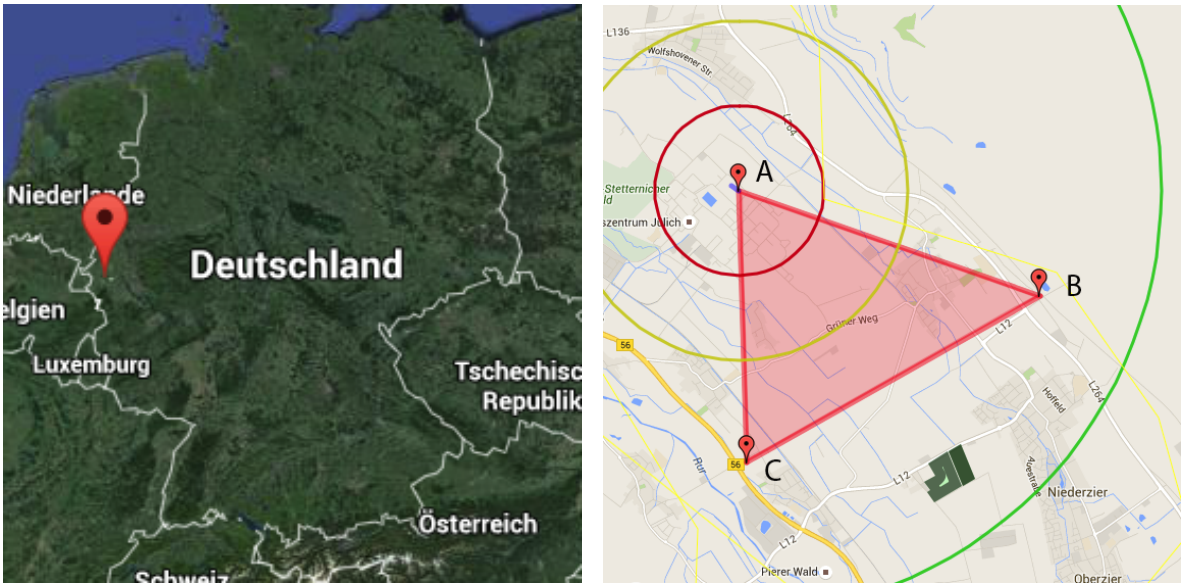

(A) (B)

Figure 2.1: (A) The JOYCE observatory at Jülich, Germany. (B) The three supersites operating during HOPE. A: JOYCE, B: KITCube & UHOH and C: LACROS. The red, yellow and greeen rings represent the 1 km, 2 km and 5 km distance around JOYCE, respectively. *Source: Google maps.*

2.1.2 Next-Generation Aircraft Remote sensing for Validation Studies: NARVAL

The NARVAL campaign is an airborne mission, which aims for a better understanding of prevalence and structure of clouds and precipitation from shallow convection (Klepp et al., 2014). The research airplane HALO [2] (High Altitude and Long range research aircraft) (see figure 2.2) was equipped with a full array of state of the art remote sensing instruments (lidar, radiometers, radar, optical spectrometers), in situ sensors and additional instrumentation, e.g. dropsondes. The first mission is divided in two experiments with a total of 15 research flights: NARVAL-South, with

[2] http://www.halo.dlr.de/

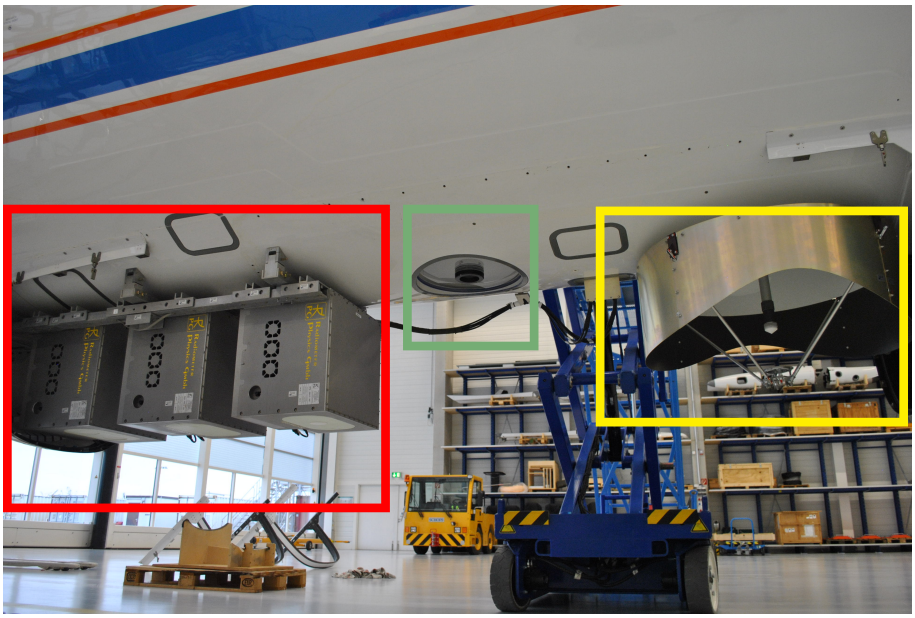

(A)

(B)

Figure 2.2: (A) Open HALO bellypod, showing from left to right: the MWR (passive HAMP) in red, the lidar (WALES) in green and the radar (active HAMP) in yellow. (B) closed bellypod for flight operation. *Source: Friedhelm Jansen, Max Planck Institute for Meteorology Hamburg.*

focus on the subtropical region east of Barbados, in December 2013; and NARVAL-North, in the vicinity of Iceland in January 2014. The first is intended to study the trade wind regions; the second focuses on postfrontal convective clouds and precipitation. In this study, the data collected during NARVAL-South has been used.

In total 8 research flights were carried out during NARVAL-South, between Oberpfaffenhofen

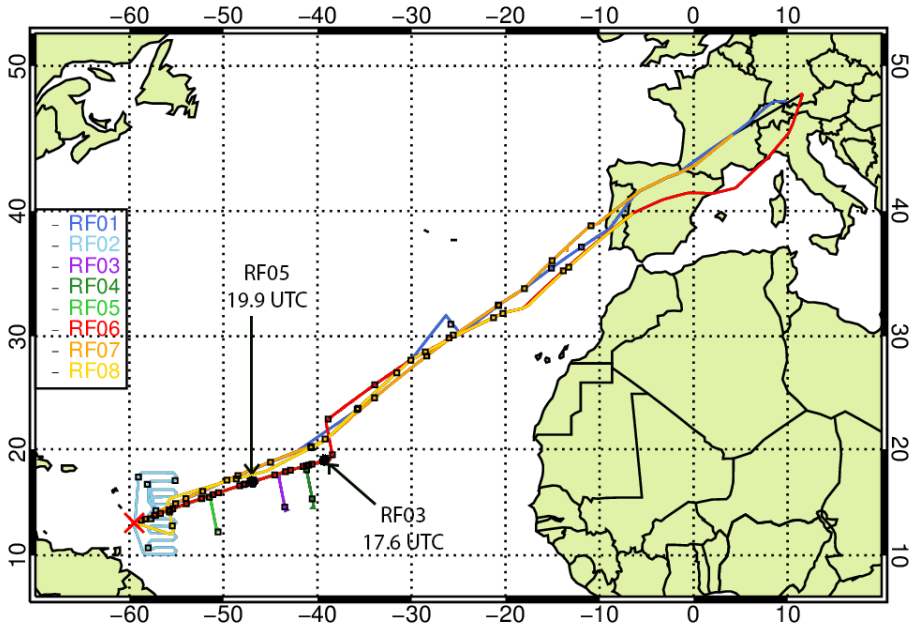

Figure 2.3: The NARVAL South mission flight pattern of the eight research flights over the North Atlantic tradewind region between Europe and Barbados. The squares represent the launched dropsondes and the red cross, the location of Barbados. Two dropsondes are highlighted, which will be used in further chapters. *Source: S. Schnitt, personal communication.*

(Germany) and the airport of Barbados, with 65-70 flight hours. Figure 2.3 gives an overview of the flights during the experiment. The goal of NARVAL-South was to fly over the northeast Atlantic trades to measure their evolution, compiling remote sensing measurements. Several flight legs were dedicated to satellite underflight for Cloudsat (Stephens et al., 2002) validation. Additionally, 75 dropsondes were launched. More information on the campaign is found in Klepp et al. (2014). In this thesis, the radiometer HAMP (explained in section 2.2.3), the lidar WALES (section 2.3.3) and the dropsondes (section 2.4.1) will be used.

2.2 Microwave radiometer

The microwave radiometer is a passive instrument, which measures thermal radiation emitted by the atmosphere in the microwave spectrum from 20-200 GHz (15-1.5 mm). Despite the fact that a MWR is a robust instrument that can measure in almost all weather scenarios, it presents a major drawback with respect to active instruments for profiling: its low vertical resolution, i.e. only 2 pieces of information per profile for water vapor (Löhnert et al., 2007).

The radiatively significant atmospheric components in the microwave regime are gas molecules and water, in the form of cloud droplets, precipitation or ice crystals. The radiation field is determined by emission and extinction processes while propagating through the atmosphere. The

extinction processes include absorption and scattering (radiation is redirected out of the propagation direction). The radiative transfer equation (RTE) describes the behavior of radiation propagating through the atmosphere. Based on the RTE, and measuring the radiation received by the MWR, one can analyze the atmospheric state. The RTE theory will be explained in this section, followed by the details of the two different MWR used in the next chapters.

2.2.1 Radiative transfer

The interactions among microwave radiation and atmospheric constituents are described with the RTE, whose theory is well described in the textbooks by Liou (1980) and Petty (2006) and will be explained shortly in the following.

Thermal emission is transmitted through the atmosphere, suffering extinction. The total atmospheric extinction is quantified by the extinction coefficient β_e (in m^{-1}), which accounts for the effects of atmospheric absorption (β_a) and scattering (β_s). The extinction coefficient has a frequency dependence in the microwave regime as depicted in figure 2.4. The peaks in the figure correspond to the absorption lines of the water vapor (around 22.235 and 183 GHz) and the oxygen absorption complex (around 60 and 118 GHz).

Because the scattering efficiency depends on the ratio of wavelength to particle size, the atmosphere can be approximated as a non-scattering medium for frequencies smaller than 100 GHz. The only exception occurs in the presence of *large* precipitation particles (Janssen, 1993). By neglecting scattering, the radiation scenario is simplified to one dimension.

Consider the propagation of monochromatic radiation, with frequency ν, through an infinitesimal layer of air, whose thickness is dR. Its intensity of radiation I_ν (in $\frac{W}{m^2 s^{-1} sr}$), which for the sake of simplicity will be referred as I in the following, will be reduced by absorption:

$$dI_{abs} = -\beta_a \cdot I \cdot dR \tag{2.1}$$

According to Kirchhoff's Law, the absorption of any medium in local thermodynamic equilibrium is equal to the emissivity of the same matter. So one can expect the layer of air to emit radiation dI_{emi}. Thus, a *net* change in the radiation intensity through the infinitesimal layer of air can be then written as:

$$dI = dI_{abs} + dI_{emi} = -\beta_a \cdot I \cdot dR + \beta_a \cdot B(T) \cdot dR \tag{2.2}$$

or

$$dI = -\beta_a \cdot (B(T) - I) \cdot dR \tag{2.3}$$

which is the most general monochromatic form for the RTE, for a non-scattering medium. This equation describes the change in radiation intensity at a frequency ν, while traversing an absorptive medium, and is known as the *Schwarzschild's Equation* (Petty, 2006). In equation

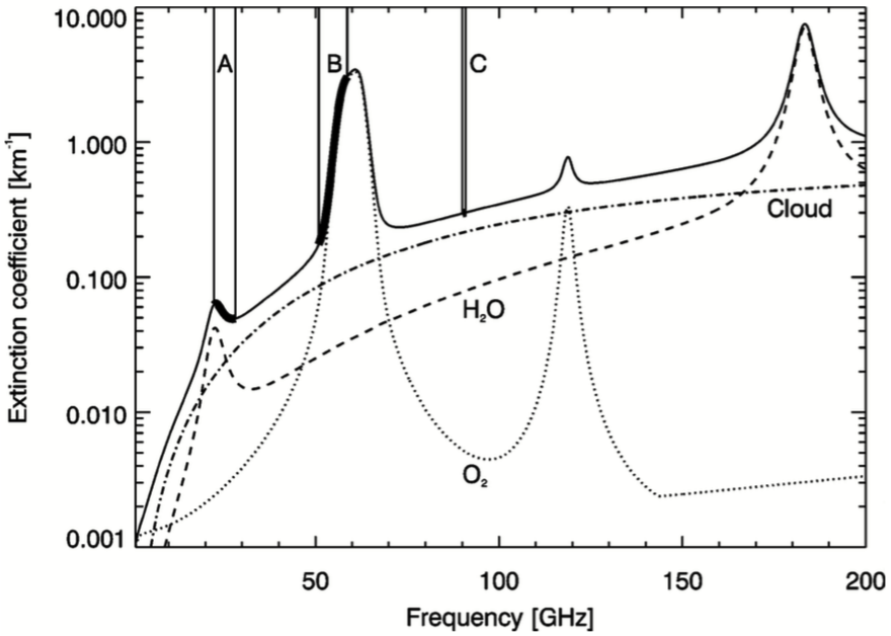

Figure 2.4: Extinction coefficient in the microwave spectrum at 850 hPa. The dashed line shows the water vapor contribution, the dotted line the oxygen contribution, and the dotted-dashed line the theoretical cloud liquid contribution of a cloud with $0.2gm^{-3}$ LWC, using the US-standard atmosphere. The solid line is the sum of all contributions. (Löhnert et al., 2004)

2.3, $B(T)$ denotes the Planck function, which represents the thermal emission of a blackbody (emissivity $\epsilon = 1$) at temperature T:

$$I = \epsilon \cdot B(T) \approx B(T) = \frac{2h\nu^3}{c^2} \frac{1}{e^{\frac{h\nu}{k_b T}} - 1} \tag{2.4}$$

where h is the Planck constant ($h = 6.626 \cdot 10^{-34}\ \frac{m^2 kg}{s}$), c is the speed of light in vacuum ($c \approx 3 \cdot 10^8 m/s$) and k_b is the Boltzmann constant ($k_b = 1.3810^{-23}\ \frac{m^2 kg}{sK}$). Equation 2.4 relates the physical temperature to the intensity of radiation of an object , as a function of the radiation frequency. Because in the microwave regime the Rayleigh-Jeans approximation is valid ($\frac{h\nu}{k_b T} \ll 1$), one can approximate eq. 2.4 as follows:

$$B(T) = \frac{2hk_b\nu^2 T}{c^2} \tag{2.5}$$

which reveals a linear relation between the physical temperature and the blackbody radiation. Therefore, the radiation intensity I is often scaled to an equivalent blackbody temperature, or brightness temperature T_B:

$$T_B \equiv B^{-1}(I) \tag{2.6}$$

where B^{-1} is the inverse of the Planck's function solved for T assuming that the observed medium is a black body. This is the definition of the Planck equivalent brightness temperature, which in the Rayleigh-Jeans limit is equal to:

$$T_B = \frac{\lambda^2}{2k_b} I \tag{2.7}$$

In practice, there are deviations between both, however the radiative transfer code used here considers the exact Planck solution. Thus, for a ground-based instrument receiving downwelling thermal radiation T_{B_g}, using eq. 2.7 in 2.3 and integrating from ground to space, one can write the RTE as:

$$\boxed{T_{B_g} = T_{B_{cos}} e^{-\tau} + \int_0^\infty \beta_a(R) T(R) e^{-\tau(R)} dR} \tag{2.8}$$

which is the RTE for measurements taken from the ground-based perspective, under the assumption of plane-parallel atmosphere. $T_{B_{cos}}$ is the cosmic background radiation ($\sim 2.73K$ (Janssen, 1993)), $T(R)$ is the physical temperature. The term $e^{-\tau}$ is the transmission term $T_{trans}(R)$, and τ is the optical depth defined as:

$$\tau(R) = \int_0^R \beta_a(R')dR' \tag{2.9}$$

When the instrument is airborne based, the perspective and so the RTE changes. In addition to the upwelling radiation from the Earth surface and atmospheric components, also downwelling atmospheric radiation reflected by the surface needs to be considered. The MWR on HALO flies over the ocean, which has typically an emissivity of $\epsilon \approx 0.5$. ϵ depends on the frequency, the sea surface temperature (SST) and the surface wind. Combining all the radiation terms, the total brightness temperature at the altitude h at which an aircraft flies, is calculated by:

$$\boxed{T_{B_{airborne}}(h) = T_{B_{sea}}(h) + T_{B_g}(\tau = \tau_1) \cdot e^{-\tau_2} \cdot (1 - \epsilon)} \tag{2.10}$$

with $T_{B_{sea}}(h)$ representing the thermal radiation emitted by the sea surface and the atmospheric layers, attenuated up to the aircraft:

$$T_{B_{sea}}(h) = \epsilon \cdot SST \cdot e^{-\tau_2} + \int_h^0 \beta_a(R) T(R) e^{-\tau(R)} dR \tag{2.11}$$

where τ_1 and τ_2 correspond to the optical depths in the path from infinite to the surface and from h to the surface, respectively. An example of the τ frequency dependence will be illustrated in figures 2.5 and 2.6 for the MWRs used in this thesis.

The form of the RTE in equation 2.8 will be used in chapters 4 to 6, for the ground-based perspective. The RTE in equation 2.10 will be used in chapter 7, for the HALO scenario. In the following, the MWR instruments used in the two different scenarios (ground- and airborne-based) are presented.

2.2.2 Humidity and Temperature Profiler: HATPRO

The microwave radiometer profiler HATPRO (Rose et al., 2005) was manufactured by Radiometer Physics GmbH, Germany (RPG) . It is a network-suitable microwave radiometer that allows to accurately retrieve at high temporal resolution (1 s) Liquid Water Path (LWP) and Integrated Water Vapor (IWV), with accuracies of 20 g/m^2 and 0.5-1 kg/m^2, respectively (Löhnert and Crewell, 2003). It measures radiation in the atmosphere in two frequency bands in the K- and V-band. The seven channels of the K band contain information about the vertical profile of humidity through the pressure broadening of the optically thin 22.235-GHz H_2O line and contain also information for determining liquid water path. The seven channels of V-band, in the O_2 complex (60 GHz), contain information on the vertical profile of temperature resulting from the homogeneous mixing of O_2 throughout the atmosphere (Löhnert et al., 2009). The weighting functions for the K- and V-bands are presented in figure 2.5, showing the altitude sensitivity of all the 14 HATPRO channels. The instrument typically measures pointing zenith, but has also the capability of scanning. The inclusion of the angular information of the TB increases the vertical information content of the temperature retrieval, specially in the boundary layer (Crewell and Löhnert, 2007).

The voltages measured by the instrument need to be calibrated to an equivalent brightness temperature. An absolute calibration is performed taking a cold and a hot load as references, which are assumed to be ideal black bodies. The cold body is a liquid-nitrogen-cooled load that is attached externally to the radiometer box during calibration, which can be considered as a black body at the LN_2 boiling temperature of approximately 77 K. This standard, together with an internal ambient black body load (at ~ 300 K), is used for the absolute calibration. The TBs absolute uncertainty is ±0.5 K at the liquid nitrogen boiling temperature at all frequency channels, and increases towards colder T almost linearly (Küchler et al., 2016). In addition, a calibration by tip-curve observations is performed, whereby the instrument collects observations for the optically thin K-band channels at different elevation angles (Han and Westwater, 2000). The reliability of sky tipping calibrations will strongly depend on how good the assumption of a horizontally stratified atmosphere is (Turner et al., 2007). Further details on the calibration procedures of the instrument can be found in Maschwitz et al. (2013) and Küchler et al. (2016).

The receiver antenna beam widths can be considered infinitively small (pencil beam approximation), as discussed in Löhnert and Maier (2012). The radiometer radome is protected from rain, snow and hail: a blower system is installed to dry it and prevent the formation of dew or any possible condensation. The instrument receiver needs to be thermally stabilized with high accuracy (±0.1 K) for stable operation within the range of expected environmental conditions (from -30 to $+45^o$ K).

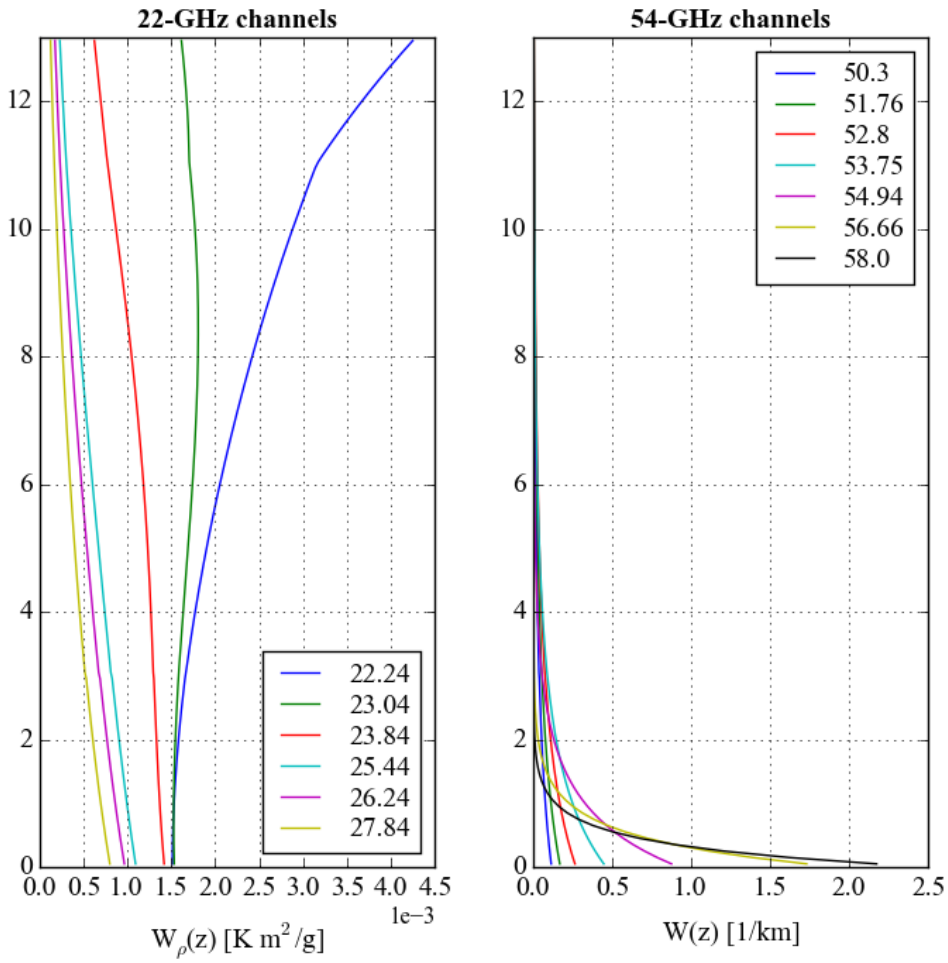

Figure 2.5: HATPRO clear sky weighting functions (zenith upward looking). Shown are the water vapor (left) and the temperature (right) weighting functions. The US 1976 Standard Atmosphere over a black surface was assumed for the calculations. *Source: personal communication with M. Mech.*

2.2.3 HALO Microwave Package: HAMP

HAMP, the HAlo Microwave Package (Mech et al., 2014), is composed by two nadir-looking modules on board of HALO: first, the active component, which is a cloud radar at 36 GHz; second, the passive microwave radiometers with 26 frequencies at different bands between 22.24 GHz and 183.31 GHz. In this thesis, only the passive microwave radiometer module is used and will be referred in the following as HAMP.

The HAMP MWR was custom manufactured for HALO by RPG and is mounted in the HALO bellypod. It is composed of three modules. The first has receivers for the K- and V-band, similar to HATPRO, where measurements in 14 different channels are taken. The second module measures in a window channel at 90 GHz (W-band) and four channels in the 118.75 GHz (±1.4 to ±8.5 GHz) F-band, on the wing of an O_2 absorption line. The last module measures radiation in the

183.31 GHz H_2O band (±0.6 to ±12.5 GHz), i.e. the G-band. All the three modules are thermally stabilized, with an accuracy < 0.05 K over the operation regime (from -70 to +35^o K).

The channels in the K-band and G-band are used for the retrieval of water vapor profiles and its integrated value (IWV). The channels in the V-band are used for T profiling, together with the four frequency channels in the F-band. The altitude sensitivity of the HAMP channels is shown in figure 2.6, which presents their clear sky weighting functions, calculated for the US 1976 Standard Atmosphere and assuming a ceiling height of 13 km. The figure nicely shows how the two innermost V-band channels present a high sensitivity to the temperature close to the aircraft. The outer channels of the G-band are less affected by water vapor and can be assumed to be window channels (Mech et al., 2014).

A liquid nitrogen calibration of the instrument was performed before every take off and after every landing. In addition, there is an in-flight calibration with two reference targets. One is at ambient temperature, corresponding to the stabilized temperature of the receiver box, and the second is generated by an internal noise diode producing a Gaussian distributed white noise signal. The beam width measured at full width at half maximum varies depending on the wavelength from 5.0^o in the K and V bands, to 2.7^o in the 183-module. This leads to a resolution at ground between 1.4 and 0.9 km in the along-flight direction and between 1.1 and 0.6 km in the across-flight direction (considering 13 km flying altitude and 1 s integration time).

2.3 Lidar: Light Detection and Ranging

Lidar (Light Detection and Ranging) is a principle for active remote sensing measurements. A general lidar system transmits a narrow laser beam into the atmosphere and receives the scattered light back to the instrument. It can work in the ultraviolet, visible and near-infrared regimes, depending on the application. Due to historical reasons, wavelengths are preferred in the lidar community, while frequency is used in the MWR community.

Different types of lidar exist: Differential absorption lidar (DIAL) , Doppler lidar, Raman lidar, etc. according to the physical mechanism that is exploited. Below, the basic principle of a lidar system, together with the description of a Raman lidar and a DIAL is presented. In addition, the RL BASIL (section 2.3.2) and the DIAL WALES on HALO (section 2.3.3) are described. In this study, both instruments were used to measure atmospheric water vapor and only the RL measures atmospheric temperature as well.

2.3.1 Lidar theory

The basic configuration of a lidar system consists of a transmitter and a receiver. The first emits light pulses to the atmosphere, generated by a laser. The second collects the radiation backscattered from the atmosphere by a telescope. This is followed by an ensemble of filters,

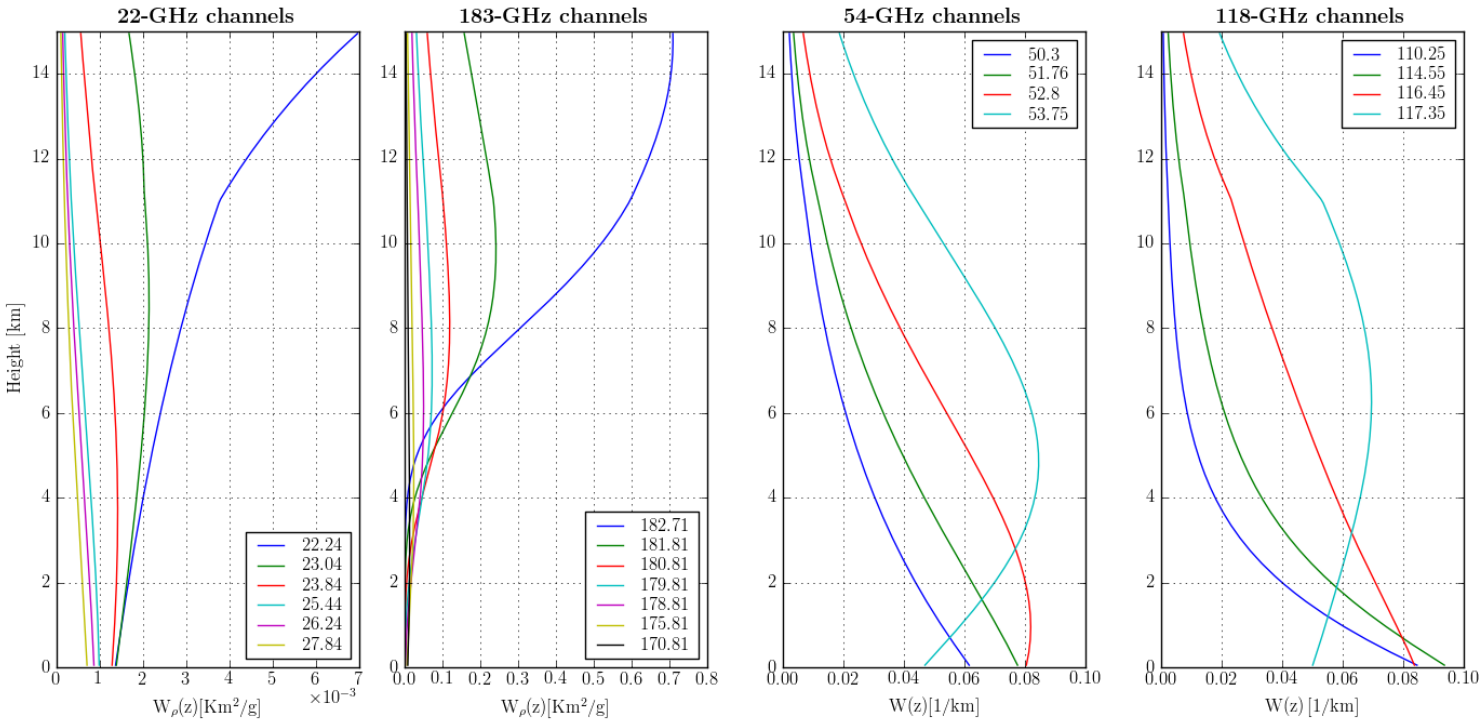

Figure 2.6: HAMP clear air weighting functions (nadir downward looking). Shown are the water vapor (two leftmost) and the temperature (two rightmost) weighting functions for a HALO ceiling height of about 13 km. The US 1976 Standard Atmosphere over a black surface was assumed for the calculations. The figure is taken from Mech et al. (2014).

which select the part of the signal under interest. The selected optical signal arrives at a detector, where it is converted to an electrical signal.

The most general form to express the power P received on a lidar system from the distance R is (Weitkamp, 2005):

$$P(R) = K \cdot G(R) \cdot \beta(R)_{\pi} \cdot T_{trans}(R) \tag{2.12}$$

where K is a factor summarizing the system performance and $G(R)$ is the range-dependent measurement geometry function (i.e. the overlapping function). These two terms depend only on the lidar system configuration. The terms $\beta_{\pi}(R)$ and $T_{trans}(R)$ are the backscatter coefficient and the transmission term at distance R, respectively.

The backscatter coefficient (in $m^{-1}sr^{-1}$) describes how much radiation is scattered towards the instrument (i.e. 180° scattering) and is frequency dependent. It is proportional to the number of scatterers in the atmosphere and to the backscattering cross section, i.e. probability of scattering in the direction of study. In the atmosphere, the emitted laser light is scattered by molecules (i.e. nitrogen and oxygen) and by particles (aerosols, water droplets, etc.).

The transmission term $T_{trans}(R)$ represents the fraction of light that arrives at the receiver after propagating from the laser to the backscattering volume and back. $T_{trans}(R)$ depends on the extinction coefficient $\alpha(R, \lambda)$[3], which accounts for the total transmission losses. The extinction coefficient includes the contributions of scattering and absorption of light by atmospheric molecules and particles. The parameters $\beta_\pi(R)$ and $T_{trans}(R)$ are the ones providing the information on the atmospheric state, since they depend on the atmospheric components.

Scattering can take place in different ways: elastically or inelastically. In contrast to elastic scattering, kinetic energy is not conserved during inelastic scattering, leading to a shift in the wavelength of the backscattered signal. Raman lidar is based on an inelastic scattering, which implies the change of the roto-vibrational energy of the molecules. The induced frequency shift is specific for each interacting molecule, like a signature. As advantage, this technique has low demands of spectral purity of the emitted laser beam and frequency stabilization on the receiver, opposite to the DIAL systems. Nevertheless, the main drawback of the Raman technique is that inelastic scattering is much weaker than the elastic one, which makes often photon counting detection necessary. It is weaker because its intensity depends on the Raman cross section, which is typically small, i.e. several orders of magnitude weaker than elastic scattering. Note that rotational Raman has higher signal strength than vibrational Raman i.e. one or two order of magnitude larger. This can lead to difficulties in day time operation, when there is high background noise, depending on the power of the incident laser light and the instrument capability of frequency selection. Because of that, in the past systems could only operate during night time, when the background noise is lower. Nowadays this difficulty is overcome by using strong filters.

From equation 2.12, the lidar equation for a Raman lidar system can be derived. The Raman signal P_R from a distance z, measured at a Raman wavelength λ_R is given by equation:

$$P_R(R) = K_R \cdot G_R(R) \cdot \beta_{\pi_R}(R) \cdot exp\left\{-\int_0^R [\alpha_0(r) + \alpha_R(r)]dr\right\} \tag{2.13}$$

where β_{π_R} is the Raman backscattering cross section, α_0 is the extinction coefficient on the path from the instrument to the Raman scatterer, and α_R the extinction coefficient on the path back to the instrument, once the light has experienced a shift in wavelength. In order to calculate gas concentration atmospheric profiles (i.e. water vapor) the ratio between two Raman signals is calculated. First, the return signal P_R from the gas under study is used, and a second signal P_{ref} from a reference gas, whose concentration is known. Typically, the Stokes roto-vibrational scattering line of N_2 is used, as well as pure rotational Raman transition for N_2 or O_2. Performing the ratio with respect to the reference, the mixing ratio of the gas relative to the dry air (Weitkamp, 2005) is:

[3]Note that the α extinction coefficient is equivalent to the β_e extinction coefficient presented in section 2.2.1. While in the lidar community the term α is preferred, in the microwave community the use of β_e is more extended.

$$m(R) = C \cdot \frac{P_R(R)}{P_{ref}(R)} \frac{exp[-\int_0^R \alpha_{ref}(r)dr]}{exp[-\int_0^R \alpha_R(r)ds]} \tag{2.14}$$

where C is the calibration constant, which is system dependent. In the equation, $G_{ref}(R) = G_R(R)$ has been assumed, because the receiver is the same for the both λ_R and λ_{ref} wavelengths.

Elastic scattering, i.e. when the frequency of the initial radiation is conserved, is used by the DIAL systems, by measuring in single absorption lines or broad absorption bands of gases (Weitkamp, 2005). The principle of a DIAL is based on the measurement at two very close wavelengths in the absorption band of the trace gas (i.e. water vapor). One of them suffers stronger absorption (λ_{on}) than the other (λ_{off}), and thus a differential absorption coefficient, which is related to the gas mass concentration, can be determined.

The general elastic backscatter equation for the received power P from a distance R derived from 2.12, is:

$$P(R) = P_0 \cdot \eta \left(\frac{A}{R^2}\right) \frac{c\tau}{2} \cdot \beta_\pi(R) \cdot exp\left[-2 \int_0^R \alpha(r)dr\right] \tag{2.15}$$

where A is the receiver area, P_0 is the average transmitted power on each pulse, η is the receiver efficiency, τ is the laser pulse duration, c is the speed of light, β_π is the backscatter coefficient and α is the extinction coefficient. If the two emitted wavelengths λ_{on} and λ_{off} are close enough, one can consider that their molecular and particle scattering is equal. Then, the difference in the returns at the two λ is only due to the absorption by the trace gas molecules. Thus, the differential absorption coefficient is:

$$\Delta\alpha = N \cdot \Delta\sigma = N \cdot (\sigma(\lambda_{on}) - \sigma(\lambda_{off})) \tag{2.16}$$

where N is the molecular number density of the trace gas and σ the molecular absorption cross section, that is known from spectroscopy. Using equations 2.15 and 2.16, and performing some algebraic manipulations, the number of molecules of the trace gas is:

$$N = \frac{1}{2\Delta\sigma} \left[\frac{d}{dR} ln\left(\frac{P_{on}}{P_{off}}\right)\right] \tag{2.17}$$

This equation does not depend any more on the system calibration constants, implying that the DIAL is a self-calibrating technique. DIAL is typically applied to gases measurements, such as O_3, NO_2, N_2O, among others. But it is also used to measure atmospheric water vapor. The main challenge for this technique is that it requires high spectral purity and high stability of the emitted laser.

2.3.2 The University of Basilicata Raman lidar system: BASIL

The University of Basilicata Raman lidar system BASIL (Di Girolamo et al., 2009; Di Girolamo et al., 2012) is an active instrument based on the detection of the elastic and Raman backscattered radiation from atmospheric constituents. BASIL includes a Nd:YAG laser emitting pulses at its fundamental wavelength, its second and third harmonics: 1064, 532 and 355 nm, respectively, at a repetition rate of 20 Hz. The average power emitted at 355 nm is 10 W. Raman scattering is stimulated by the 355 nm wavelength, because of the higher cross-section with respect to other wavelengths. Nevertheless, other wavelengths could also be used for water vapor detection, as reported by Althausen et al. (2000). The receiver is built around a larger telescope in Newtonian configuration (45 cm diameter primary mirror) and two smaller telescopes (5 mm diameter lenses). The larger telescope is primarily dedicated to the collection of the Raman signals, i.e. the water vapor and molecular nitrogen roto-vibrational Raman signals, at 407.5 and 386.7 nm, respectively, which are used to estimate the water vapor mixing ratio (WVMR) profiles.

Signal selection is performed by means of narrowband interference filters, whose specifications were reported in Di Girolamo et al. (2004) and Di Girolamo et al. (2009). Sampling of the Raman signals is performed by means of transient recorders with double signal acquisition mode (i.e. both analog, A/D conversion and digital, photon counting). Depending on the application, WVMR profiles can be derived with different vertical and temporal resolutions. These two parameters can be traded-off to improve measurement precision. For the purposes of this study, the lidar products are characterized by a vertical resolution of 30 m and a temporal resolution of 5 minutes.

Because of the absence of overlap between the laser beam and receiver field-of-view, there is a blind region in the lower altitudes: the zero overlap region (ZOR). Due to that, vertical profiles of WVMR typically start at 150-180 m above ground. The temperature signal presents a larger ZOR, i.e. it can vary from 500 meters up to 2 km, depending on the system alignment. The WVMR and T ZORs are different because the signals are collected with different telescopes. Humidity profiles extend vertically up to different altitudes during daytime and night-time depending on the altitude where the signal gets completely extinguished. For water vapor this typically takes place around 5 km during daytime and around 12 km during the night. The different ranges result from the additional noise due to solar contamination during daytime.

During HOPE, BASIL has been calibrated based on the comparison with the radiosondes launched approximately 4 km away from the instrument. A mean calibration coefficient was estimated from the comparison of BASIL and radiosonde data, as described in the following. Every radiosonde coincident with BASIL measurements (60 in total) was compared to the lidar profile in an altitude region with a vertical extent of 1 km above the boundary layer. This region is chosen to minimize the air mass differences related to the distance between the lidar and the radiosonde. For every profile comparison, a value for the calibration constant is calculated. Out

of these 60 values, the mean value was calculated and used as the calibration constant for the complete period of HOPE. The standard deviation of the mean calibration coefficient from the single values does not exceed 5%.

In addition to the calibration constant uncertainty, other smaller uncertainty sources might affect the water vapor measurements. For example, an additional bias (<1%) might be associated with the use of narrowband filters, the temperature dependence of H_2O and N_2 Raman scattering and the thermal drifts of the filters (Whiteman, 2003). Still an additonal 1% might be associated with the determination of the differential transmission term at the water vapor and molecular nitrogen Raman wavelengths (Whiteman, 2003). These sources of uncertainty, in principle negligible, are not taken into account for the calculations in the algorithm.

The statistical uncertainty of the WVMR is proportional to the number of detected photons at each level, calculated from Poisson statistics (Di Girolamo et al., 2004). Providing a profile with 5 minutes time-resolution and 30 meters vertical grid, the statistical uncertainty affecting WVMR measurements for night-time operation is typically smaller than 2% up to 3 km and smaller than 20% up to 9 km. For daytime operation, it is typically smaller than 40% up to 3 km and smaller than 100% up to 4.5 km.

The operation of BASIL was not continuous during HOPE: the instument collected a total of 430 hours of measurements distributed over 44 days, which represents the 30% of the whole HOPE period.

2.3.3 WAter vapor Lidar Experiment in Space: WALES

The WAter vapor Lidar Experiment in Space (WALES) is a lidar developed by DLR (Deutsches Zentum für Luft- und Raumfahrt) installed on HALO (Wirth et al., 2009). This instrument is up to now the only four-frequency airborne lidar, and serves also as preparation for a future space-borne mission. WALES uses four wavelengths in the 935 nm H_2O absorption band, each of them adapted to cover a specific range in the atmosphere (figure 2.7). The use of the four wavelengths allows to measure the water vapor profiles from the lower stratosphere to the planetary boundary layer with high vertical resolution in all climate regions. In addition, WALES has high spectral resolution aerosol and depolarization channels, which provide information about aerosol characteristics.

Two identical lasers are working in two different branches in parallel. The output power of each laser is up to 12 W, using diode-pumped solid-state lasers. The laser frequency is doubled (from 1064 nm to 532 nm) by a second harmonic generator (SHG) , and then converted to a 935 nm wave via an optical parametric oscillator (OPO) . Both steps use a potassium titanyl phosphate (KTP) crystal as nonlinear medium. The two output frequencies of each OPO are alternated at a rate of 50 Hz each. From the two lasers, four frequencies are generated as an output of the two OPO. The four waves are temporally alternated in a resulting 200 Hz pulse. The residual

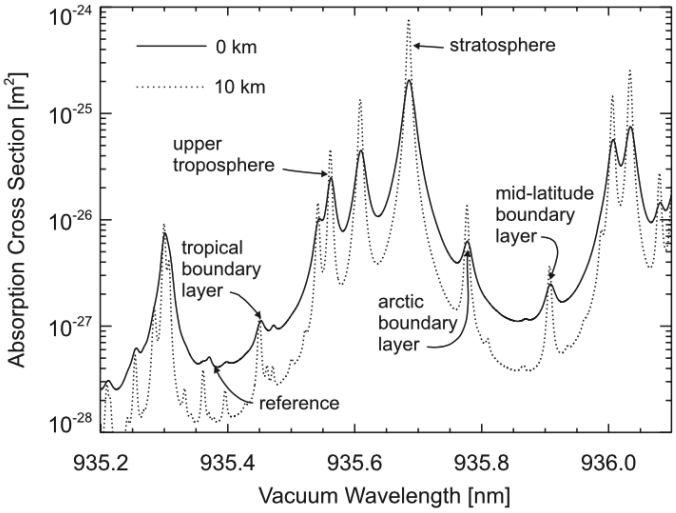

Figure 2.7: Water vapor absorption lines used in WALES. Absorption cross section data calculated from HITRAN 2006 (Rothman et al., 2005) for sea level conditions (solid line) and at 10 km altitude (dashed line) using the US-standard atmosphere. Possible operation wavelengths are indicated by arrows, where the current system is able to use four at a time. Figure is taken from (Wirth et al., 2009).

radiation at 1064 and 532 nm are used for aerosol characterization.

To summarize the four main instruments presented so far, i.e. HATPRO, BASIL, HAMP and WALES, table 2.1 presents an overview of their main features.

2.4 Auxiliary data

In addition to the two main instruments, other data sources are used either for evaluation or a priori information needed for the retrieval, and explained in the following.

2.4.1 Radiosondes and dropsondes

The radiosondes launched during HOPE are DFM-09 manufactured by GRAW Radiosondes GmbH. They measure temperature, relative humidity, pressure and wind (speed and direction) from the ground up to the height when the balloon bursts (~30 km). Continuous data sets are sent to the ground station through a radio-telemetry link. The accuracy of the measurements is specified to be 0.3 hPa, 0.2^{o} C, and 5% for the pressure, temperature and relative humidity, respectively. The radiosonde horizontal position accuracy derived using GPS technology is ~5 m, and the vertical one ~10 m. The wind speed is therefore measured with a 0.2 m/s accuracy. More than 270 radiosondes where launched during HOPE.

During NARVAL, Vaisala dropsondes D94 have been released. D94 is a 350 g sonde equipped with a parachute that measures temperature, pressure, relative humidity and wind. The temper-

Table 2.1: Summary of the main instruments used in this study, their most important features and the type of data used for the current thesis.

	HOPE		**NARVAL**	
	HATPRO	**BASIL**	**HAMP**	**WALES**
Instrument type	Passive MWR	Raman Lidar	Passive MWR	DIAL
Channels	K-band (*22.240, 23.040, 23.840, 25.440, 26.240, 27.840, 31.400 GHz*), V-band (*51.260, 52.280, 53.860, 54.940, 56.660, 57.300, 58.000 GHz*)	1064, 532 and 355 nm	K-band, V-band, W-band (*90.00 GHz*), F-band (*127.25, 122.95, 121.05, 120.15 GHz*) G-band (*183.91, 184.81, 185.81, 186.81, 197.31, 190.81 GHz*)	1064, 935 (4x) and 532 nm
Data used	TBs [K]	WVMR prof. [g/kg], T prof. [K] and their error profiles.	TBs [K]	WVMR prof. [ppm] and its error profiles.
Information on	T and Q prof, IWV, LWP	T and Q prof	T and Q prof, IWV, LWP	Q prof
Time resolution	1 sec.	5 min	1 sec	15 sec
Vertical resolution	N/A	30 m	N/A	7.5 m

ature, humidity and pressure are measured twice a second, with an accuracy of 0.2^{o} C, 2% and 0.4 hPa, respectively. The wind speed and direction are measured with a commercial GPS receiver at a rate of 4 Hz. The dropsonde transmits the data using the 403 MHz meteorological band, to a system on board the aircraft. The descent speed is approximately 21 m/s at 12 km altitude, and ~11 m/s at sea level. This leads to typical descent times of ~15 min from 14 km, and ~8 min from 7.5 km.

The radiosondes and dropsondes will be used for the evaluation of the retrieval, as well as for a priori calculation.

2.4.2 Global Positioning System

The Global Positioning System (GPS) can be used to derive the atmospheric column water vapor (Bevis et al., 1992; Rocken et al., 1997). The signal propagating from GPS satellites to ground-based GPS receivers suffers a delay due to the presence of water vapor in the atmosphere. By studying the delayed signal, in comparison to the undisturbed signal propagating in vacuum, one can get information on the atmospheric state (Dick et al., 2001). Information from the ground

meteorological conditions is needed to perform the IWV retrieval, i.e. pressure and temperature at the surface. The IWV estimates are available typically every 15 min with an accuracy of $1-2$ kg/m^2 (Gendt et al., 2004), in all weather conditions.

The information of the GPS will be used in chapter 4, to compare the IWV from the retrieval and the IWV provided by the GPS station.

2.4.3 JOYRAD35 radar

The JOYRAD35 cloud radar is a Doppler radar manufactured by Metek GmbH (Görsdorf et al., 2015). This instrument transmits linearly polarized radiation at 35.5 GHz and receives the cross- and co-polarized signals at the same frequency. JOYRAD35 provides profiles of radar reflectivity factor, linear depolarization ratio, Doppler spectra and Doppler mean velocity, in a vertical range from 0.2 to 15 km and a typical time resolution of $1-10$ seconds. With these parameters, one can study the macrophysics (i.e. type of particles, cloud boundaries) and microphysics (i.e. liquid-ice content) of the clouds. The radar has scanning capability, which allows to capture the 3D structure of clouds.

This instrument will be used in chapter 6, to estimate the cloud top.

2.4.4 Ceilometer

The Jenoptik CHM15k Nimbus ceilometer[4], operated at JOYCE, is a low power, robust lidar that provides information on aerosol particles and hydrometeors in the atmosphere. The ceilometer emits pulses at 1064 nm and receives the backscattered elastic radiation. Photon counting is used at the receiver to allow for high detection accuracy and high sensitiveness. With a range gate length of 15 meters, the ceilometer is able to provide information on cloud layer penetration depth, vertical visibility, cloud base and aerosol layers, up to 15 km.

This instrument will be used throughout chapters 4 and 5 to detect the cloud base and discriminate the cloudy cases.

2.4.5 Cloudnet

Cloudnet [5] is created with the aim of optimizing the use of existing data sets for validating and developing new cloud remote sensing synergy algorithms, as well as improving the representation of clouds in models. Based on ground-based remote sensing observations, Cloudnet (Illingworth et al., 2007) provides systematic and continuous evaluation and classification of aerosol, clouds and their main parameters for climate and forecast models.

Cloudnet can be applied to provide continuous vertical profiles of cloud geometry, cloud fraction, liquid water content and ice water content, among others, to sites where at least these

[4] https://www.jenoptik.com

[5] http://www.cloud-net.org

three instruments are available: cloud radar, ceilometer and dual-frequency MWR. At the site of JOYCE, these and other instruments provide continuous atmospheric measurements and the Cloudnet products and classification are available since 2011.

The LWP Cloudnet product will be used in chapter 6, for the construction of the a priori calculation (section 3.2.1) for the cloudy scenario.

2.4.6 ERA-Interim reanalysis

ERA-Interim is the latest global atmospheric reanalysis produced by the European Centre for Medium-Range Weather Forecasts (ECMWF)[6] . The reanalysis provides a description of the recent climate, as the combination of model and observations, containing the best estimates of the three dimensional distribution of atmospheric variables.

ERA-Interim covers the period from the 1st of January 1989 onwards, and is extended forward almost in real time. The data assimilation system used to produce this reanalysis is based on a 2006 release of the ECMWF Integrated Forecast Model (Cy31r2). The system includes a 4-dimensional variational analysis (4D-Var) with a 12-hour analysis window. The spatial resolution of the data set is ~80 km on 60 vertical levels from the surface up to 0.1 hPa (Dee et al., 2011).

From ERA-Interim, the surface parameters (surface wind, sea surface temperature, surface pressure) and profile data (cloud information and pressure, temperature and humidity profiles) will be used. More information on how these data are used is provided in section 3.2.1.3.

2.5 Summary

The measurements used in this thesis were taken during two major field campaigns: HOPE (section 2.1.1) and NARVAL (section 2.1.2). The two field experiments, carried out in regions with very different climatological conditions, are presented at the beginning of the current chapter. After that, the instruments concerning this study are described, focusing on MWR and lidar.

During HOPE, a HATPRO (section 2.2.2) MWR was measuring. In HALO, the aircraft flying during the NARVAL experiment, the module HAMP (section 2.2.3) was installed. The theory related to the working principle of these instruments has been presented in section 2.2.

Two lidars are used in this thesis, based on different physical principles. The first, a Raman Lidar, i.e. BASIL (section 2.3.2), measured water vapor mixing ratio and temperature during HOPE. The second, WALES (section 2.3.3), is a DIAL installed on HALO to measure atmospheric mixing ratio. Their theory is presented in section 2.3.

Additionally, section 2.4 presents a short description of the auxiliary data used in the thesis, e.g. GPS, sondes, radar, ceilometer, etc.

[6] http://www.ecmwf.int

3

Algorithm

The Optimal Estimation Method (OEM) is a special application of the Bayesian probability theory. Here, an application for retrievals of atmospheric parameters, i.e. humidity and temperature profiles, will be developed. Compared to other retrievals, e.g. statistical retrievals or retrievals based on neural networks, the OEM offers several benefits. First, OEM allows a posteriori analysis of the retrieval. This implies that an information content assessment is possible, as well as theoretical error quantification, which is important for any evaluation and data assimilation. Second, the solution is physically consistent, which means that, given the retrieved profiles and the forward model, the measurements can be reproduced within their uncertainties.

In this chapter, first the general theory of the OEM will be introduced (section 3.1). In section 3.2, the details of the retrieval algorithm developed within this thesis, LIME SOAP (Lidar and Microwave Synergetic Optimal Atmospheric Profiler), will be described. In the different chapters of this thesis, LIME SOAP will be applied in several contexts. First, the HOPE dataset will be investigated, where separate analysis of water vapor (chapter 4), temperature and relative humidity (chapter 5) retrievals will be performed. A cloudy scenario will be presented in chapter 6. Finally, the water vapor and temperature retrieval from the airborne perspective of HALO will be examined (chapter 7).

3.1 Optimal Estimation theory

Retrieving an atmospheric state is in general an *ill-posed* problem. This means that although the model, which relates the instrument measurements to the atmospheric state, is well known, there are multiple possible atmospheric states that would fit one set of measurements. In other words: a unique solution between the atmospheric state and the measurements cannot be found.

To overcome this ambiguity, an inverse method is used. Said method allows to optimally estimate the state of the atmosphere, i.e. to find the most probable solution and its associated

uncertainty. Using this scheme requires a set of measurements, together with their uncertainty specification, a forward model $F(x)$, which relates the atmospheric state x to the instrument measurements y, and some *a priori* information x_a. In the following, a short description of the OEM is presented. More details can be found in Rodgers (2000).

Two main assumptions are required for applying the method. First, the relation between the atmospheric state and the instrument measurements must be *linear* to a certain degree. Second, the covariance distributions of measurements S_y and atmospheric states S_x must be Gaussian distributed. Under these assumptions one can apply the Bayesian theory to define a cost function $J(x)$, which is minimized in order to find the most probable atmospheric estate:

$$J(x) = [y - F(x)]^T S_\epsilon^{-1}[y - F(x)] + [x - x_a]^T S_a^{-1}[x - x_a] \tag{3.1}$$

where S_a and S_ϵ are the covariance error matrices of the prior and measurement, respectively. According to their covariances, the observations and the a priori information are weighted in the retrieval, i.e. measurements with small uncertainty will have a stronger weight onto the solution. Sections 3.2.1 and 3.2.2 will provide further details on their calculation.

The solution for the atmospheric state is found iteratively, converging to the state vector x_{op} that minimizes the cost function in equation 3.1 through the equation:

$$x_{i+1} = x_a + (S_a K_i^T \cdot (K_i S_a K_i^T + S_\epsilon)^{-1} \cdot [y - F(x_i) + K_i \cdot (x_i - x_a)]) \tag{3.2}$$

where x_i is a vector containing the atmospheric state at the iteration i. The variable K represents the Jacobian, which is the sensitivity of the forward model with respect to changes of the atmospheric state vector:

$$K_i = \frac{\partial F(x_i)}{\partial x_i} \tag{3.3}$$

By iterating equation 3.2, a most probable atmospheric state x_{op} is reached when a convergence criterion is fulfilled. Here, the convergence criterion is based on the difference between the observational estimates at iterations n, $F(x_n)$, and $n+1$, $F(x_{n+1})$. To evaluate this difference one must scale the change in the solution by its estimated error, leading to:

$$d_i^2 = (F(x_{i+1}) - F(x_i))^T \cdot (S_\epsilon \cdot (K S_a K^T + S_\epsilon) \cdot S_\epsilon)^{-1} \cdot (F(x_{i+1}) - F(x_i)) << m \tag{3.4}$$

where m is the number of elements in the observation vector. In practice, convergence is found when d_i^2 is at least one order of magnitude smaller than m. A major benefit of using this method is that one can directly calculate a posterior error covariance matrix S_{op} associated to the optimal solution x_{op}. Said matrix is calculated with the expression:

$$S_{op} = S_a - S_a K^T \cdot (S_\epsilon + K S_a K^T)^{-1} \cdot K S_a \tag{3.5}$$

where K is the Jacobian calculated in the last iteration. Another benefit is the possibility to estimate the information content of the measurements for the retrieved atmospheric state: the degrees of freedom for signal (DOF) represent the amount of independent pieces of information contained in the measurements. They can be calculated as the trace of the averaging kernel matrix A_{ker}:

$$A_{ker} = S_a K^T \cdot (S_\epsilon + K S_a K^T)^{-1} \cdot K \tag{3.6}$$

This matrix describes the subspace of the atmospheric state space in which the retrieval must lie. Each diagonal element in A_{ker} is a measure of the DOF for each element in x. In the case of retrieving an atmospheric profile, the diagonal elements of A_{ker} represent the independent pieces of information per altitude level. Following this interpretation, its reciprocal would be the number of levels per degree of freedom, and thus, a measure of resolution. The vertical resolution Δz of a retrieved profile is another way to assess the information content of the retrieval. Δz is defined as the range of heights covered, divided by the number of independent quantities measured, and is calculated according to the equation:

$$\Delta z = \frac{\delta z}{diag(A_{ker})} \tag{3.7}$$

where δz is the vertical grid spacing used in the retrieval. It is important to note the difference between the vertical discretization of the retrieved profile and the quantification of the *efficient* vertical resolution Δz.

3.2 LIME SOAP

In the framework of this thesis, the **Li**dar and **M**icrowav**e** **S**ynergetic **O**ptimal **A**tmospheric **P**rofiler (LIME SOAP) has been developed. The algorithm that combines MWR and RL measurements is based on the optimal estimation technique, as presented in section 3.1. The definition of LIME SOAP allows to flexibly combine several measurements into the retrieval algorithm.

Before one can apply the algorithm to a given atmospheric scenario, some preparation is needed. First of all one needs to specify the variables to retrieve (i.e. absolute humidity, temperature or both together) and their discretization, the kind of measurement information used for such aim (e.g.: only from RL, only from MWR or the both) and for which set of conditions the algorithm will be applied. For example, one cannot consider the same prior information for a site in Germany during spring, than for aircraft measurements in the tropics.

Thus, the configuration of the a priori information (S_a and x_a), the measurement information (y and S_ϵ), the forward models $F(x)$ and the state vector x, change for the different LIME SOAP applications during this thesis. In the following sections, the different parts of the retrieval are explained for each specific scenario.

3.2.1 A priori information and atmospheric state

The a priori information provides a background knowledge of the atmospheric state. It serves to constrain the infinite number of solutions in the atmospheric state space to a physically meaningful subset. In general, the a priori state x_a should be any state preferably *close* to the solution. It can be defined, for example, as an average of typical atmospheric states. The covariance matrix S_a provides an uncertainty estimation for x_a, including also the correlation among the a priori uncertainties.

In LIME SOAP, the covariance (*cov*) matrix for a joint retrieval of two variables, i.e. temperature and humidity profiles, is defined as:

$$S_{a,(T,q)} = \begin{pmatrix} cov(T,q) & cov(q,q) \\ cov(T,T) & cov(q,T) \end{pmatrix} \tag{3.8}$$

where q is atmospheric humidity (i.e. absolute humidity (AH) $[kg/m^3]$ or relative humidity (RH) [%]) and T is the temperature [K]. Both q and T are defined as a function of the altitude:

$$\begin{aligned} q &= [q_1, q_2, ...q_k] \\ T &= [T_1, T_2, ...T_k] \end{aligned} \tag{3.9}$$

with k the total number of altitudes in the vertical retrieval grid. The covariance matrix of the a priori profile is estimated from a large ensemble of typical atmospheric states:

$$cov(a,b) = \frac{1}{n-1} \sum_{i=1}^{n} [(a_i - \bar{a})(b_i - \bar{b})] \tag{3.10}$$

In equation 3.10 (Wilks, 2006), the index i goes over the total number of profiles taken into account, i.e. every radiosonde or the chosen reanalysis profiles. The variables a and b represent both humidity and/or temperature at each height level. The terms $\bar{a}$ and $\bar{b}$ are the averaged values of a and b over all profiles. In order to better illustrate the relations between water vapor and temperature at different height levels in the atmosphere, the correlation matrix (*corr*) is provided by:

$$corr(a,b) = \frac{cov(a,b)}{s_a s_b} = \frac{\frac{1}{n-1} \sum_{i=1}^{n} [(a_i - \bar{a})(b_i - \bar{b})]}{\left[\frac{1}{n-1} \sum_{i=1}^{n} (a_i - \bar{a})^2\right]^{\frac{1}{2}} \left[\frac{1}{n-1} \sum_{i=1}^{n} (b_i - \bar{b})^2\right]^{\frac{1}{2}}} \tag{3.11}$$

The a priori information corresponding to the three different LIME SOAP applications, i.e. clear sky and cloudy conditions during HOPE and clear sky conditions during NARVAL, are presented in the following.

3.2.1.1 *A priori information for clear sky conditions during HOPE*

From the ground based perspective, the linear AH and T are retrieved. The retrieval of the linear humidity profiles from MWR has been already implemented by other authors (Meunier et al., 2015; Turner and Löhnert, 2014; Steinke et al., 2014b; Solheim et al., 1998). The a priori information for the HOPE period for the T and AH profiles is calculated from the radiosondes launched during the campaign. A total of 217 sondes have passed the quality criteria.

From this set of 217 radiosondes, average profiles of T and AH have been calculated to represent the a priori profile x_a, together with the corresponding covariance matrix S_a. The correlation matrix is shown in figure 3.1, presenting how the two variables (AH,T) are correlated as a function of the altitude, from ground to 10 km, and is composed of the four submatrices: corr(T,T), corr(AH,AH), corr(AH,T) and corr(T,AH).

The temperature corr(T,T) clearly reveals the tropopause at altitudes > 9 km, indicated by a strong change in correlation to negative values. Furthermore, a drop in correlation can be seen between the boundary layer (~1.5 km) and the free troposphere above. The corr(T,T) values are higher than the water vapor corr(AH,AH) values, which show a much higher variability. The values for corr(AH,AH) are strongest close to the main diagonal as expected, but decrease quickly for off diagonal terms, whereas the corr(T,T) is stronger in the off diagonal terms. In the lowest 1-2 km there is a higher correlation in all cases, because of the well mixed conditions in the boundary layer. The corr(T,AH) and corr(AH,T) present rather poor correlation in the middle troposphere. The results are similar to the ones presented in a previous study by Ebell et al. (2013).

When the absolute humidity profile is retrieved (chapter 4) only the submatrix $S_{a,(AH,AH)} = cov(AH, AH)$ will be used. Likewise, when temperature profile is retrieved alone (section 5.1), only the submatrix $S_{a,(T,T)} = cov(T, T)$ will be taken into account. The complete matrix $S_{a,(T,AH)}$ will be needed for the simultaneous retrieval of both temperature and humidity, used in section 5.2 and referred in the following as T-Q correlation.

3.2.1.2 *A priori information for cloudy conditions during HOPE*

The a priori information presented in section 3.2.1.1 for AH and T retrievals turned out to be inappropriate for the cloudy analysis in chapter 6, i.e. in the afternoon of the 4th of May 2013. An improvement on x_a and S_a has been performed such that the new a priori information presents a more adequate description of the atmospheric conditions during the case study.

LIME SOAP is run for 24 hours data on the 4th of May, i.e. 163 clear sky profiles, using only RL information and the x_a and S_a from section 3.2.1.1. The results are full atmospheric profiles that provide a general estimate of the atmospheric conditions for the day under study. From this set of 163 profiles, average AH and T profiles are calculated as well as their covariance (S_a) and correlation (see figure 3.2) matrices.

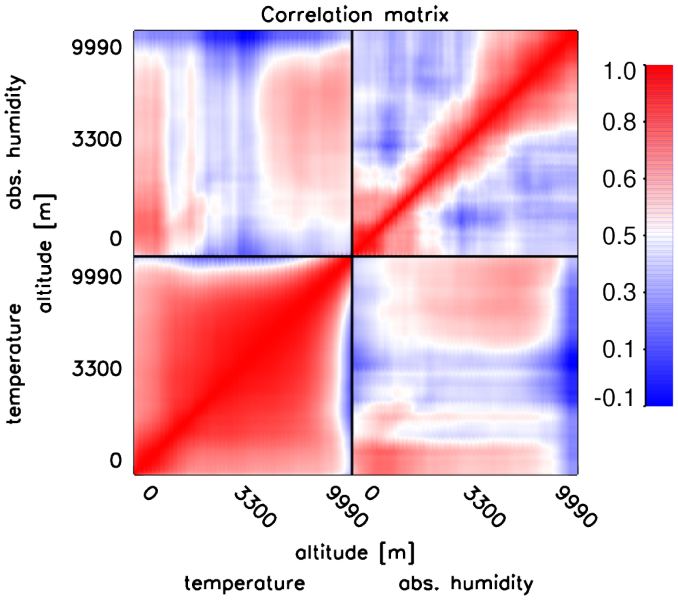

Figure 3.1: Correlation matrix for the 217 radiosondes in HOPE. Correlation is shown between temperature and absolute humidity as a function of the altitude (from 0 to 10 km). Second and third quadrants (from up to down and left to right), represent the corr(AH,AH) and corr(T,T). The first and fourth represent the corr(T,AH) and corr(AH,T) respectively.

In the presence of a cloud the liquid water path (LWP) is retrieved in addition to the T and AH profiles. To avoid negative values in the result, the LWP is retrieved on a logarithmic scale. This approach has been used before in previous studies, e.g. Löhnert et al. (2004). For the a priori information, an average log(LWP) (defining x_a) has been calculated, together with its standard deviation (for the definition of S_a), using 5 years (from 2011 to 2016) of Cloudnet data (see section 2.4.5) at the site of JOYCE. Because the cloud under study in chapter 6 has a thickness of $\sim$ 200 m, clouds with thickness between 150 and 250 meters have been considered for the calculations. The resulting a priori pieces of information are 1.27 $log(g/m^2)$ and 1.06 $log(g/m^2)$ for the mean LWP and its standard deviation respectively.

3.2.1.3 A priori information for clear sky conditions during NARVAL

In contrast to the ground based perspective, from the airborne viewpoint the retrieval of the linear AH is not possible. This is because the solution x_{op} tends typically to negative values in high altitudes where the water vapor is low. To avoid this unphysical result, the logarithmic AH is retrieved instead of the linear AH. Other authors, like Hewison (2007), Cimini et al. (2010) or Deblonde and English (2003), have also implemented the retrieval of the logarithmic humidity.

For NARVAL, two types of a priori information have been calculated: using model reanalysis data and using dropsondes (DS) . Chapter 7 will justify the reason for that and will present the

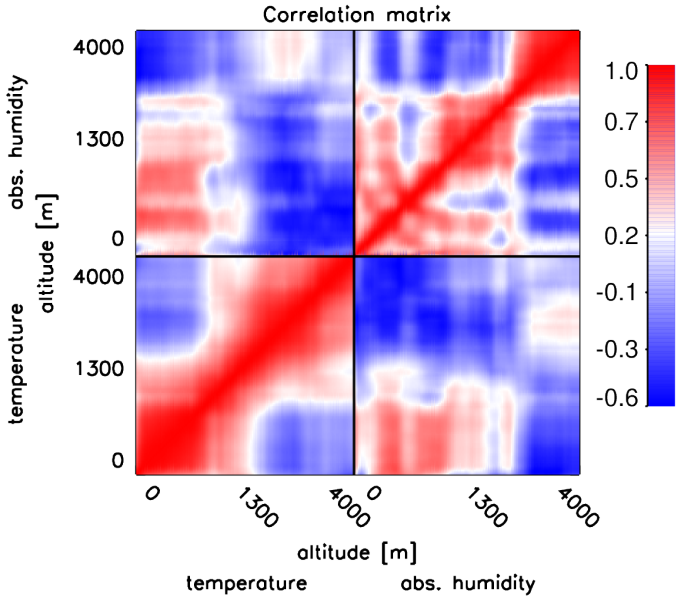

FIGURE 3.2: Correlation matrix for the the cloudy scenario on the 4th of April 2013. Correlation is shown between temperature and absolute humidity as a function of the altitude (from 0 to 4 km). Second and third quadrants (from up to down and left to right), represent the corr(AH,AH) and corr(T,T). The first and fourth represent the corr(T,AH) and corr(AH,T) respectively.

details of their application.

The first prior is obtained from the ERA-Interim reanalysis (see section 2.4.6). Because HALO flies from Germany to Barbados, a wide variety of atmospheric scenarios will be measured. So, instead of calculating a mean profile for the whole domain as prior profile, three areas with similar atmospheric behavior have been defined for the a priori calculation (see figure 3.3). For the calculation of the a priori profiles and covariance matrices the data of the month of December 2013 is used. Note that only non-land points with clear sky conditions are considered. This implies that several thousands of profiles in each region are used to calculate x_a and S_a. The resulting correlation matrix for the region defined between 5 and 20 N degrees latitude (figure 3.3) is presented in figure 3.4. The figure reveals features like the boundary layer height (correlation inversion at $\sim$ 2 km), as well as the tropopause at around $\sim$ 11 km altitude, higher than in the a priori information calculated at the German site (found at around 9 km).

In a second approach, the a priori is calculated from clear sky DS data. From the 75 DS launched during NARVAL, 34 have been identified as clear sky based on a simple RH threshold of 93% in the latitude range between 5-25 degrees North. The resulting correlation matrix (figure 3.5) is less smooth than the one calculated from ERA-Interim, because much less profiles are used in the calculations. Despite this fact, similar atmospheric description (i.e. boundary layer and tropopause) is shown by both correlation matrices, presenting sharper transitions the one

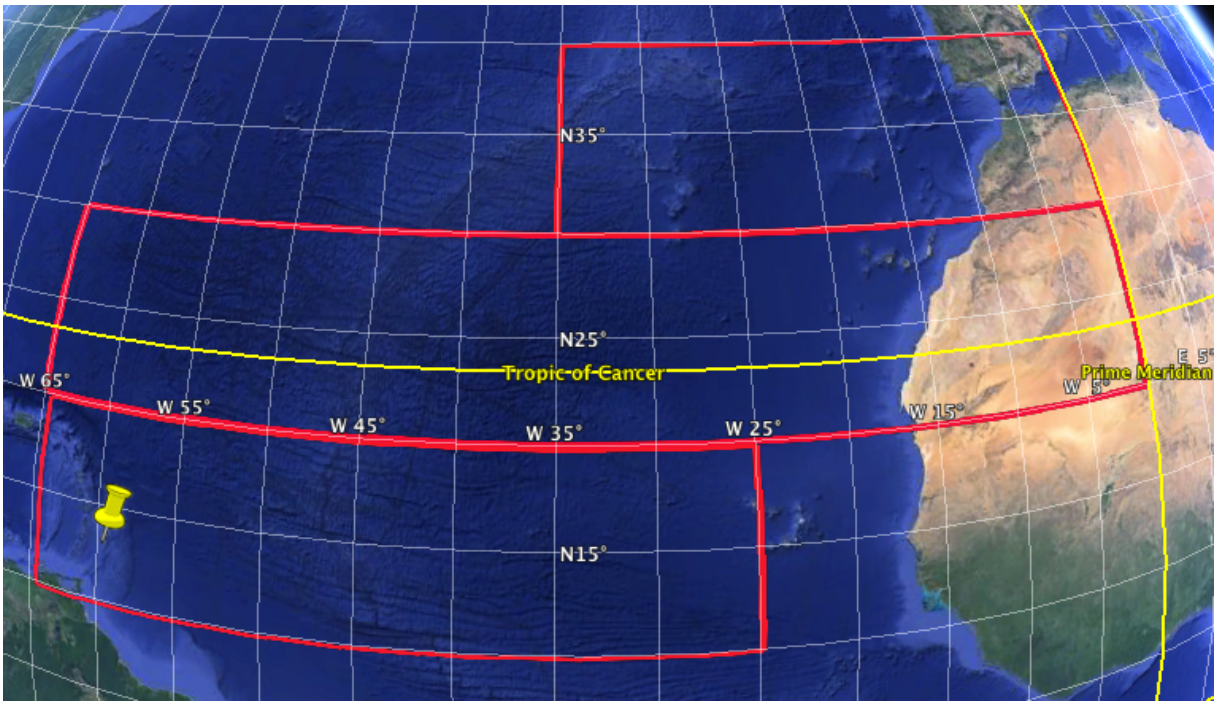

Figure 3.3: Different regions where an a priori is defined, as a function of the latitude and longitude. They are chosen according to the HALO flight patterns. The yellow pin shows the position of Barbados. Source: Google Earth.

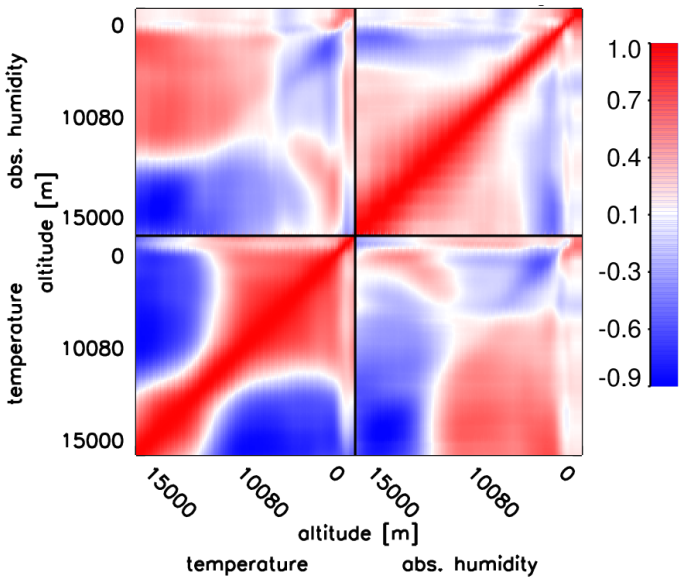

Figure 3.4: Correlation matrix for the ECMWF model during NARVAL. Correlation is shown between temperature and absolute humidity as a function of the altitude (from 0 to 10 km). Second and third quadrants (from up to down and left to right), represent the corr(AH,AH) and corr(T,T). The first and fourth represent the corr(T,AH) and corr(AH,T) respectively.

calculated from DS. Furthermore, the T correlation of altitude levels higher than ~ 10.1 km is larger for the DS prior information than for the one based on ERA-Interim.

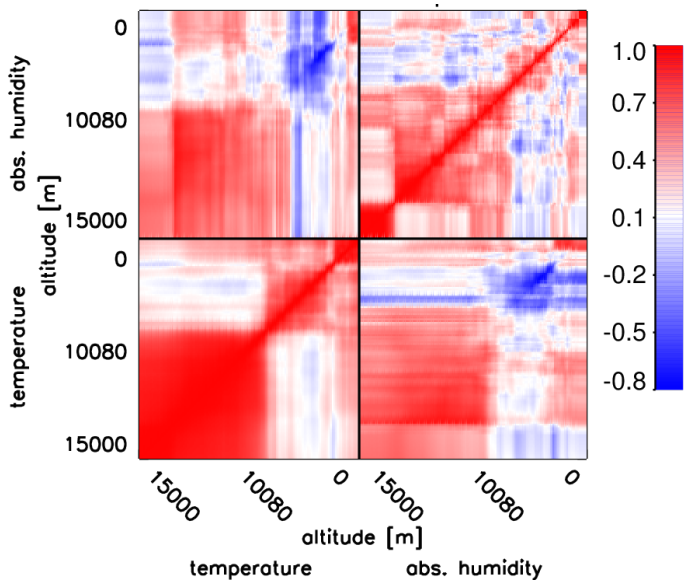

FIGURE 3.5: Correlation matrix for dropsondes during NARVAL. Correlation is shown between temperature and absolute humidity as a function of the altitude (from 0 to 10 km). Second and third quadrants (from up to down and left to right), represent the corr(AH,AH) and corr(T,T). The first and fourth represents the corr(T,AH) and corr(AH,T) respectively.

3.2.2 INSTRUMENT DATA

In both retrieval applications, i.e. the HOPE and NARVAL scenarios, data from MWR and lidar are used in LIME SOAP. The measurement information is contained in the vector y, whose size n_y is variable. While the MWR provides always the same amount of data at a given time (i.e. 14 frequency channels), for every lidar profile the number of altitudes where the data can be considered meaningful varies. The range up to where the lidar data can be used is determined by the relative lidar measurement error. When this value is larger than 100%, the data is considered too noisy and discarded. Care is needed when defining this threshold, because possible random peaks in the lidar uncertainty can lead to a misidentification. Therefore, a running vertical average is performed on the data with a 300 m window size. Note that this smoothed profile of lidar error is only used to select the clipping altitude for the lidar data. In general, the range with valid lidar data depends on the weather situation and night/day-periods. For example, from the ground-based perspective, the maximum altitude where water vapor can be used is typically $\sim 3-4$ km during daytime; and $\sim 7-8$ km during nighttime measurements.

As mentioned before, the measurement covariance matrix S_ϵ contains the uncertainty information associated to the measurements and forward model. Since the number of measurements at each time step changes, also the size of S_ϵ, i.e. $n_y \times n_y$, varies. The part of S_ϵ corresponding to the MWR, contains the variance and error covariance between the frequency channels when observing a black body target. The part of S_ϵ associated to the lidar contains the information of the lidar noise at each altitude level, which is assumed to be uncorrelated (Sec. 2.3.2). The

covariance between lidar and MWR measurements will be considered zero because no correlation is expected among measurements of two separate instruments with different measurement principles.

3.2.2.1 Instrument data for HOPE

For the HOPE analysis, the measurements used are the TBs from the MWR HATPRO (section 2.2.2) and the mixing ratio and/or temperature from BASIL (section 2.3.2). In the simplest case when one single atmospheric parameter is retrieved, y is composed of $t + m$ elements, where m is the number of altitudes where the lidar measurements have sufficient signal to noise ratio and t is the number of TBs. For the water vapor study only zenith TB measurements have been used since non-zenith measurements do not improve the retrieval of vertical humidity profiles (Crewell and Löhnert, 2007). Thus, seven brightness temperatures are used for the retrieval of absolute humidity (chapter 4), while a total of 27 TBs are used in the case of the temperature retrieval (chapter 5), due to the inclusion of angular information (see section 2.2.2). The most beneficial scanning strategy considers the four most opaque channels (i.e. 54.94, 56.66, 57.3 and 58 GHz) with their angular information (90, 42, 30, 19.2, 10.2 and 5.4 degrees) and the three more transparent channels (i.e. 51.26, 52.28, 53.86 GHz) with only their zenith measurements (Crewell and Löhnert, 2007).

In the case of the simultaneous humidity and temperature retrieval (see chapter 5), the vector y consists of $t_q + t_T + m_q + m_T$ measurement, which are: the seven TBs of the K-band (t_q), the 27 TBs in the V-band (t_T), the number of valid altitudes for the lidar mixing ratio (m_q) and the number of valid altitudes for the lidar temperature (m_T).

An example time series of the BASIL and HATPRO measurements is provided in figure 3.6, for the 17th and 18th of April 2013. The figure shows the TBs of the K- and V-band, which include information for the calculation of the humidity and temperature profiles, respectively. The differential response of the 14 HATPRO channels to water vapor and temperature variations can clearly be seen. Water vapor signals in the K-band are most strong in the 22 GHz absorption line, and decrease toward the window frequencies. The temperature diurnal cycle can be seen clearly in the most opaque of the temperature channels (58 GHz). The example dnicely shows how the RL signal gets extinguished when encountering a cloud between ~5-7 UTC (figure 3.6(a)). The MWR provides continuous information also in cloudy scenarios, where liquid clouds cause the strongest signal in the most transparent channels on the V-Band (figure 3.6(b)).

The error covariance matrix associated with the HATPRO MWR measurements was obtained empirically by calculating the covariance between the different channels while constantly viewing an ambient black-body target with known temperature. It is a 7×7 square matrix for each band. If temperature and humidity are retrieved together, then both MWR bands are used and it becomes a 14×14 matrix. The diagonal elements represent the variance of each channel, which adopts

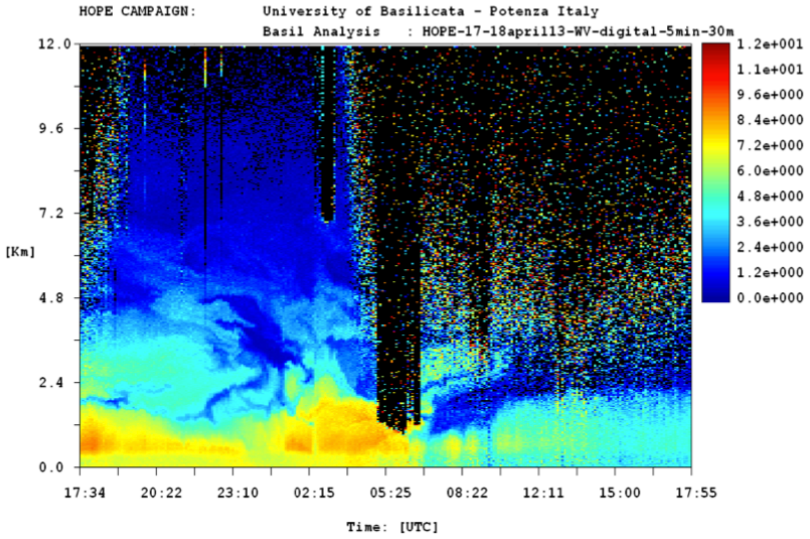

(A)

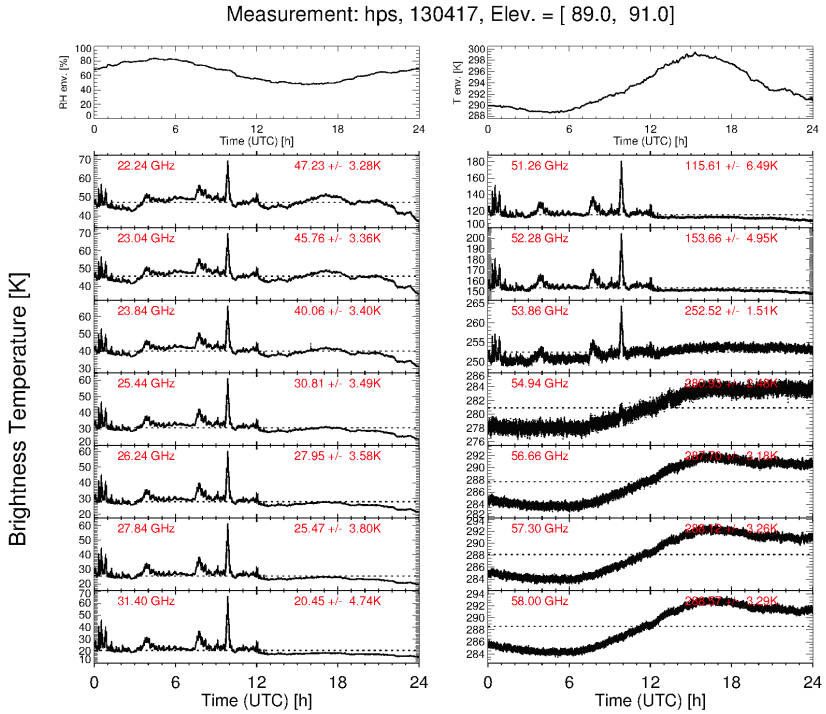

(B)

FIGURE 3.6: Timeseries of (a) mixing ratio profiles [g/kg] from BASIL for the 17th and 18th April and (b) brightness temperature [K] from HATPRO in the K- (left) and V- (right) bands during HOPE on the 17th of April. In addition, the upper most graphs represent the environmental RH (left) and T (right) measured in situ by instrument sensors. Source: (a) Personal communication with Paolo Di Girolamo, (b) *http://gop.meteo.uni-koeln.de/ hatpro/dataBrowser/*.

values around the noise level (~ 0.25 K). The off-diagonal elements are not zero because the

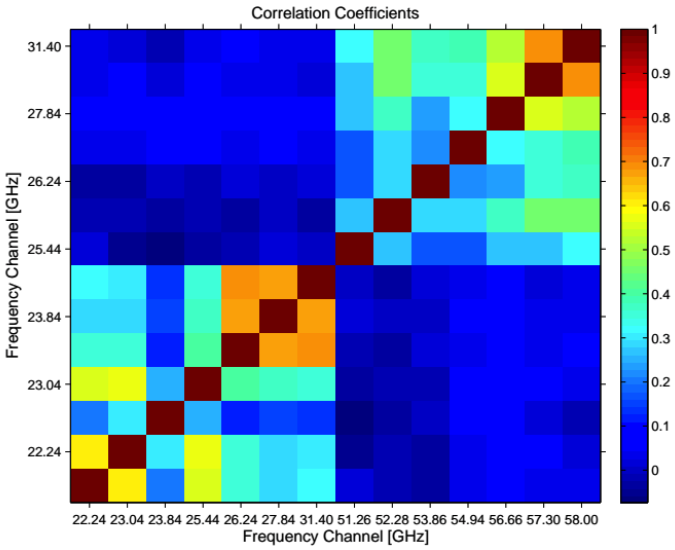

Figure 3.7: Correlation measurement matrix for HATPRO, calculated for the 14 frequency channels. Source: Personal communication with Nils Kuechler.

channels with similar frequencies share some electronic components inside the instrument. They represent the covariance between the measurements of different channels, and though small, they should be considered. Figure 3.7 shows the correlation matrix for the HATPRO MWR measurements, which is a normalized version of the covariance matrix S_ϵ and thus, describes the same behaviour. Figure 3.7 shows also that there is almost no correlation between K and V bands.

The submatrix of S_ϵ corresponding to the RL has dimensions $m_T \times m_T$ for temperature or $m_q \times m_q$ for mixing ratio and it is defined as a diagonal matrix containing only the random uncertainty at each altitude. This definition implies no correlation between measurements in different heights. This simplification in the error covariance matrix has also been considered in other studies (Wulfmeyer et al., 2006; Dunbar et al., 2014; Adam et al., 2015).

The S_ϵ elements corresponding to the correlation between RL and MWR measurements is set to zero because no correlation is expected among measurement uncertainties of two separate instruments with different measurement principles.

3.2.2.2 Instrument data for NARVAL

In the airborne scenario, y contains the TBs of the HAMP MWR channels and the mixing ratio profile (in parts per million) from the lidar WALES. Note that WALES, in contrast to BASIL, is not able to provide temperature measurements. An example of the measurements of WALES and HAMP are shown in figure 3.8 for the third research flight on the 12th of December 2013. Figure 3.8b clearly shows how each frequency channel is sensitive to different atmospheric layers depending on the atmospheric absorption at the given frequency (see also figure 2.6). For

example, the coldest channels in the G-band are more sensitive to layers close to the instrument, i.e. the most opaque frequencies. Note that the jumps in the 197.31 GHz channel, which are specially strong from the beginning of the flight until ~17 UTC, correspond to drifts between periodic internal calibrations. The higher brightness temperatures in the K-band are associated to window channels. The most transparent channels in the K-band, i.e. higher frequencies, adopt their highest value when a liquid water cloud is present. The water vapor peaks agree with the lidar data gaps in the lowest 2 km due to the signal attenuation for presence of clouds (figure 3.8a). The TBs in the V-band show how the highest frequencies are more opaque and sense the ambient temperature. For example, the step in these highest frequency channels at around 17.8 UTC shows a flight altitude change, which is visible also in figure 3.8a for the lidar measurements. Also in this channels, the take off from 14 to ~14.25 UTC is most visible.

The covariance matrix S_ϵ for the lidar, similar to BASIL, is a diagonal matrix that contains the random uncertainty of the measurements calculated at each altitude. In the case of HAMP, and since the instrument is not available to us, S_ϵ cannot be empirically calculated. In this case, a diagonal matrix whose diagonal elements are the square values of the instrument noise level (~0.5 K) is defined. This implies that the measurement uncertainties between any pair of frequencies are uncorrelated. This approximation has been already used by other authors (Löhnert et al., 2009).

3.2.3 Forward models

The forward model $F(x)$ is the function that relates the atmospheric state x to the observations. For example: given an absolute humidity profile, which TBs would the MWR measure. In the algorithm, different forward models (FM) associating the atmospheric state with different measurement types are required. In the following, the FMs for the MWR, for the lidar humidity and for the RL temperature measurements are explained.

The forward model uncertainties are difficult to estimate, including uncertainties due to the application of the radiative transfer model on a discrete height grid, errors associated to the absorption model and other factors. One way to capture these uncertainties is to inflate the observational covariance matrix (Masiello et al., 2012), and different approaches are performed in literature for that (Turner and Löhnert, 2014; Ebell et al., 2013; Heidinger and Pavolonis, 2009). Nevertheless, in this study, the forward model uncertainty is not included in the retrieval, considering the FM as *perfect*. However, one should keep this approximation in mind for the interpretation of the a posteriori error analysis.

3.2.3.1 Forward models for HOPE

The forward models for the RL are trivial, since RL raw data, i.e. photon counts, will not be used, but products, i.e. mixing ratio or temperature profiles, will be used instead. Therefore the lidar

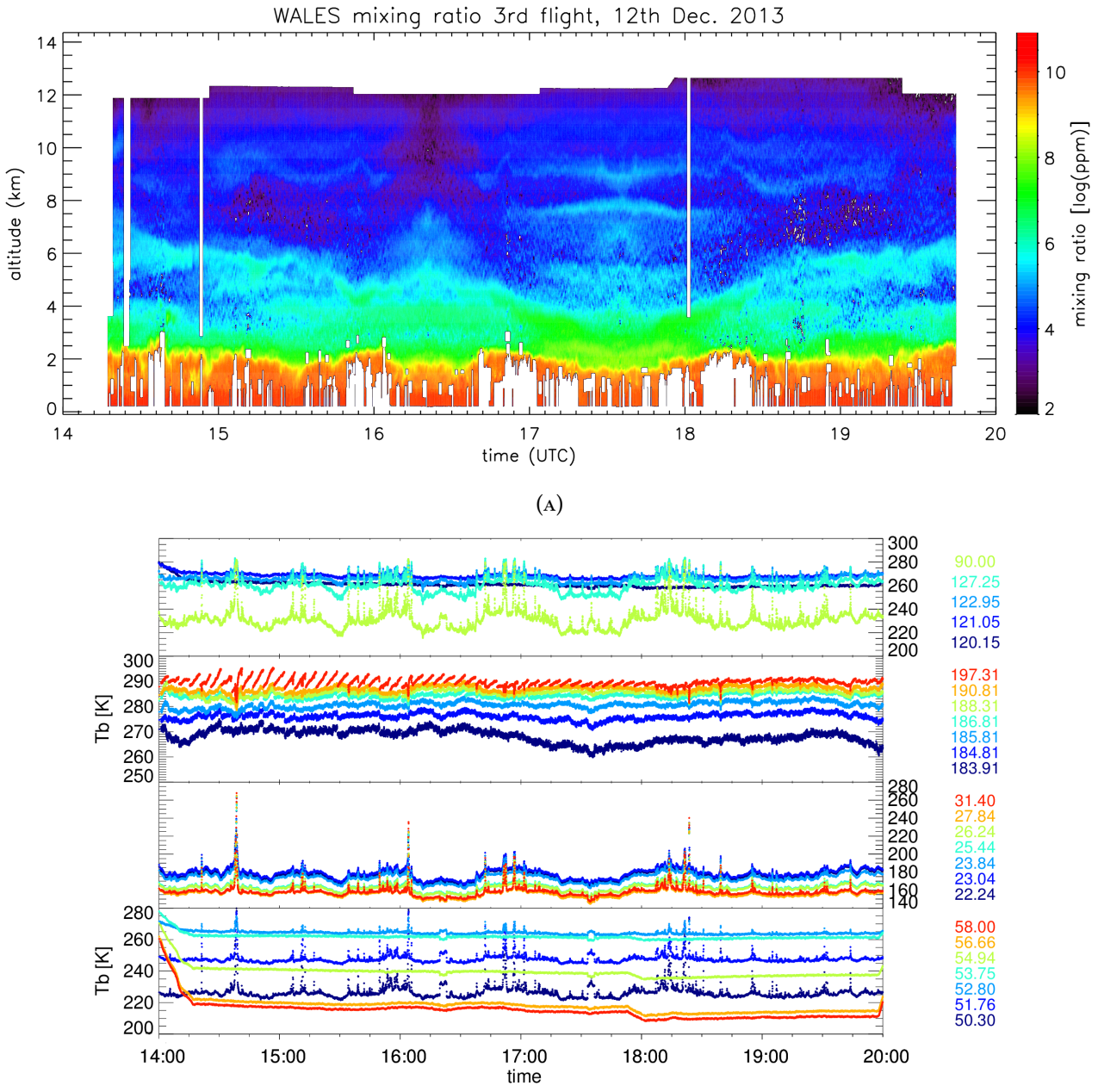

(A)

(B)

Figure 3.8: Timeseries of (a) mixing ratio profiles [ppm] from the lidar WALES and (b) brightness temperature [K] at the 26 frequencies of HAMP during NARVAL-South. Example for the third research flight on the 12th of December 2013.

FM for water vapor simply performs the conversion from absolute humidity to mixing ratio, according to the formula:

$$mr = 0.622 \cdot \frac{AH}{\frac{p}{R_w \cdot T} - AH} \tag{3.12}$$

where mr is the water vapor mixing ratio in kg/kg, AH is the absolute humidity in kg/m^3, R_w is the water vapor gas constant (R_w = 461.52 J/(kg K)), P is the pressure in Pa and T is the temperature in K. In the case of the temperature, the RL FM is the unity, i.e. $F(T)$ is simply T_{RL}.

The FM for the MWR is more complex since it involves radiative transfer (RT) calculations. Here, the RT model by Simmer (1994) is used. It considers emission and absorption of radiation by gases in the atmosphere but neglects scattering, which can be ignored for all atmospheric particles except for rain droplets (see section 2.2). The model calculates the optical thickness and absorption coefficients for each atmospheric layer. The gas absorption is calculated based on the Rosenkranz absorption model (Rosenkranz, 1998). The absorption of liquid water (which will be discussed in chapter 6 for cloudy scenarios) is calculated according to Liebe et al. (1991). From the derived absorption coefficients, the TBs are calculated using the the radiative transfer equation (eq. 2.8).

3.2.3.2 Forward models for NARVAL

For the retrieval application to the airborne measurements, the FM for the lidar humidity measurements is also simple. It performs the conversion from absolute humidity [kg/m^3] to mixing ratio [parts per million] with the equations:

$$q_{spec} = \frac{AH}{\frac{P}{T \cdot R_L} - AH \cdot 0.6078} \tag{3.13a}$$

$$mr_{ppm} = \frac{q_{spec}}{1 - q_{spec}} \cdot 10^6 \cdot \frac{M_d}{M_w} \tag{3.13b}$$

where R_L = 287.05 is the gas constant for dry air, M_d = 28.97 g/mol and M_w = 18.015 g/mol are the molar masses of water and dry air, respectively, q_{spec} is the specific humidity, and mr_{ppm} is the water vapor mixing ratio in parts per million.

The forward model for the airborne MWR, i.e. HAMP, is also based on a radiative transfer model. It uses the same absorption model for gas and liquid water as in the ground-based case. Nevertheless, the radiative transfer equation changes to eq. 2.10. This equation requires the knowledge of the sea surface temperature and the surface emissivity. Both are estimated from the closest point (in time and space) of the ERA-Interim reanalysis surface data (see section 2.4.6).

3.3 Summary

The chapter started with an introduction to the general optimal estimation theory, describing the different elements needed to define the retrieval algorithm, i.e. atmospheric state x, a priori information x_a and S_a, instrument measurement y and its uncertainty S_ϵ and forward model $F(x)$.

After that, the LIME SOAP algorithm is described, which is a synergetic retrieval method combining MWR and lidar measurements based on the optimal estimation theory. LIME SOAP is applied to different scenarios in different weather conditions, i.e. ground based perspective during HOPE and airborne viewpoint during NARVAL. The elements constituting the algorithm change depending on each specific application. A detailed description on how they are chosen and calculated for the different scenarios has been presented.

4

Absolute humidity retrieval - ground based

The algorithm that combines lidar and microwave radiometer (MWR) measurements, i.e. **Li**dar and **M**icrowav**e** **S**ynergetic **O**ptimal **A**tmospheric **P**rofiler (LIME SOAP), has been described in chapter 3. The current chapter presents its first realization and pursues two main aims: the first is to present the LIME SOAP application to the retrieval of absolute humidity (AH) profiles from the ground base perspective; the second is to evaluate the results in order to show the MWR+lidar synergy benefits.

For such aims, the data collected during HOPE (section 2.1.1) is used. In the first section of this chapter, the algorithm is applied to a single case study, whereas section 4.2 evaluates LIME SOAP when applied to the two months period of HOPE. The improvements of the synergy will be analyzed in terms of several parameters, like the reduction of the theoretical error or the increase of the degrees of freedom per signal (DOF), showing significant advantages with respect to the two instruments working separately.

4.1 Case study

LIME SOAP is applied to optimally combine the BASIL Raman lidar (RL) (section 2.3.2) and the HATPRO MWR (section 2.2.2) measurements to retrieve atmospheric AH profiles (in kg/m^3) during HOPE. The algorithm setup is designed such that one can work with input from a single instrument, i.e. only MWR data or only RL data; or with the two of them simultaneously, i.e. MWR+RL information. This aspect will allow to compare the performance of each sensor working individually in contrast to the combination of the both.

In the following, we demonstrate the algorithm presenting results for a case study, i.e. the 24th of April at 11 UTC, where a collocated radiosonde launched 4 km away from the RL and the MWR is used as reference (figure 4.1). Three different results are compared for three observation vector configurations: y contains only-RL measurements, y contains only-MWR information

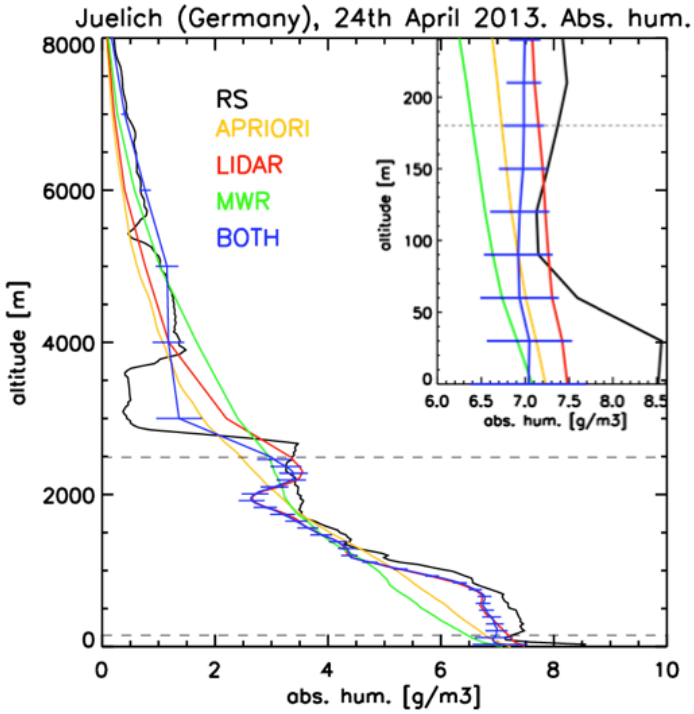

Figure 4.1: Absolute humidity profiles on the 24th of April at 11 UTC for a priori (yellow), only-RL (red), only-MWR (green) and MWR+RL (blue). The RS is used as reference (black). The dashed horizontal lines enclose the region where the lidar data is used. The inset is a zoom for the region close to the ground, between 0 and 250 m.

and y contains the two sensors measurements (MWR+RL). In the three cases, the retrieved atmospheric state x is the AH profile. Its vertical retrieval grid has 30 meters layers from ground to the highest RL valid point (to match the RL resolution). From this altitude upwards, only one point each 1 km is retrieved, because actually the MWR cannot provide more useful information to these higher layers. The a priori profile x_a (calculated as in section 3.2.1.1), which is the prior atmospheric knowledge, serves also as the starting point (first guess) for the first iteration in the main LIME SOAP equation (eq. (3.2)).

At first, the LIME SOAP observation vector y is defined as the portion of the water vapor mixing ratio (WVMR) RL profile (i.e. from 180 m to 2.5 km, ~ 77 layers) where the RL data has passed the quality threshold, i.e. relative measurement error smaller than 100% (see section 3.2.2). Note that MWR measurements are not taken into account yet. The result of the algorithm x_{op} is a complete profile from ground up to 10 km. In the region with lidar availability, x_{op} is strongly constrained by the lidar observations, since the associated measurement uncertainties are small (on the order of 0.5 g/m^3). In the regions with no RL data, the profile x_{op} is completed with the information provided by the a priori profile x_a and the a priori covariance matrix S_a.

Second, when only the 7 TBs in the K-Band of the MWR are introduced in the LIME SOAP observation vector y, a very smooth profile x_{op} is obtained. This is because the 7 frequencies

do not provide enough information to resolve fine vertical structures: MWR can only provide ~ 2 DOF per profile, as already mentioned in section 2.2. Therefore, the a priori profile plays a dominant role for defining the vertical structures.

Finally, the vector y is formed by the MWR TBs and the RL WVMR. The retrieved AH profile x_{op} is strongly constrained to the RL observations in the region where RL data has been considered valid, i.e. from 180 m to 2.5 km. Outside this region, the profile is completed based on the information provided by the TBs and the a priori.

The profile obtained with the MWR+RL combination best fits the RS, used as reference (see figure 4.1). Only the MWR+RL retrieval can detect the drop in humidity at 3 km and the increase at 5 km. This is due to both the additional microwave radiometer observations as well as propagated lidar information via the a priori covariance matrix. It is interesting to pay attention to the retrieval in the lowest atmospheric layers. In figure 4.1, a zoom from 0 to 250 meters is shown. Due to the missing RL information below 180 meters, the MWR+RL combination tends to the MWR values close to the ground, but quickly approaches to the lidar, as soon as the first RL values are available. One can see that the lowest values of the RS are $1 - 1.5 g/m^3$ more humid than the rest of the profiles. This might be explained by the fact that the sonde has been launched under different local environmental conditions: while the instrument site is located inside a research center, the RS is launched in an open field area. In addition, the venting of the RS is not optimal in the lowest ~ 100 m. These could cause slight differences in the comparisons close to the ground, but should not be a problem in the free troposphere.

As already discussed, a major advantage of LIME SOAP is that it can provide an a posteriori covariance matrix S_{op} for the retrieved x_{op} (eq. (3.5)). Thus, the theoretical error (in kg/m^3) associated to each altitude of the retrieved x_{op} profile is calculated as the square root of the main diagonal elements in S_{op}. The resulting MWR+RL theoretical error is small ($\sim 0.5 g/m^3$) in the region where RL data is available, but it increases with altitude, as to be expected. It is also slightly larger close to the ground ($\sim 1 g/m^3$), due to the absence of lidar data. Throughout the profile, the MWR+RL theoretical error is smaller than in the only-RL and only-MWR cases. (see section 4.2.3 for detailed uncertainty statistics). Nevertheless, the two latter are not presented in figure 4.1 for the sake of simplicity.

One can additionally evaluate the quality of the retrieval by calculating the *effective* vertical resolution (equation (3.7)). Figure 4.2 presents the vertical resolution Δz calculated for the three different retrievals on the 24th of April 2013, at 11 UTC. The results nicely show the improvements of the MWR+RL combination. In the region where RL is available (from 180 m to 2.5 km), the only-RL resolution is high ($\sim 100 - 300$ m). But outside this region the vertical resolution for only-RL adopts the value of infinite because the information content on these layers is zero. The only-MWR resolution is coarser in all the altitudes: up to 2.5 km it presents values one order of magnitude larger than the other two cases. Nevertheless, the advantage of the MWR is that the instrument provides information throughout the complete profile. Finally, the MWR+RL

case presents the lowest vertical resolution: it adopts similar values as the only-RL resolution when RL is available, and improves the resolution by $\sim 1-2$ km compared to the only-MWR case in the rest of the profile. Since the MWR+RL solution is strongly constrained by the lidar measurements between 180 m and 2.5 km, the additional information contained in the MWR observations is mainly distributed in the region above the 2.5 km.

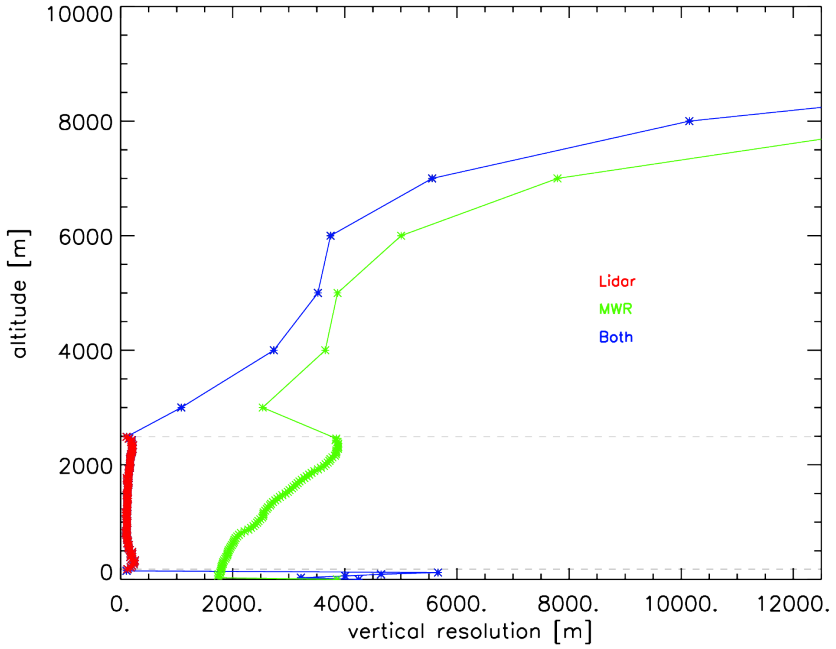

Figure 4.2: Vertical resolution for the only-RL (red), only-MWR (green) and MWR+RL (blue). The dashed lines enclose the area where RL data has been considered.

The same methodology is now applied to a larger measurement period. An example of this is shown in Figure 4.3, which presents a 7-hour time series of the absolute humidity on the 17th of April 2013, during HOPE. The figure shows the effect of a cold front passage around 23 UTC leading to an intrusion of dry air into the lower altitudes. Above 5 km, no significant changes of humidity occur. The time series reveals a successful synergy between RL and MWR, making use of the TB and a priori information to complete the profile where RL measurements are not available (i.e. in the blind region below 180 m and at regions of too high a lidar noise level).

4.2 Statistical assessment

LIME SOAP has been applied for retrieving AH to all the clear sky periods with simultaneous availability of MWR and RL. The MWR measured continuously during the campaign, so this selection is restricted to lidar availability. There are in total 4201 lidar profiles (30% of the total campaign). Out of them, 717 profiles are considered clear sky (around 17% of the total). From the clear sky profiles, the convergence of LIME SOAP is found in 95.8% of the cases, that is, 687

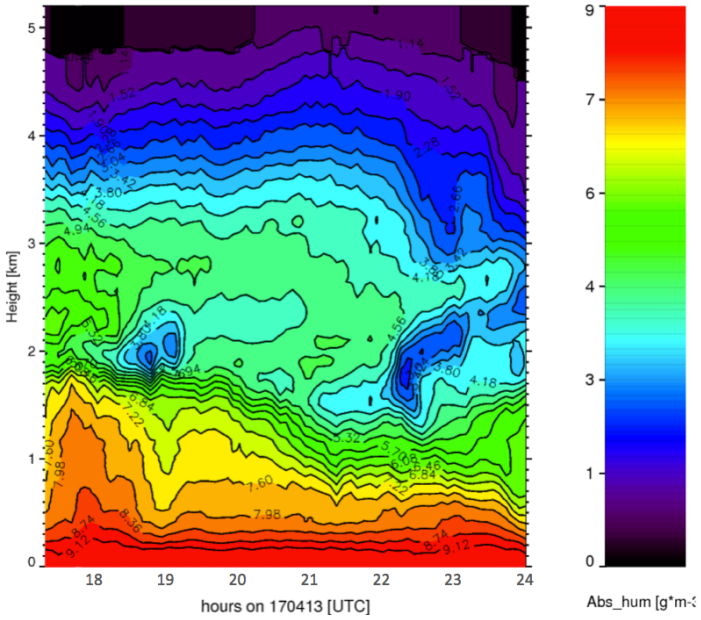

Figure 4.3: Time series of the retrieved absolute humidity by combining MWR+RL, in the afternoon of the 17th April 2013.

profiles. In the remaining 4.2% of the cases, convergence is not reached because the algorithm could not find a solution which is simultaneously consistent with the measurements of the two instruments and the a priori, within their uncertainties.

4.2.1 IWV assessment using GPS

Once LIME SOAP has been applied to all the clear sky periods in HOPE for AH, a key atmospheric parameter to evaluate is the integrated water vapor (IWV). This evaluation is used not only for learning about the IWV evolution during HOPE, which is studied in more detail by Steinke et al. (2014a), but also as a consistency check for the retrieved AH profiles. The independent measurements of IWV from the Global Position Satellite (GPS) (Bevis et al., 1992) (see section 2.4.2) are used to assess the quality of the retrieval products. Figure 4.4(a) presents the time series of the IWV during HOPE, showing the continuous IWV from GPS and the IWV calculated from the LIME SOAP retrieved AH, which is only available during clear sky events. The 2-months IWV time series reveals strong fluctuations with values between 5 and 29 kg/m^2.

Figure 4.4(b) quantitatively compares the IWV calculated from the three AH retrieval cases (i.e. MWR+RL, only-MWR and only-RL) against the GPS signal. Note, that a comparison with the original lidar data before processing in LIME SOAP is not sensible, since the lidar lacks information in the lowest atmosphere (due to incomplete overlap) and also above the altitude where the SNR is too large. A sensible comparison is only carried out after LIME SOAP processing because the result of the retrieval is a full profile.

Figure 4.4(b) also shows the values for the bias and the standard deviation (in kg/m^2) for all

the cases. In all three situations, the values lie in the GPS uncertainty of 1-2 kg/m^2 (Gendt et al., 2004) and the MWR product of $\sim 0.5-1\ kg/m^2$ (Steinke et al., 2014a). The combination of the two instruments and the only-MWR case present similar standard deviations, whereas the only-RL case presents a twice as large standard deviation in comparison to the other two cases. These numbers confirm that, though the RL is essential for retrieving a water vapor profile, it does not provide any additional information to the calculation of the IWV, which is already accurately provided by the MWR. In addition, this result demonstrates that the retrieved LIME SOAP water vapor profiles are well constrained with respect to the integrated value.

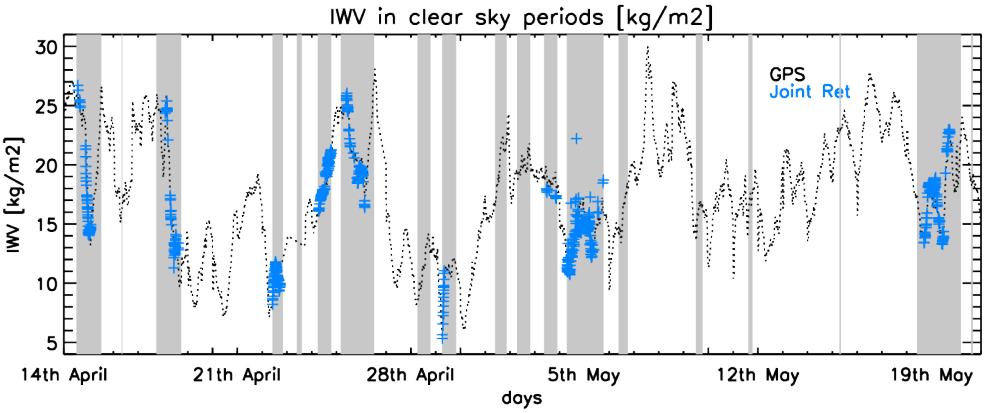

(A)

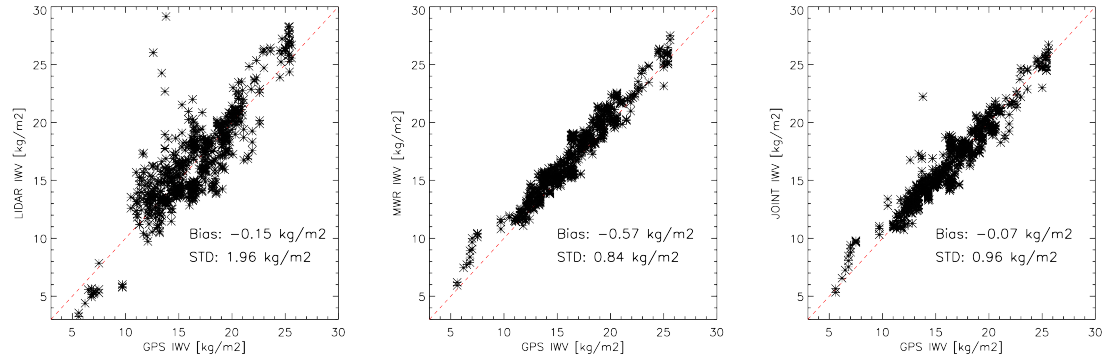

(B)

Figure 4.4: (A) Time series of IWV during the complete HOPE period for clear sky cases from: the GPS signal (black) and the one calculated from the joint retrieval, available only in clear sky cases (blue). Shaded areas represent the RL availability. (B) From left to right, scatterplots of the IWV calculated from the AH retrieved in the cases: only-RL, only-MWR and MWR+RL; against the GPS.

4.2.2 Comparison with radiosondes

As explained above, the retrieval grid of each profile changes depending on the amount of *useful* RL data, which is affected by the atmospheric conditions, background noise, etc. In order to clearly assess the benefits of the sensor synergy, a different retrieval strategy is used for the

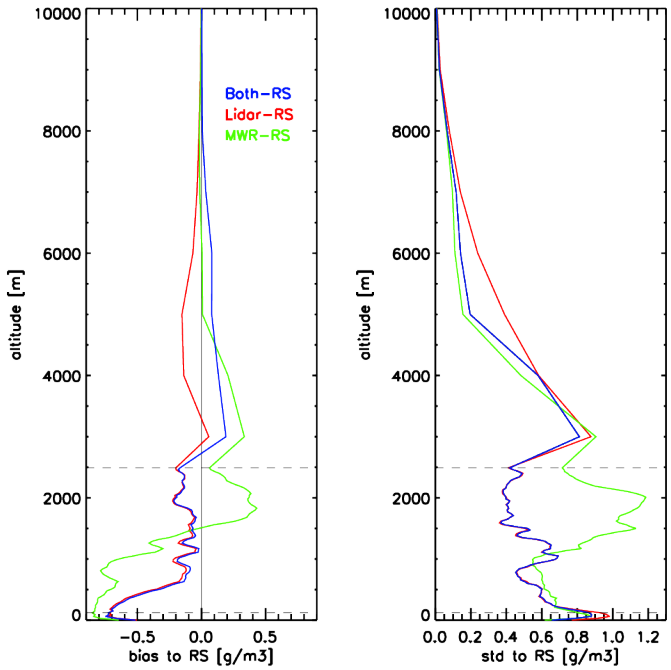

Figure 4.5: Mean and standard deviation of the difference between the 18 clear sky radiosondes: MWR (in green), RL (in red) and the combination of both (blue). The dashed horizontal lines enclose the region where the lidar data is used.

current test: the algorithm is applied using RL profiles artificially clipped at a fixed altitude. This strategy, which will be used as well from section 4.2.3.2 until the end of the current chapter, allows to retrieve all AH profiles using the same vertical grid, which facilitates consistent comparisons and statistics.

The defined clipping altitude is 2.5 km, chosen in order to keep at least 75% of the profiles within the statistics (only 23% of the considered RL profiles reach 100% relative measurement uncertainty at a height lower than 2.5 km). In the case that a given RL profile gets too noisy at a hight lower than the clipping altitude, the profile is discarded and not taken into account for the statistics.

This strategy also simplifies the separate study of three atmospheric regions, defined as follows:

- Region a) from ground to 180 m: no lidar data is available
- Region b) from 180 m to 2.5 km: the only domain where RL data is used.
- Region c) from 2.5 km to 10 km: no lidar data is considered, though it could be available.

At first, a comparison of the retrieved AH profiles with the radiosonde (RS) profiles is performed. Unfortunately, only 18 valid clear sky RS have been found during the periods

where BASIL measured. In figure 4.5, the bias and the standard deviation (STD) to the 18 RS are presented for the three cases: only-MWR, only-RL and the MWR+RL combination.

Region (a), exhibits the largest STD and biases, with similar values for the three cases. In addition to the fact that no lidar data is available in this region, this result may be due to different surface-related local effects at the site where the RS was launched ($\sim$ 4 km distance) and at the site where the instruments measure. In addition an insufficient venting of the RS in the lowest 100 m may act as an additional uncertainty.

In region (b), the biases and STD for the only-RL and RL+MWR are similar, revealing the only-MWR the largest values. The similarity between only-RL and RL+MWR is again explained by the small uncertainty associated to the lidar measurements. The product of the combination tends to the lidar data when available, as seen in section 4.1. From $\sim$ 500 m to 2.5 km, both only-RL and RL+MWR show a small bias on the order of $\sim 0.2\ g/m^3$, but below this altitude the deviation increases up to $\sim 0.75\ g/m^3$. This fact may suggest that the lidar data in the lower 500 m could have some additional issues with the RL overlapping function (OVF). This feature will be examined in more detail in section 4.2.3.2.

In region (c) all the three values for the different retrievals are similar. The only-MWR performs best when comparing to the RS, because both its bias and STD are the smallest. The only-RL case presents the largest bias and STD because in this region only information from the a priori is provided. The combination of the two sensors presents intermediate values, however more similar to the only-MWR case.

Unfortunately, this set of only 18 radiosondes does not allow a significant assessment of the synergy benefits. In addition, when interpreting the results in figure 4.5, one must take into account that the RS itself presents some sources of uncertainty which are not easy to quantify, e.g. the launch distance of 4 km to the instrument site, drifts of the balloon, dry bias, etc. Because of that, other parameters that assess the a posteriori information content of the retrieval are needed to further evaluate the synergy advantages. The theoretical uncertainty of the retrieved AH profiles is one of these parameters, which is studied in the following subsections.

4.2.3 Theoretical error

As previously mentioned, the algorithm provides an estimation of the a posteriori error for the retrievals. This theoretical error is computed for every retrieved AH profile in the three different cases: using only-RL, only MWR and the RL+MWR combination.

At first, section 4.2.3.1 presents a separation between day and night time measurements, since the RL performs best in dark environments when the background noise is lower. Section 4.2.3.2 presents different results and sensitivity studies using the RL clipping strategy.

4.2.3.1 Day and night measurements theoretical error study

In order to investigate the algorithm performance during day- and nighttime separately, figure 4.6 is presented. Figure 4.6(a) shows the mean theoretical errors for the three algorithm setups, differentiating between day-time and night-time. Note that, in this study, no clipping is performed in the measurements, and thus, we cannot distinguish three regions according to lidar availability. The clipping altitude and region separation will be used again in next sections.

Figure 4.6(b) presents the number of RL profiles reaching each specific altitude. Note that, for the sake of comparability, the theoretical error for each of the three retrieval cases have been averaged over the same number of profiles. As discussed in section 2.3.2, the lidar performance is much better during nighttime, when more than 50% of the lidar data reach a maximum useful altitude of around 7 km. The theoretical error profile during night is also lower than during daytime (i.e. about a factor of three smaller at an altitude of 4 km), as expected. During daytime, the highest useful lidar range reaches only a maximum altitude of around 5.5 km. In addition, only half of the profiles reach values higher than 3 km. Under these situations, the MWR information is expected to be a more powerful supplement to the lidar information. This is well seen in the improvement of theoretical error from 3 to 5 km in day-time measurements. The addition of the MWR measurements improves the theoretical error by approximately a 25% in this region. The only-MWR case remains almost invariable, because the instrument performance does not change with the background light conditions.

4.2.3.2 Clipped RL profiles for theoretical error study

Another theoretical error analysis is performed clipping all lidar measurements at 2.5 km, following the same argumentation as in section 4.2.2. This way, the three previous atmospheric regions (a), (b) and (c) defined in section 4.2.2 can be distinguished according to RL availability. Note that this simplification of the problem allows to clearly specify the relative impact of MWR and RL in the different LIME SOAP retrievals.

Figure 4.7 presents the a priori uncertainty, as well as an average over the 636 theoretical error profiles calculated after running LIME SOAP for all the HOPE clear sky periods. Clearly, the uncertainty associated to the a priori is the largest, as it represents the atmospheric variability within the HOPE period. When only the TBs of the MWR are used in the LIME SOAP, the average error estimate is reduced at least by half throughout the whole atmosphere with respect to the a priori uncertainty. When only the lidar information is used in the AH retrieval, the error in region (b) is strongly reduced with respect to the other two previous cases. Compared to the only-MWR error, which has an average of $\sim 0.7\ g/m^3$, the only-RL is lowered to almost $0.1\ g/m^3$. In regions (a) and (c) the only-RL error is larger than in region (b) because no lidar data is available and thus only the a priori information is used to complete the profile. The only-RL uncertainty is indeed especially large above 3 km, where it tends to the a priori uncertainty, presenting even

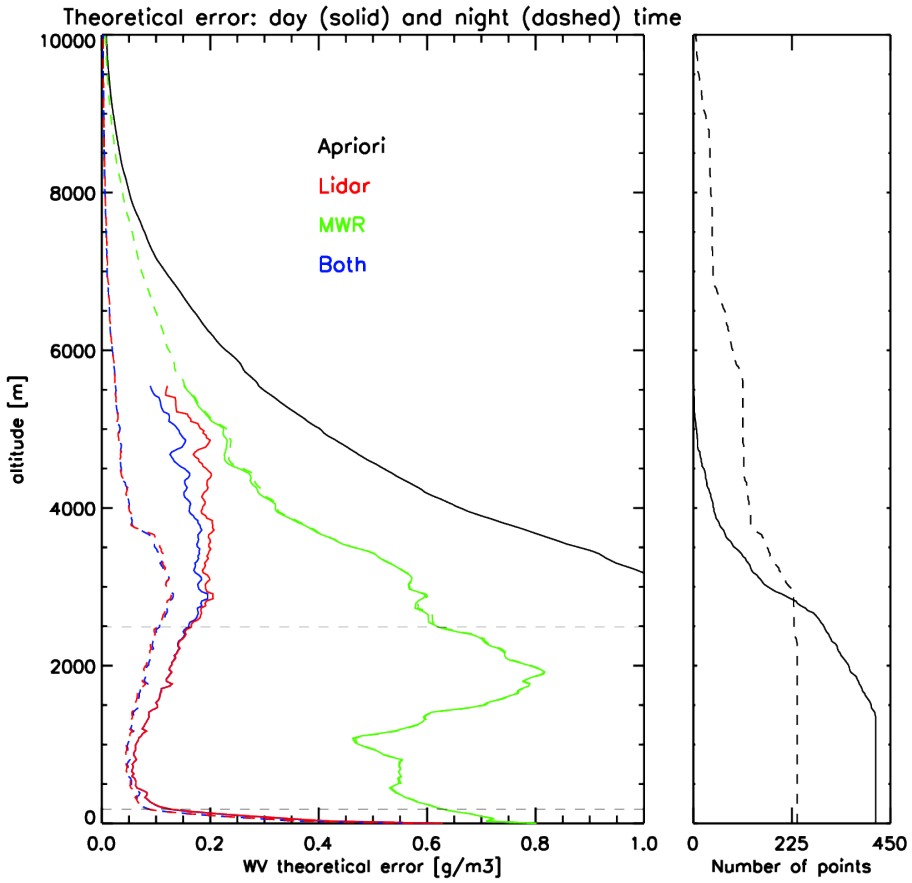

Figure 4.6: Left: mean theoretical error over the 636 clear sky cases during the complete HOPE period, separated into daytime (solid) and nighttime (dashed) measurements. In black: a priori uncertainty (lowest 3 km are out of margins). Red: only-RL. Green: only MWR. In blue: the MWR+RL. Right: number of RL profiles reaching each altitude, corresponding to the number of profiles used to calculate the average in the left panel.

larger values than the only-MWR error.

However, when the RL+MWR retrieval is performed, the resulting error is the smallest for all the altitudes. In region (b), the error is almost the same than for the only-RL case. Outside this region, the MWR contribution plays an important role to reduce the uncertainty: in region (c), from average uncertainty values of 0.17 and 0.22 g/m^2 for only-MWR and only-RL respectively, the uncertainty of the combination is reduced to an average value of 0.12 g/m^2. Similarly, in the lowest region, the average error for the combination is 0.30, in comparison to 0.71 and 0.33 g/m^2 for the only-RL and only-MWR cases, respectively.

In general, one can say that there is a clear improvement in the theoretical error due to the synergy of the two instruments. One can quantify the relative error reduction err_{red} of the MWR+RL retrieval in comparison to the only-MWR and only-RL retrievals. This value can be

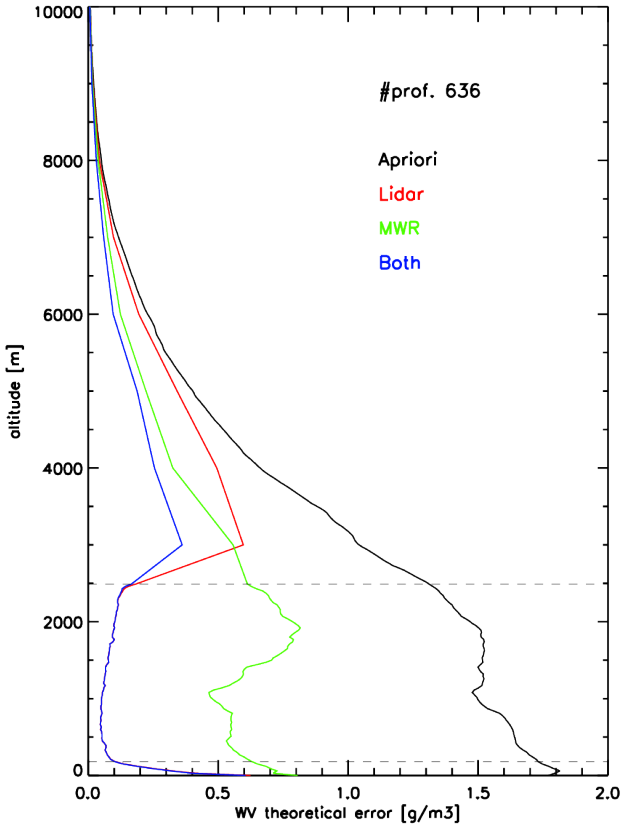

Figure 4.7: Mean theoretical error over the 636 clear sky cases during the complete HOPE period. The lidar data has been artificially cut-off at 2.5 km. In black: a priori uncertainty. Red: only-RL. Green: only MWR. In blue: the MWR+RL. The dashed horizontal lines enclose the region where the lidar data is used.

calculated as the difference between the single-instrument and joint theoretical error profiles, divided by the single-instrument one. That is:

$$err_{red,i} = \frac{err_i - err_{MWR+RL}}{err_i} \cdot 100 \tag{4.1}$$

where $i = [RL, MWR]$ and represents the averaged error profiles when only-RL and only-MWR are used (see figure 4.7). Then, $err_{red,i}$ is a profile representing a relative error reduction as a function of the altitude. The average error reduction for the AH in the complete atmospheric profile is 60% (38%), with respect to the retrieval using only-MWR (only-RL) data. This improvement is especially clear in region (c), where lidar data are not available. The improvement of the combination in region (a) is better analyzed with the experiment in the following section.

Sensitivity study 1: lower atmosphere

As argued in section 4.2.2, the high bias values for only-RL and RL+MWR from ground up to 500 m (figure 4.5) might reveal a problem with the lidar OVF in this region. If it was the case and in

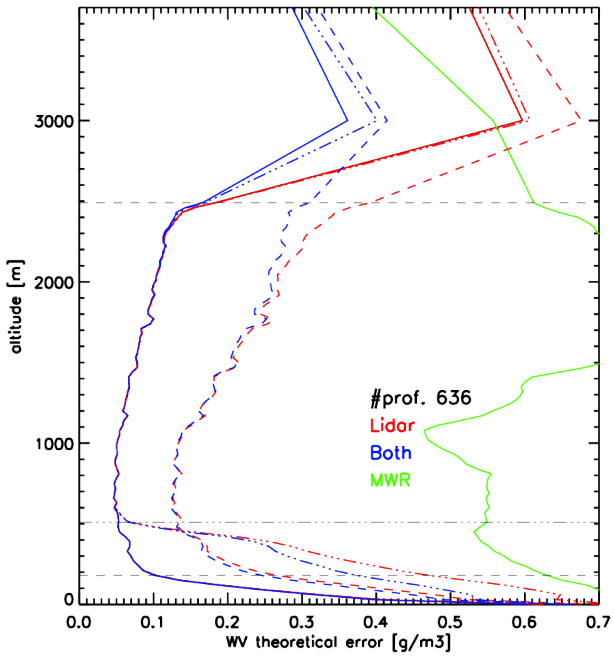

Figure 4.8: Mean theoretical error over the 636 clear sky cases during the complete HOPE period. Red: only RL has been introduced in the algorithm. Green: only-MWR. In blue, the combination of RL and MWR. The dashed horizontal black lines define the region where lidar data has been considered available. The dashed red and blue lines represent the result when the lidar uncertainty has been incremented by a factor of four. The dotted-dashed red and blue lines correspond to the case where lidar data has been suppresed from ground until 500 meters. Solid lines show the errors without increments, as shown in figure 4.7.

order to asses the retrieval performance, the hypothesis of a larger RL zero-overlap region (ZOR) is assumed. Under this hypothesis, a new ZOR is defined so that there are no valid measurements in the lowest 500 m, instead of the previous ZOR of 180 m. Thus, lidar data from 180 to 500 meters is discarded for all the profiles. The algorithm is run again for the complete HOPE period taking this condition into account.

Figure 4.8 shows the mean theoretical error for the cases of expanded ZOR (up to 500 m) and the initial BASIL ZOR (up to 180 m). In both cases, the results are very similar in regions where the RL data is available, i.e. from 500 m to 2.5 km, with the theoretical error of the MWR+RL matching that of the only-RL. However, in the lower region of the increased ZOR, the MWR+RL error is smaller than the only-RL case: there is an uncertainty reduction at the ground level of about $0.1 g/m^3$, which is gradually reduced towards the region where RL data are available. This result nicely shows the synergy benefit of both instruments in the atmosphere below 500 m, where the MWR contributes more significantly. Above this point and up to 2.5 km, the error is almost equal for the cases of initial ZOR and increased ZOR. From 2.5 km to 10 km, the increased ZOR shows a slight increase in theoretical error of $\sim 0.05\ g/m^3$ and $\sim 0.02\ g/m^3$ for the RL+MWR

Table 4.1: Degrees of freedom for signal comparison for absolute humidity. Average over 636 profiles. The atmosphere is separated in three regions according to lidar availability. The DOF are presented for three cases: only RL, only MWR and the combination of both instruments. In the upper part, no increment on the RL uncertainty has been considered. In the bottom part, the RL uncertainty has been multiplied by a factor of four.

Region	RL	MWR	Combination
a) Ground to 180 m	0.00	0.07	0.03
b) 180 m to 2.5 km	25.90	1.01	25.75
c) 2.5 km to 10 km	0.00	1.18	1.69
Total	25.90	2.26	27.47
Region	RL	MWR	Combination
a) Ground to 180 m	0.00	0.07	0.06
b) 180 m to 2.5 km	12.19	1.01	12.11
c) 2.5 km to 10 km	0.00	1.18	1.57
Total	12.19	2.26	13.74

and only-RL cases, with respect to the initial ZOR. This is because the MWR information content is redistributed and more efficiently used in the lower layers of the atmosphere.

Sensitivity study 2: Increase of the RL error

In section 3.2.2, the components of the covariance matrix S_e have been determined to the author's best knowledge. However, it might be possible that additional uncertainty sources exist. In order to better understand the impact of the lidar uncertainties, a sensitivity study increasing the lidar uncertainty is performed.

The increase on the RL measurement uncertainty is chosen based on the discrepancy between the theoretical error (figure 4.7) and the deviations to the RS (figure 4.5) at around 2 km. The values are approximately 0.1 g/m^3 and 0.4 g/m^3 respectively, showing that the deviation to the RS is four times larger than the calculated only-RL theoretical error. Since this factor represents an upper uncertainty limit, the RL measurement uncertainty is incremented by a factor of 4 to study the sensitivity of the retrieved profile error with respect to the RL measurement uncertainty.

The results of this test are plotted in figure 4.8, together with the initial values (without increment), for the only-RL and MWR+RL cases. Note that the only-MWR case remains exactly the same. The new averaged errors are a very similar at the ground, but they increase by a factor of 2 to 3 in region (b). In case of increased RL uncertainties, the difference between the errors of the only-RL and RL+MWR (dashed lines) is more noticeable than in the original case (solid line), especially from 2 km upwards. Note that already at 2.5 km, the error reduction for including the MWR, reaches values close to $0.1 g/m^3$. Thus, as expected the synergy benefit increases.

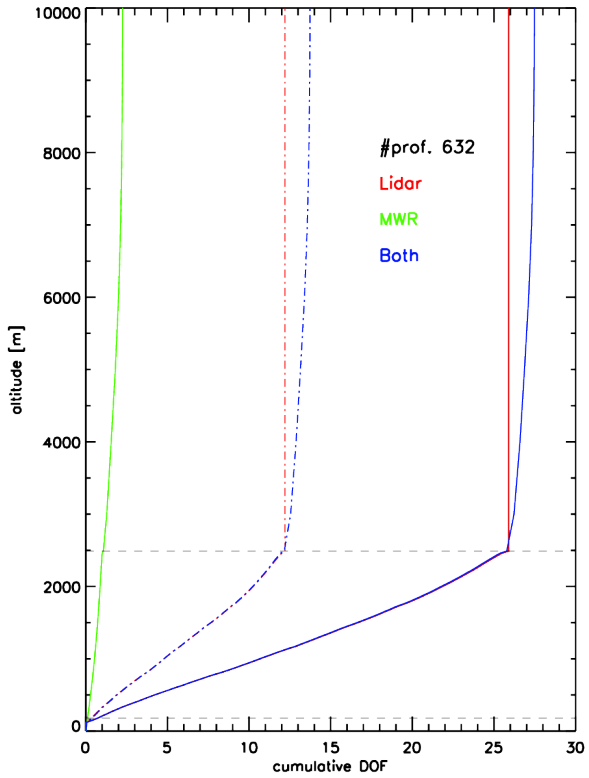

Figure 4.9: Cumulative degrees of freedom per profile for the different instrument combinations: in red, only-RL; in green, only-MWR and in blue, the combination of the two sensors. The dotted-dashed lines represent the degrees of freedom for the case where the RL uncertainty has been multiplied by 4. The average number of DOF in every region are summarized on Table 4.1. The dashed horizontal grey lines enclose the part of the atmosphere where lidar data has been considered. The number of elements in the measurement and state vectors are 77 (66 for the dashed case) and 91 respectively.

4.2.4 Information content analysis

4.2.4.1 Degrees of freedom per signal

The benefit of the combined retrieval can also be analyzed by means of the DOF (figure 4.9), which allow to study the amount of information provided by the different instruments for the different altitudes. Figure 4.9 represents the vertical profile of cumulative degrees of freedom (CDOF) for the different instrument combinations, obtained as an average over 636 profiles. In the case of only-MWR, the CDOF are smaller than for the other cases, reaching a maximum of about 2 at 10 km. This result agrees with previous studies (Löhnert et al., 2007). Wherever lidar is available, the CDOF increase linearly, thanks to the lidar information content. In the case of only-RL, above 2.5 km the cumulative DOF remain constant because no additional information is introduced. However, for the RL+MWR case the CDOF increase above 2.5 km thanks to the inclusion of the MWR measurements.

Table 4.1 summarizes the values in the different atmospheric regions of figure 4.9. For the only-RL case: in the regions where no lidar data is available ((a) and (c)), the DOF are, as expected, zero. In region (b), the total number of average DOF are around 26, which means that the lidar with the assumed S_e and the constraint provided by S_a provides 26 independent pieces of information for AH retrieval. The total average number of DOF in the column is largest for the combination of the two instruments, increasing in almost 2 DOF with respect to the only-RL case. The numbers for the MWR+RL combination show that the inclusion of MWR results mainly in an increase of DOF (+1.7) in region (c), whereas in region (b) the DOF remain almost the same. This implies that part of the 2.26 DOF contained in the only-MWR retrieval for the complete profile have now been *re-distributed* into the region above 2.5 km.

When the increment in the RL uncertainty from the *Sensitivity study 2* is considered, the amount of useful information provided by the RL is smaller, and thus the DOF are reduced. This reduction can been seen in all regions where the RL is involved (figure 4.9). In case of an uncertainty increase of a factor of 4 the total average DOF are reduced by a factor of ~ 2. Note, that the DOF values for the MWR only retrieval remain the same.

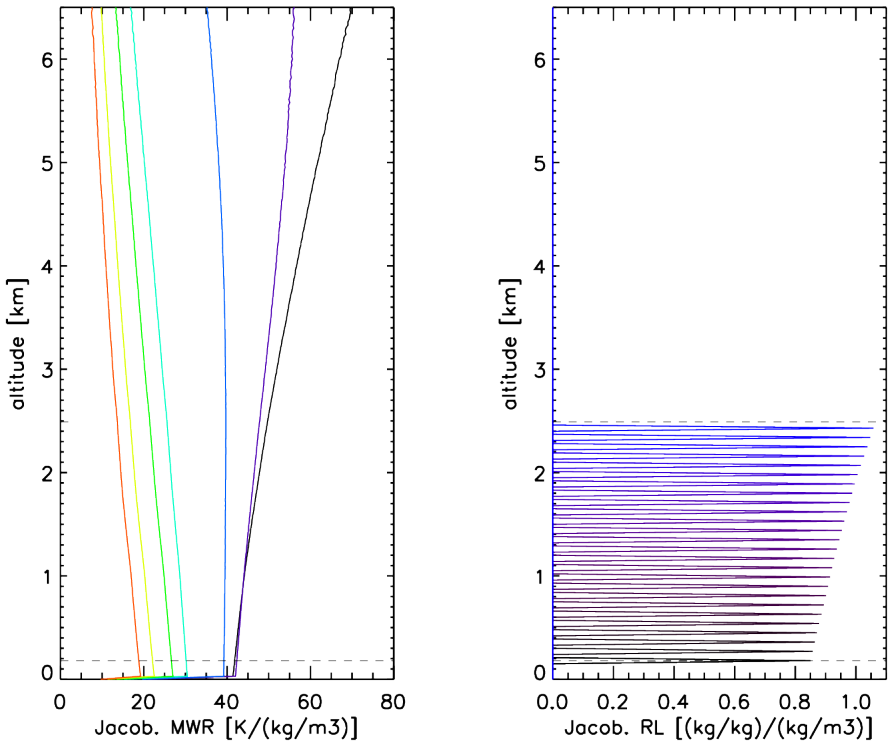

Figure 4.10: Jacobian for the MWR (left): each line corresponds to a frequency channel. The orange is the most transparent channel, i.e. 22.24 GHz, the black, the most opaque at 31.40 GHz. Jacobian for the RL (right): each line corresponds to a different WVMR altitude, shown only every 90 m for clarity. The dashed lines enclose the area where RL data has been considered.

4.2.4.2 *Extended information content analysis: Averaging kernels and Jacobians*

In addition to the DOF, there are other parameters which serve to understand the quality of our retrieval, e.g. the averaging kernel matrix (equation (3.6)) and the Jacobian (equation (3.3)).

Figure 4.10 presents the Jacobians for the MWR and RL corresponding to the retrieval in figure 4.1, on the 24th of April 2013 at UTC. The Jacobian can be understood as the response to a variation on the observation vector y when an element on the state vector x, i.e. an atmospheric layer, is perturbed. The MWR Jacobian has seven lines, each of them corresponding to a channel of the K-band. The most transparent channels, i.e. 22.24 GHz, induce a smaller variation on the upper atmosphere. The more transparent channels, are more sensitive to variations in the higher atmospheric layers, e.g. the 31.40 GHz channel. The Jacobian for the lidar is zero where no RL is available, and composed of Dirac delta functions at the rest of the altitudes, adopting values close to one, which represent the conversion from WVMR to AH. This means that a variation performed on a layer with RL measurement availability, affects only to this layer and the rest remain the unperturbed. The reasons for that are two. First, because of the definition of the S_ϵ, where the measurement error is assumed independent from the other measurements, i.e. S_ϵ is a diagonal matrix. Second, because the retrieval vertical grid for x has the same vertical separation than the RL measurements in y.

Because the retrieved parameter x is a vertical atmospheric profile, the A_k columns represent the information distribution of the retrieved profile as a function of the altitude. For the sake of clarity, the averaging kernels have been plotted for a AH profile retrieved with constant retrieval grid with 30 meters separation. Figure 4.11 shows the A_k corresponding also to the case study in figure 4.1, where the lidar useful data covers the region from 180 meters to 2.5 km. In addition, figure 4.11b is presented as a tool to better understand figure 4.11a. The first considers the same retrieval profile than figure 4.11a but takes into account a diagonal S_a in the retrieval calculation, i.e. canceling the vertical correlations.

If the RL WVMR values are vertically independent, i.e. S_ϵ and S_a are diagonal matrices, the RL information at a given height will only affect this specific altitude. In the A_k, this is translated into Dirac deltas at each height were RL is available (see figure 4.11b). Instead, and because of the vertical correlation introduced by the off-diagonal elements in the a priori covariance matrix S_a (figure 3.1), the A_k columns present a smooth shape. This implies that the information from a given atmospheric layer is redistributed in altitude, affecting to the neighboring regions (figure 4.11a).

The only-MWR provides much lower information content, i.e. one order of magnitude smaller than the RL, as expected. If the a priori covariance matrix is diagonal, the strongest information content will be expected close to the surface, where the instrument is more sensitive (see figure 4.11b). Nevertheless, due to the altitude correlation defined by S_a, the information content is re-organized in the atmosphere, showing its maximum at ~2 km, i.e. the typical boundary layer

height. The A_k for the MWR+RL combination shows in both cases, i.e. figure 4.11b and 4.11a, how the information content of the two sensors is optimally combined.

4.3 Summary

The details of LIME SOAP applied to the AH retrieval from the ground-based perspective during HOPE have been presented in this chapter. To better understand the MWR+RL synergy, the AH retrieval has been applied to three different cases: when only MWR information is used, for only RL data and for the combination of the both sensor's data.

The chapter starts analyzing a simple case study, where the AH retrievals are compared to a RS, showing that the MWR+RL combination presents the best result w.r.t the reference. To further demonstrate the synergy benefit, the LIME SOAP is applied to a larger time series, i.e. the two months period of HOPE. The results are statistically analyzed in terms of several parameters. First, the IWV calculated from the AH retrievals is compared to the IWV from the GPS. The results show that, though the RL is essential for AH profiling, it does not provide additional information on the integrated water vapor amount, which is already accurately provided by the MWR. Second, an extensive analysis of the a posteriori retrieval error is performed, where several sensitivity studies are carried out. It has been also demonstrated that when applying the combined MWR+RL retrieval on average the theoretical uncertainty is reduced by 60% (38%) with respect to the retrieval using only-MWR (only-RL) data. The detailed analysis of the theoretical error allows to deeper understand not only the synergy benefit, but also how the initial measurement error definition might affect to our results. Third, a study of the retrieval information content by means of the DOF and CDOF confirms the outcomes by the previous sections. Finally, further information content parameters, i.e. the averaging kernels and Jacobians, are presented. These parameters aim to give some details about how the *useful* information is distributed on the retrieval.

In general, the results presented in this chapter confirm that the RL+MWR water vapor synergy is meaningful and advantageous. In addition, they suggest that a careful specification of the prior information as well as the instrument uncertainties, specially for the RL, is required. It has been also demonstrated that the a priori covariance matrix S_a plays an important role on the vertical distribution of the information because its off-diagonal elements establish a relation within the different atmospheric layers.

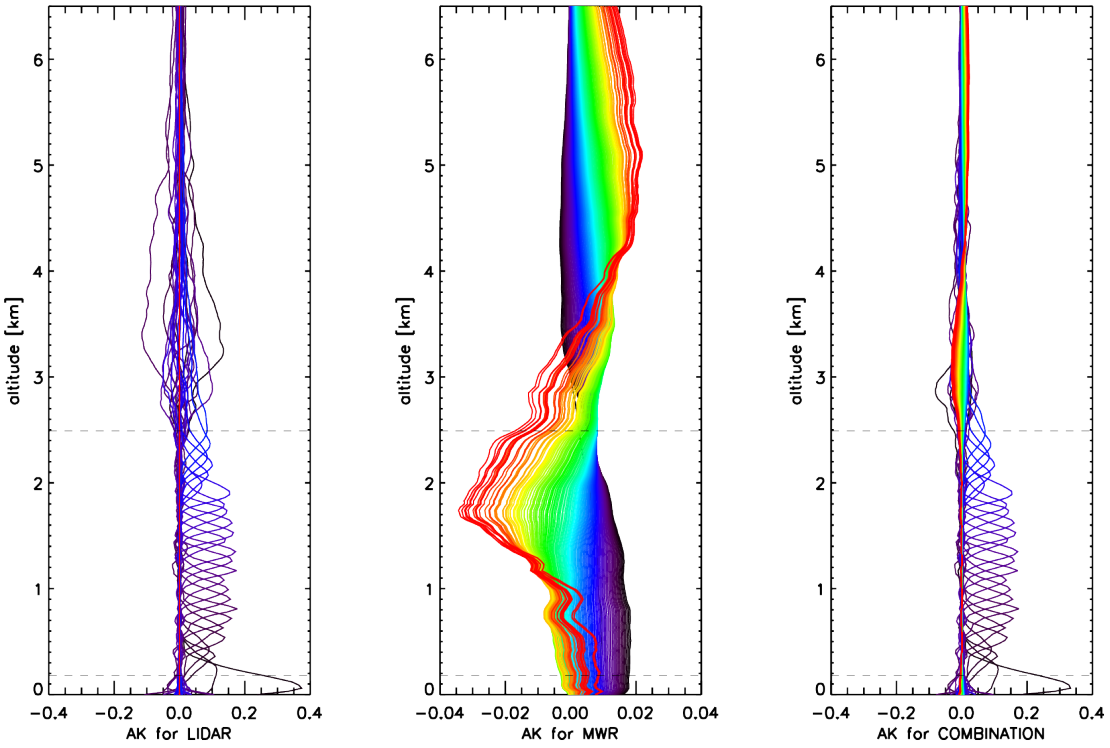

(A)

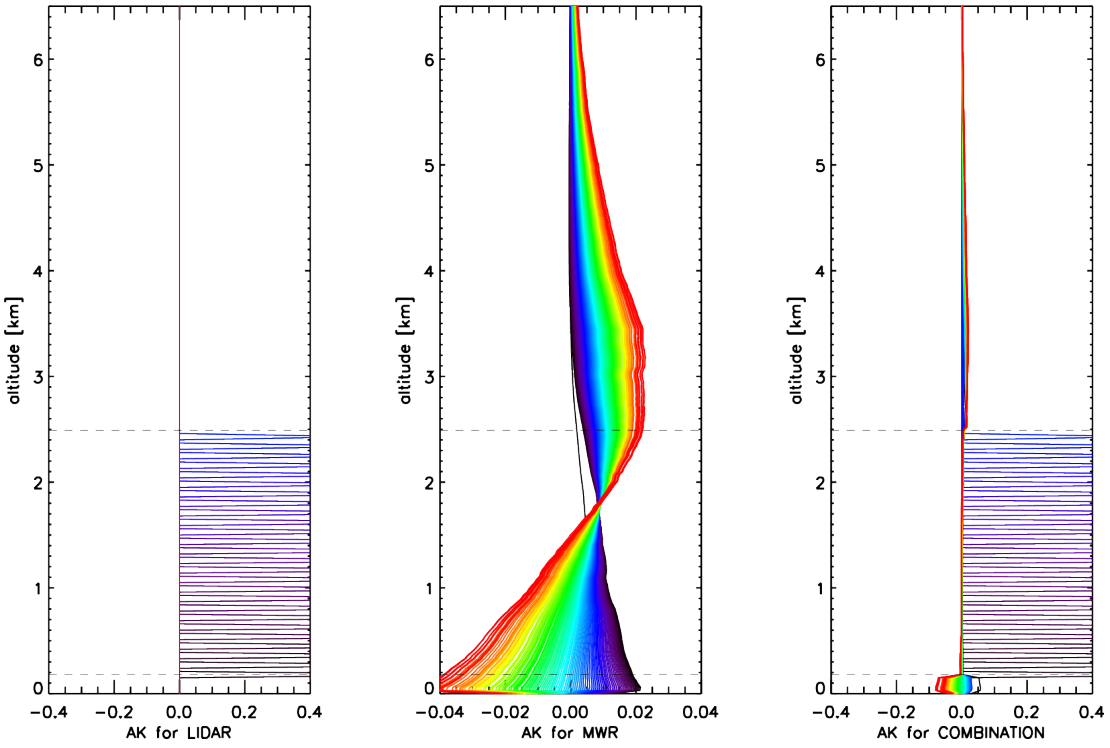

(B)

Figure 4.11: From left to right: averaging kernels of only-RL, only-MWR and MWR+RL. Each color corresponds to a different altitude: ground is represented by black, higher altitudes are represented with reddish colors. The bottom figure corresponds to the A_k calculated using a diagonal covariance matrix S_a. The averaging kernels are only shown every 90 m in altitude for clarity.

5

Temperature and relative humidity retrieval

In the previous chapter, LIME SOAP was used to retrieve atmospheric absolute humidity (AH) profiles by combining RL mixing ratio profiles and MWR brightness temperatures. In addition to water vapor measurements, both RL and MWR have the capability to provide atmospheric temperature (T) profiles (see sections 2.2.2 and 2.3.2), which allows the LIME SOAP application to the T retrieval. Moreover, knowing the distribution of AH and T leads to the possibility of retrieving relative humidity (RH) profiles.

In this chapter, the retrieval of T profiles will be presented and evaluated within a case study (section 5.1.1). Statistics over ~150 T retrievals will be analyzed in section 5.1.2. The RH retrieval will be presented in section 5.2, showing the benefits of the sensor combination. Because the lidar T is typically restricted to specific time periods or even not possible at all for some lidar systems (i.e. for WALES), a RH retrieval will be performed in the absence of lidar T information. This approach will be later used in chapter 7, where the lidar WALES only provides water vapor information.

5.1 Temperature

In this section, temperature profiles are retrieved by combining RL and MWR within LIME SOAP. Similar to the AH approach (chapter 4), LIME SOAP allows to work with one single instrument, i.e. only-RL or only-MWR, or with the combination of both, i.e. MWR+RL. This allows to compare the performance of the individual sensors to the combination of the two.

T profiles from BASIL and/or MWR brightness temperatures (TB) in the V-Band (along the 60 GHz oxygen absorption complex) are used in the observation vector y. As discussed in section 3.2.2, the angular information of the TB is used in the T retrieval because it increases the vertical information content, especially in the boundary layer, up to 2 DOF. The most beneficial scanning strategy (section 3.2.2.1) considers the four most opaque channels (i.e. 54.94, 56.66, 57.3 and 58

GHz) with their angular information (90, 42, 30, 19.2, 10.2 and 5.4 degrees) and the three more transparent channels (i.e. 51.26, 52.28, 53.86 GHz) with only their zenith measurements (Crewell and Löhnert, 2007). Note that, due to the way the RL T profile is obtained (see section 2.3.2), the non-overlap region for T is significantly higher than for the mixing ratio, e.g. for water vapor mixing ratio it is 180 m, while for T it is $\sim 500 - 2000$ m.

5.1.1 Case study

To demonstrate the performance of LIME SOAP applied to temperature retrievals, an example case study is shown. The algorithm is run for three different cases: using only the RL profile T information (only-RL), using solely the MWR TB (only-MWR) and using the information of the two instruments simultaneously (RL+MWR). Figure 5.1 shows the resulting profiles and their deviations with respect to the collocated radiosonde on 17th of April 2013, at 23 UTC. As in chapter 4, three atmospheric regions are differentiated according to lidar information availability with the aim of studying the individual instrument performance. For this particular profile the three regions are:

- Region a) from ground to 2.5 km, where the RL error is large due to overlapping function (OVF) problems or no lidar signal is available at all, i.e. the zero overlap region (ZOR).
- Region b) from 2.5 km to 7 km, the only domain where useful lidar data is available.
- Region c) from 7 km to 10 km, where the RL signal becomes too noisy.

When the algorithm is run with only-RL data, the retrieved profile presents a large error in region (a) where the difference to the RS reaches values larger than 4 K. This is because the result tends to the a priori information, which in this case is *far* from the *true* atmospheric state, i.e. the RS. In region (b), where T can be measured by RL, the difference is reduced to values smaller than 1 K.

When LIME SOAP is run introducing only the MWR TBs, a temperature inversion is resolved close to the ground, which cannot be detected by the lidar (see right panel on figure 5.1). The only-MWR performs better than the only-RL in region (a), reducing the difference to the RS to approximately one fourth of the only-RL case in the lowest 1.2 km. This deviation grows with altitude, taking on larger values (up to $\sim$ 4 K) in region (b) from 5 km above, where the MWR looses sensitivity.

When the combination RL+MWR is performed, the resulting profile is improved with respect to the only-RL and only-MWR retrievals. The RL+MWR case presents the smallest deviation to the RS in regions (a) and (b), with values $\sim$ 1 K up to 7 km. The strongest improvement of the joint retrieval takes place in the lowest 2 km of the atmosphere, because the MWR enhances the information content. Note also the region from 2 to 2.5 km, where the RL+MWR product

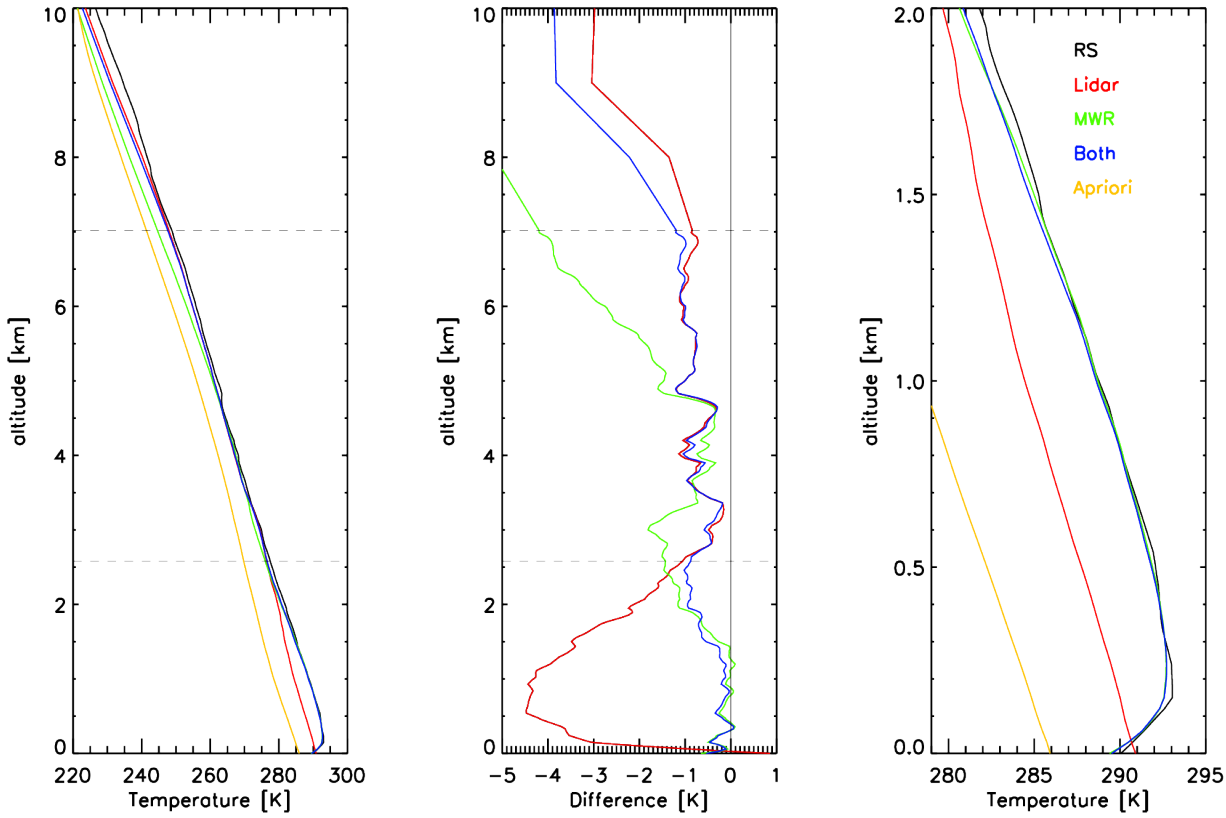

Figure 5.1: Example profile for temperature retrieval on 17th of April 2013, at 23 UTC. From left to right: (a) Complete profiles of temperature for (black) the radiosonde, (red) only-RL information, (green) only MWR, (blue) the combination of MWR and RL. The horizontal dashed grey lines enclose the area where RL data is available. (b) Difference with respect to the radiosonde and (c) zoom to the lower 2km of the atmosphere.

improves ~ 0.5 K with respect to the only-MWR and ~ 1 K with respect to the only-RL. This is due to the vertical information propagation induced by the off-diagonal elements in the covariance matrices S_ϵ and S_a, showing the importance of a robust definition of these matrices, as already demonstrated in chapter 4.

Following equation (4.1), one can calculate the RL+MWR error reduction relative to the only-MWR and only-RL cases. Hence, the total RL+MWR deviation is reduced by ~47% and ~25% with respect to the only-MWR and only-RL profiles, respectively.

The degrees of freedom for this temperature case study are also presented in table 5.1. The independent pieces of information are improved in the lower atmosphere by more than 2 DOF when introducing MWR information, which agrees with the results in figure 5.1. The combination RL+MWR presents the highest information content (>9 DOF), increasing the number of DOF by more than one, with respect to the only-RL case and in ~ 6 with respect to the only-MWR profile. Further details on the DOF are presented in next section for a set of temperature retrievals.

Table 5.1: Degrees of freedom for a temperature retrieval on the 17th of April 2013, at 23 UTC, separated in three atmospheric regions. Lidar data is only present in region (b). The DOF are presented for the cases were only-RL is used, only-MWR and for the combination of the both instruments.

Region	RL	MWR	Joint
a) 0 m to 2.5 km	0.00	2.64	2.57
b) 2.5 km to 7 km	8.15	0.47	6.60
c) 7 km to 10 km	0.00	0.07	0.05
Total	8.15	3.19	9.23

5.1.2 Statistical assessment

The same retrieval scheme is now applied to a longer time series, i.e. all the clear sky situations when BASIL was performing temperature measurements (~300 profiles). As previously mentioned, the dataset for RL temperature is more limited than for mixing ratio due to the complex and costly operation of the T Raman channels. This implies, for example, that comparisons with only 2 collocated RS are possible. Thus for further demonstrating the algorithm performance, this chapter relies on theoretical comparisons (i.e. cumulative DOF (CDOF) or theoretical error), which are statistically evaluated covering a wide variety of atmospheric conditions.

In a similar approach than in section 4.2.2, the lidar temperature profiles are clipped in order to facilitate consistent comparisons and statistics. In contrast to the RL mixing ratio, which has a fixed ZOR, the RL temperature profiles have changing OVF and ZOR. Thus, two clipping altitudes are to be defined: the minimum altitude where RL has enough SNR, i.e. 1.2 km, and the maximum one, i.e. 6 km. These thresholds are chosen to keep around 50% (146 profiles) of the total RL temperature profiles for a significant statistical assessment.

The a posteriori analysis of the T retrieval applied to these profiles is evaluated via the theoretical error covariance matrix S_{op} (eq. 3.5) and the DOF. The square root of the main diagonal elements in S_{op} represents the theoretical error (in K) associated to each altitude of the retrieved x_{op} profile. These theoretical errors are calculated for the 146 retrieved T profiles and averaged, so that an average theoretical error profile is obtained. Figure 5.2 shows the results for the three cases (only-MWR, only-RL and MWR+RL), which are consistent with the results of the case study in figure 5.1, as well as with section 4.2.3 for the AH retrieval.

The HOPE a priori profile (figure 5.2) describes the atmospheric temperature with $\sim 4-5$ K accuracy, presenting higher uncertainty close to the surface, where the largest temperature variations occur. When the MWR TB are used for the temperature retrieval, the resulting profile has an associated theoretical error of ~0.3 K close to the ground, increasing with altitude (i.e. ~2 K at 6 km). The only-RL case presents good accuracy (~ 0.35 K) in the region where RL data is available. Nevertheless, in the other regions, the error estimates grow up to more than 3 K.

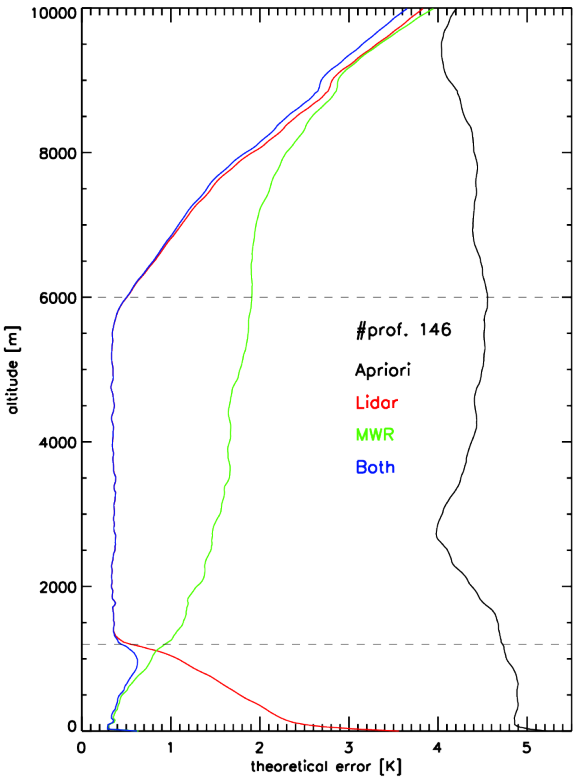

Figure 5.2: Mean theoretical temperature error averaged over 146 temperature cases. The lidar data has been artificially cut for all the profiles and is considered only between 1.2 km and 6 km. In black: a priori uncertainty. Red: only-RL. Green: only MWR. In blue: the MWR+RL. The dashed horizontal lines enclose the region where the lidar data is used.

When the MWR is combined with the RL, the theoretical error improves through the complete profile: above 1.2 km, it is similar to the only-RL case; below this point, the error is reduced to the only-MWR error values.

In order to generalize the results of the case study (table 5.1), the average CDOF for the 146 temperature profiles are presented for the three instrument combinations (figure 5.3). The results are similar to the AH analysis shown previously in figure 4.9. The only-MWR presents the smallest number of DOF, reaching a maximum value slightly larger than 3 at 10 km altitude. For the only-RL retrieval, the CDOF increase linearly in the region where lidar is available. Outside this region, the CDOF remain constant: zero from ground up to 1.2 km, and ~11 from 6 km above. The synergy RL+MWR allows to optimally combine the two sensors information. Special improvement is seen in the lowest region, where the MWR provides a higher information content.

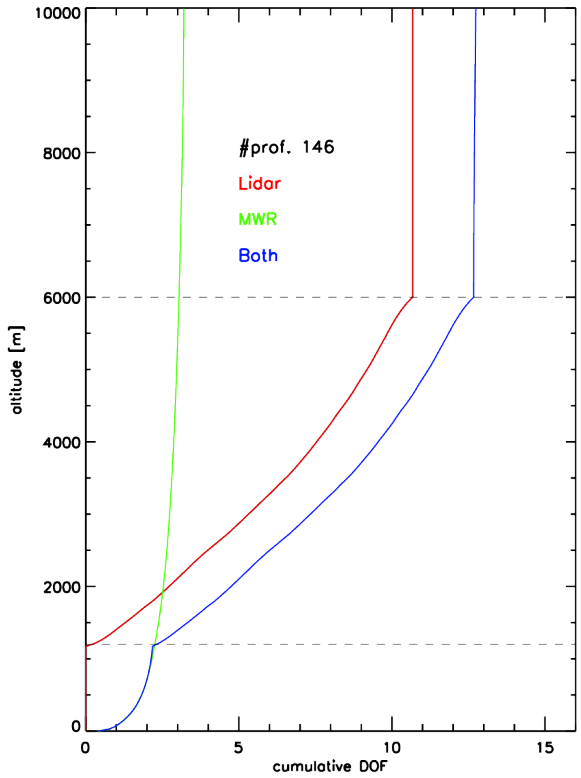

Figure 5.3: Temperature cumulative degrees of freedom for the different instrument combinations: in red, only-RL; in green, only-MWR and in blue, the combination of the two sensors. The resulting profiles are an average over 146 temperature cases. The dashed horizontal grey lines enclose the part of the atmosphere where lidar data has been used.

5.2 Relative humidity

So far the advantages of LIME SOAP applied to AH and T have been presented independently. In this section, LIME SOAP has been implemented to simultaneously retrieve T and AH, taking into account that these two variables are not independent. From them, the RH can be obtained, which is of particular interest to study cloud formation.

In principle, including joint information on AH and T should lead to improvements on the RH estimates. The correlation as a function of the altitude among temperature and humidity was already presented (figure 3.1, first and fourth quadrants) and, in the following, it will be referred as T-Q correlation. The RH profile retrieved using T-Q will be referred as RH-I. It will be compared with RH calculated when no correlation is assumed between T and AH, referred in the following as RH-II.

Because RH does not belong to the atmospheric state vector x, but instead is calculated from the retrieved AH and T, a theoretical a posteriori analysis of the RH retrieval will not be directly possible. Because of that, the retrieval performance is evaluated by comparisons with

independent measurements, i.e. RS profiles.

Case study

The same case study presented for T analysis (see figure 5.1), on 17 of April 2013 at 23 UTC, is used in this section to investigate the RH retrieval. The resulting AH, T and RH-I assuming T-Q correlation are shown in figure 5.4 and compared to the AH, T and RH-II profiles retrieved independently as described in sections 4 and 5.1.

The retrieved T and AH profiles are very similar when assuming T-Q correlation and when retrieved independently (see figure 5.4). Nevertheless, RH-I and RH-II present significant differences. Even if in the lower 4 km the two profiles are similar, above this altitude RH-I presents a $\sim$ 20% smaller deviation with respect to the RS than RH-II. This improvement is induced thanks to the use of T-Q correlation, which constrains the solution.

Because the RL temperature is not always available, it is interesting to investigate weather the RH retrieval is still reasonably good when using all MWR information and only RL mixing ratio profiles. For that, T, AH and RH are calculated assuming T-Q correlation and discarding lidar T (see figure 5.4). The results for all three atmospheric parameters are similar to the case when RL temperature was used, finding only small deviations, i.e. less than 10% for RH, less than 1 K for T and less than 0.5 g/m^3 for AH. This is because, while MWR cannot capture the high AH atmospheric variability, it can already provide a good estimation of the atmospheric temperature, and thus one could disregard the RL temperature in case of limited resources. Retrievals of T, AH and RH without lidar T information will be performed further on in chapter 7.

One can conclude that, for a particular case study, the introduction of correlation information T-Q is beneficial for RH retrieval. The benefit is translated into a reduction of the deviation to the RS, especially in the upper part of the atmosphere, where there is no RL water vapor signal. In addition, the results suggest that the RH retrieval is reasonably good in the absence of RL temperature. Because AH in the atmosphere is highly variable, RL signal is essential to capture this variability, and thus to calculate the RH profile. Nevertheless, T presents a *smoother* variability, which is already satisfactory estimated by the MWR specially in the lowest atmosphere, where this variability is higher and RL is *blind*.

Unfortunately, since the RL temperature data availability is reduced during the campaign, a further investigation with more case studies cannot be carried out at present for the HOPE data, because no *truth* state is known due to the lack of collocated RS.

5.3 Summary

In this chapter, atmospheric temperature profiles are retrieved with LIME SOAP. For such aim, the MWR TBs in the V-band are used (including their angular information) as well as T profiles from RL. An example case study is shown, demonstrating the synergy benefit.

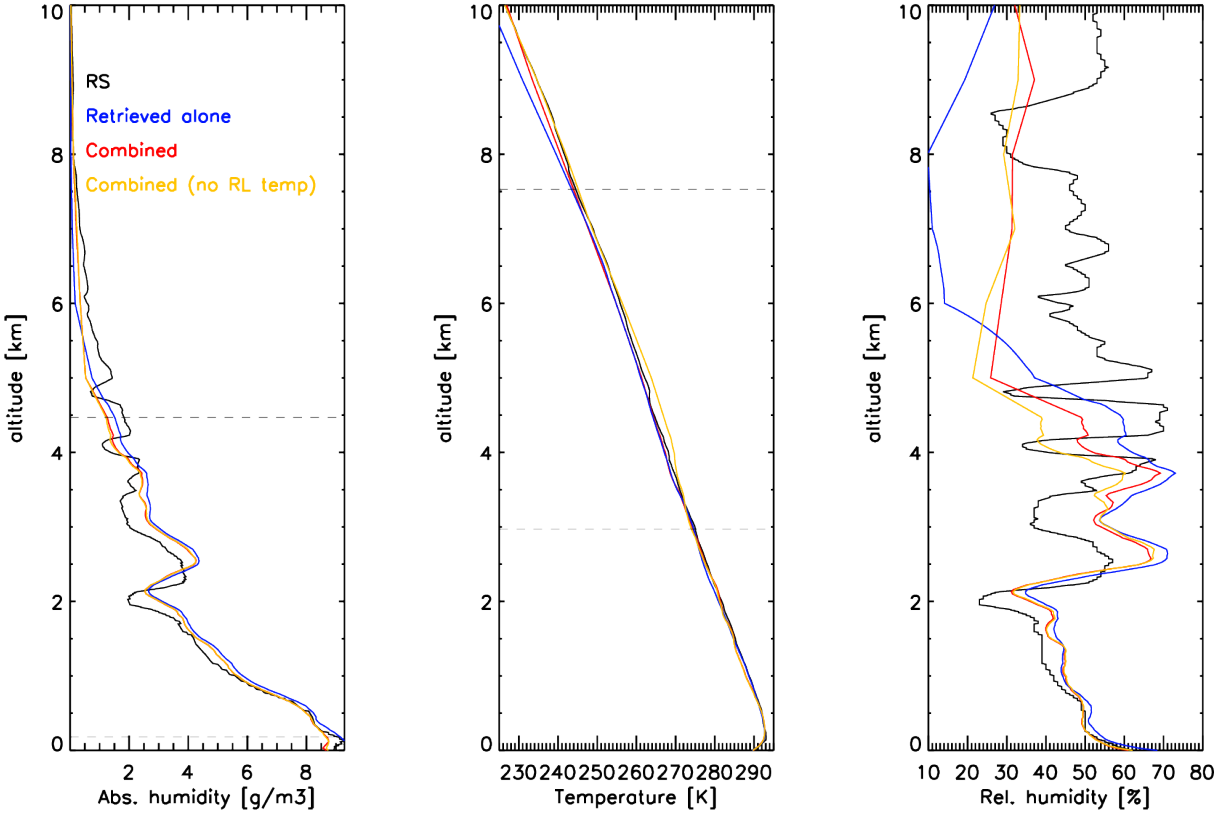

Figure 5.4: Absolute humidity, temperature and relative humidity from RS (black), profiles retrieved separately using MWR+RL (blue), the simultaneous T-Q retrieval using MWR+RL(red) and the simultaneous T-Q retrieval without RL temperature (yellow). Horizontal bars represent the error associated to the resulting profiles. The horizontal grey dashed lines enclose the area where lidar data was available.

While the MWR is more sensitive in the lowest atmosphere where typically T inversions occur, the RL T profiles suffer from OVF problems, i.e. for this specific case study, the RL blind region is 2.5 km. Under these circumstances, the MWR+RL synergy applied to T profiling is very beneficial. In addition to the case study, the T algorithm is also applied to a set of ~150 profiles, which are used to present theoretical comparisons, i.e. degrees of freedom and theoretical error analysis.

In section 5.2, the application of LIME SOAP to the RH calculation is presented for the first time. The AH and T profiles are retrieved assuming T-Q atmospheric correlation, which is demonstrated to improve the RH retrieval for the specific case study. Because the RL T is frequently not available, the RH retrieval is performed neglecting the RL T data. The results show that the latter is not essential and the MWR T information is sufficient.

6

Profiling of the cloudy atmosphere

In previous chapters, the LIME SOAP application to the clear sky scenario has been presented. A step further is to extend the retrieval to cloudy conditions. Because the RL cannot provide information inside or above an optically thick cloud, the MWR+RL synergy benefit is expected to be strongest in cloudy cases.

A case study of a broken single layer cloud will be analyzed in the current chapter. The retrieval of the absolute humidity (AH), temperature (T), relative humidity (RH) and liquid water path (LWP) will be presented and discussed.

6.1 Cloud remote sensing

A case study of a broken single layer liquid water cloud over JOYCE (Jülich observatory for cloud evolution) is chosen to demonstrate the application of LIME SOAP to the cloudy scenario. The day of the analysis is the 4th of May 2013. During this day, clear sky conditions prevailed except for thin liquid water clouds in the morning around 5 UTC and a longer period with liquid water cloud between ~18.7 UTC and 19.8 UTC. The latter is the period under analysis in this chapter. According to the wind lidar[1] at JOYCE, wind speeds were ~8-10 m/s in the boundary layer during the whole day, which is relatively high for typical clear sky conditions.

From the synoptic scale, the day is characterized by a high pressure system with center above the gulf of Biscay. The system brought fair weather to most of central France and northern Germany. From above, satellite images can provide a wide perspective of the general atmospheric situation. Figure 6.1 shows the satellite infrared image of METEOSAT at 19 UTC, when the cloud of interest at JOYCE already existed. West of JOYCE and moving in south-east direction, the image shows a cloud field. This cloud field is related to the frontal system extending from the north of France to Belgium (see figure 6.1), which also generates the cloud under analysis over

[1]The *Stream Line* pulsed Doppler lidar from Halo Photonics, `http://halo-photonics.com`.

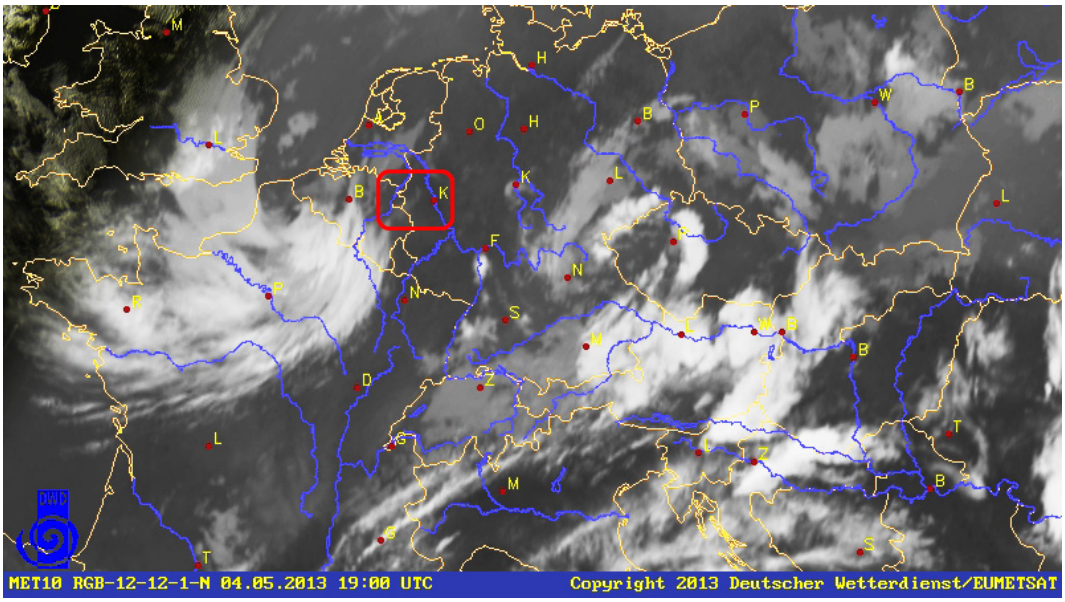

Figure 6.1: METEOSAT infrared image over Europe, 4th of May 2013 at 19:00 UTC. The red square marks the cloud over JOYCE, west of Cologne (K). Source: Deutscher Wetterdienst.

JOYCE. Though weak, some grey shades appear in the area around the observatory. Note that, the whiter the cloud, the colder its temperature and vice versa. Thus, the weak grey shades represent low warm clouds, which are hardly distinguishable from the (warm) surface.

From the ground based perspective, the cloud is observed with a wide variety of sensors available at JOYCE. With the information of these sensors, Cloudnet (section 2.4.5) provides the cloud geometry, i.e. cloud base from the Jenoptik CHM15k Nimbus ceilometer (section 2.4.4), and cloud top from the cloud radar JOYRAD35 (section 2.4.3). In addition, the MWR provides good estimates of integrated values, i.e. the liquid water path (LWP) and the integrated water vapor (IWV) (see section 2.2.2). Moreover, the total sky imager[2] (TSI) provides pictures of the sky periodically (see figure 6.3).

With all this information, one deduces the cloud geometry and the amount of water in it, shown in figure 6.2 for the case under study. When the LWP (calculated with a simple statistic algorithm (Löhnert and Crewell, 2003)) is around zero there are no liquid water droplets whose thermal radiation is detected by the MWR. Around 18.7 UTC the MWR detects an increase of the LWP, which continues increasing until it reaches a maximum of ~40 g/m^2 before decreasing again. The signal shows a gap in the cloud between 18.85 UTC and 19 UTC, when the cloud grows again. The maximum cloud water path is found at ~19.35 UTC, reaching a value of almost 60 g/m^2. After this time, the LWP starts decreasing again until the cloud vanishes at around 19.8 UTC. The cloud top and the cloud base from Cloudnet are also shown in figure 6.2. Note that there are small discontinuities in these values because the radar was performing periodic scans and no zenith observations are available at these points.

[2] http://www.yesinc.com/products/cloud.html

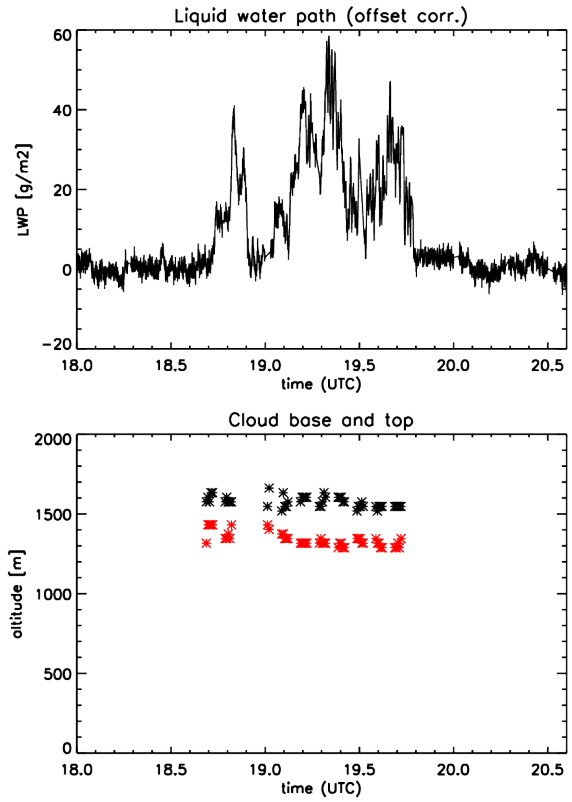

Figure 6.2: Time series of (top) offset corrected liquid water path $[g/m^2]$ from the MWR statistical retrieval and (bottom) cloud base (red) and cloud (top) from the Cloudnet classification, combining radar and ceilometer measurements.

Figure 6.3 shows a sequence of four pictures of the total sky imager. The first, at 18 UTC (figure 6.3a), presents a clear sky situation. The second, at 18.5 UTC (figure 6.3b), shows an early stage of the developing cloud, which is neither detected by the MWR nor by the radar. By the shape, one could think it is a cumulus cloud, but later on it does not have a cumulus shape any more (figure 6.3d). By 19.16 UTC, a stratiform cloud field mostly covered the sky. Vertical velocity from wind lidar indicates that cloud is not related to convection originating from surface.

In order to analyze the cloudy period in more detail, the LIME SOAP is applied to retrieve the LWP, AH, RH and T profiles.

Microwave radiometer and lidar temperature and humidity profiles

To apply the LIME SOAP algorithm, the MWR and RL measurements are required. For the AH retrieval, the MWR TBs in the K-band are used as well as the water vapor mixing ratio (WVMR) profiles from the RL. Figure 6.4a shows the RL WVMR converted into AH, while figure 6.4b presents the AH profiles calculated with a simple statistical retrieval based on a quadratic regression method, i.e. a multi-variate regression scheme based on an extensive radiosonde data set from DeBilt (NL). The figures are presented in order to illustrate the strongest benefits of the

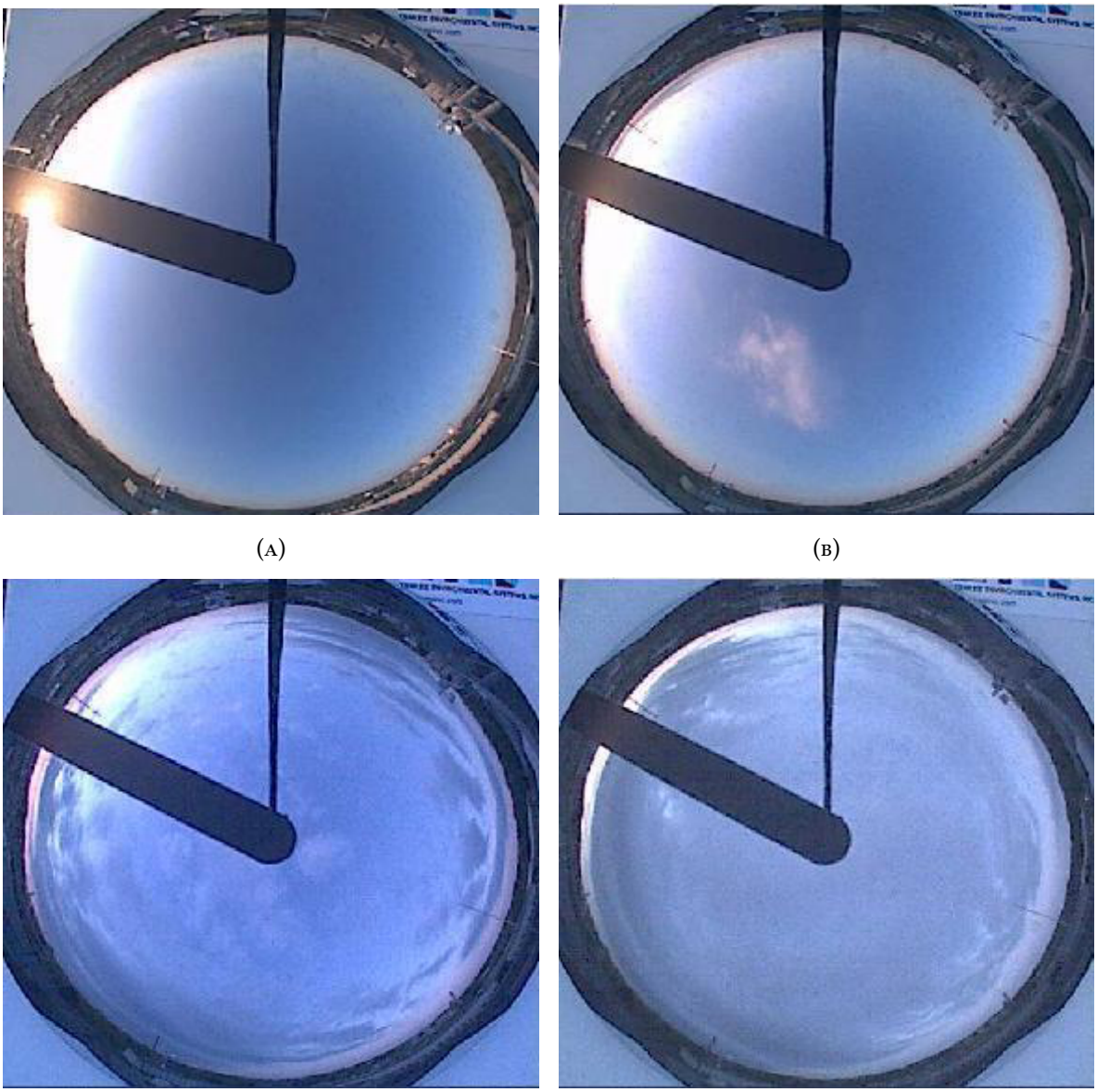

(A) (B)

(C) (D)

Figure 6.3: Total sky imager pictures at (A) 18 (B) 18.5 (C) 19.0 and (D) 19.16 UTC.

combination in the presence of a cloud.

Since the RL is an active instrument, it provides a high vertical resolution (here 30 m is used), but as previously discussed, its signal is attenuated as soon as encountering a cloud (see section 2.3). If the cloud is optically thick, no signal is received from the cloud and above. In addition, the RL zero overlap region (ZOR) does not allow to receive any information from the lowest 180 meters (see section 2.3.2). The signal before the cloud, i.e. until ~18.6 UTC, is strongly affected by the background day time radiation from around 2.5 km above. After the cloudy period, one can nicely see how the maximum lidar range is slowly increasing from ~2.2 km at 19.80 UTC up to ~3 km at 20.5 UTC because the background radiation causing noise is decreasing. Note that,

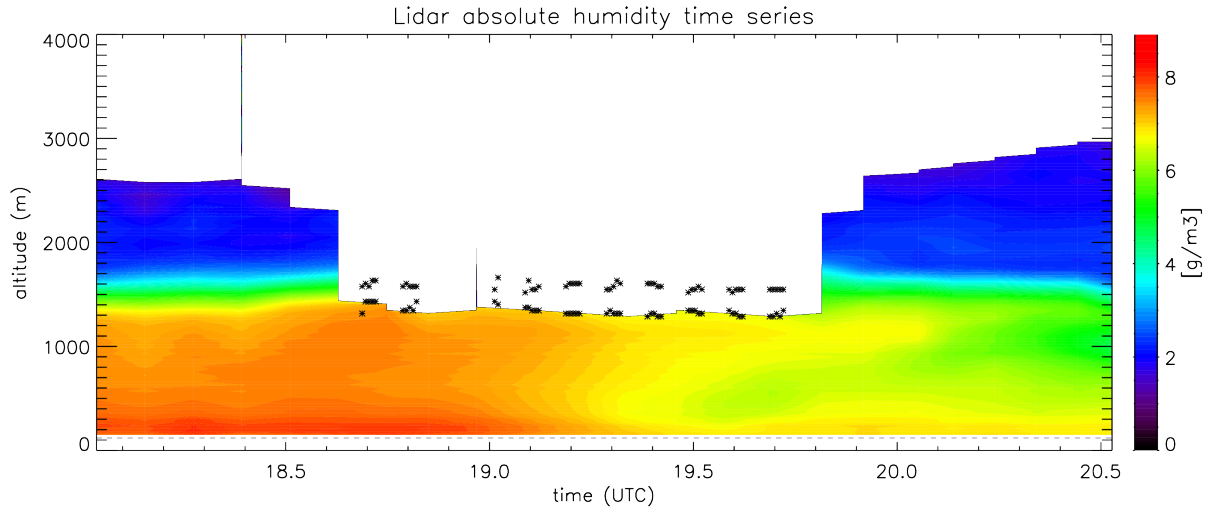

(A)

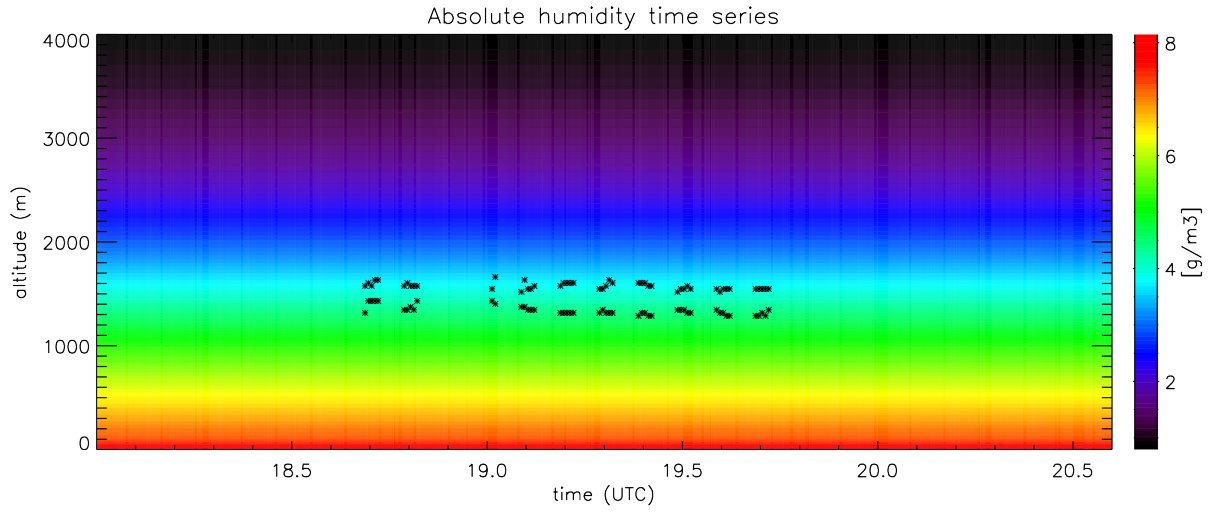

(B)

Figure 6.4: Absolute humidity $[kg/m^3]$ time series (a) from the WVMR of BASIL and (b) calculated from statistical retrieval applied to the MWR K-band frequencies.

following the explanation in section 3.2.2, the RL data whose relative error is larger than 100% is discarded.

In contrast to the RL, the information provided by the MWR is continuous regardless of the presence of a cloud or the background radiation (figure 6.4b). Nevertheless, the vertical resolution of the MWR profiles is extremely poor compared to the RL (see section 2.2.2).

Similar conditions hold for temperature. For the retrieval of T profiles, the RL T profiles and the MWR TBs in the V-band are used. The MWR temperature profile from the statistical retrieval has a coarse resolution (see figure 6.5b and section 2.2.2), similar to the AH profiling. The RL T profiles, same that the WVMR profiles, have a 30 meter resolution (figure 6.5a). Nevertheless, the RL T signal is much more affected by overlapping function (OVF) problems, and in this

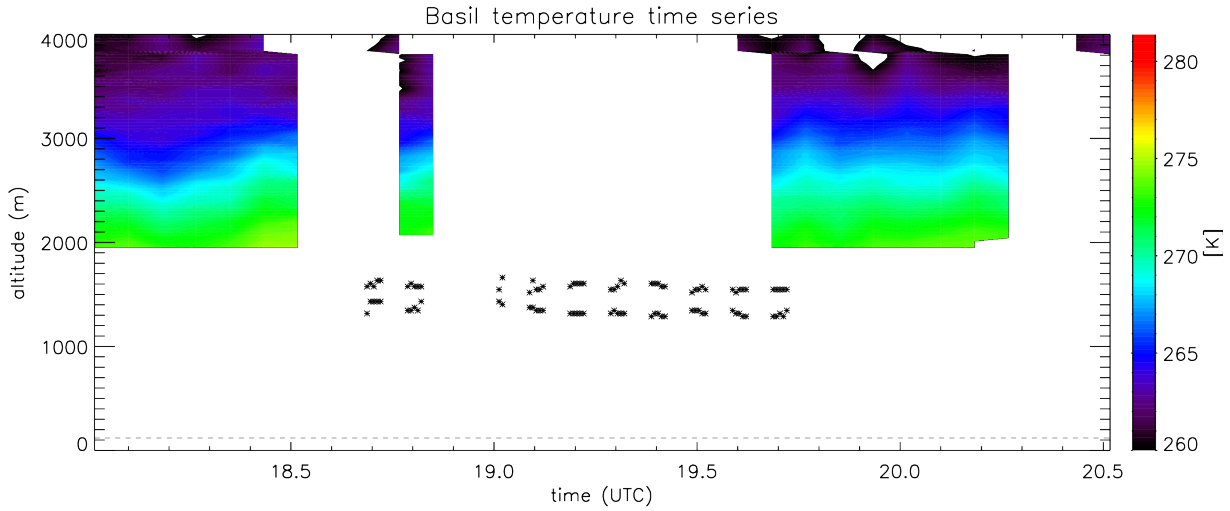

(a)

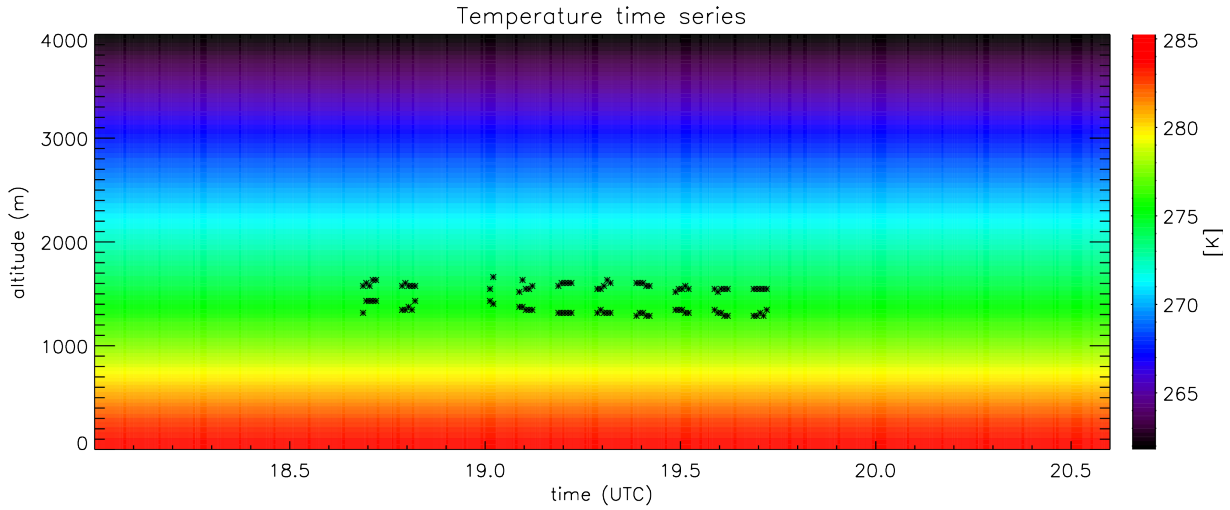

(b)

Figure 6.5: Temperature [K] time series (a) from BASIL and (b) calculated from statistical retrieval applied to the MWR V-band frequencies.

specific case no T information is available in the lowest ~2 km. The useful T range reaches higher altitudes than the WVMR because the rotational Raman backscatter used to sense the T has an intensity 1–2 orders of magnitude larger than the WVMR Raman signals. In addition, the rotational Raman temperature signals, which are 30-50 nm shorter in wavelength, are less affected by the background noise than the WVMR Raman signals (see section 2.3.2).

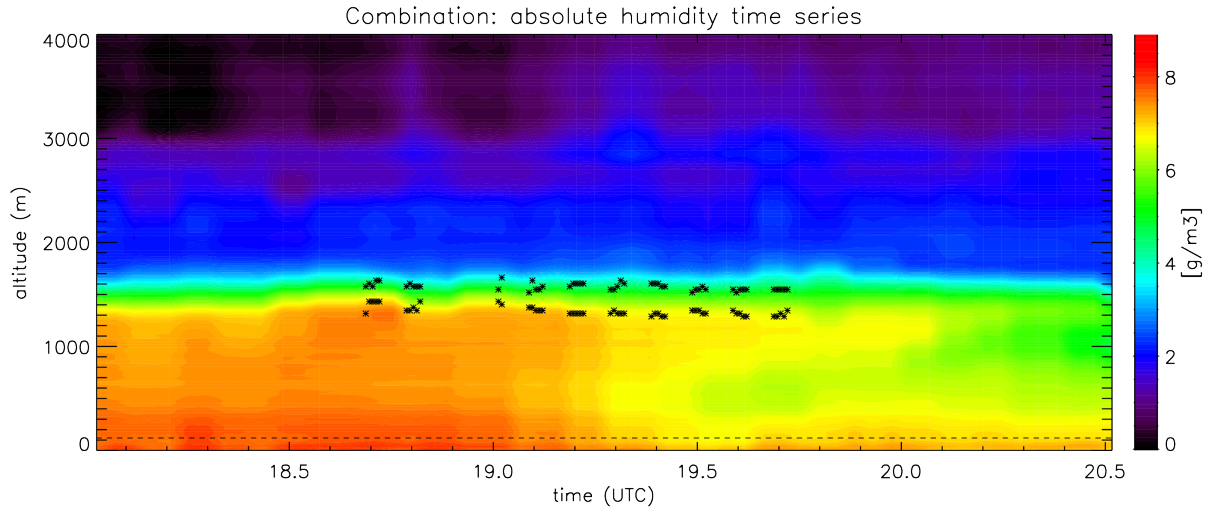

(A)

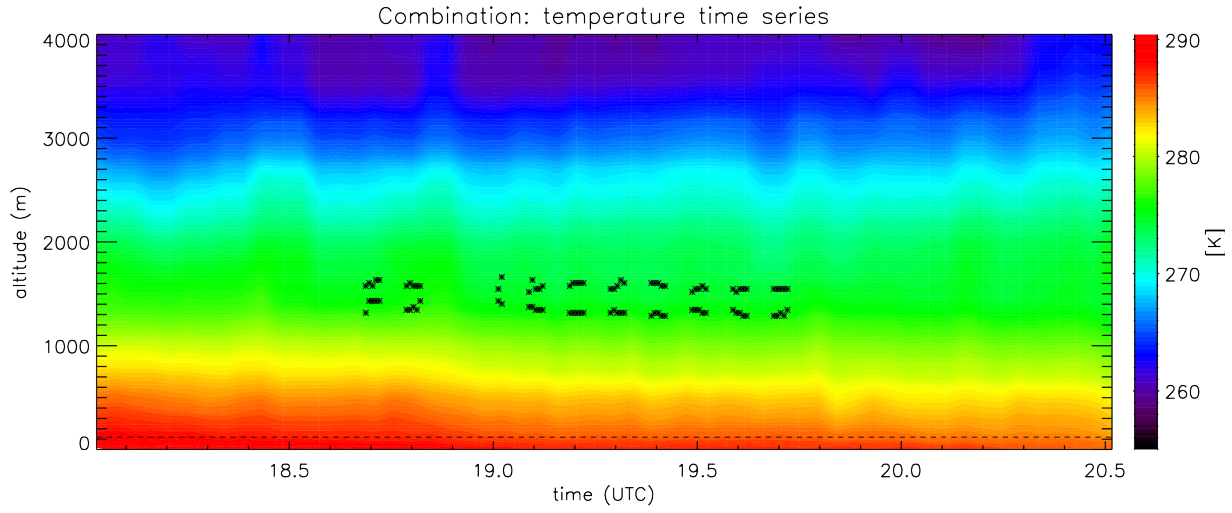

(B)

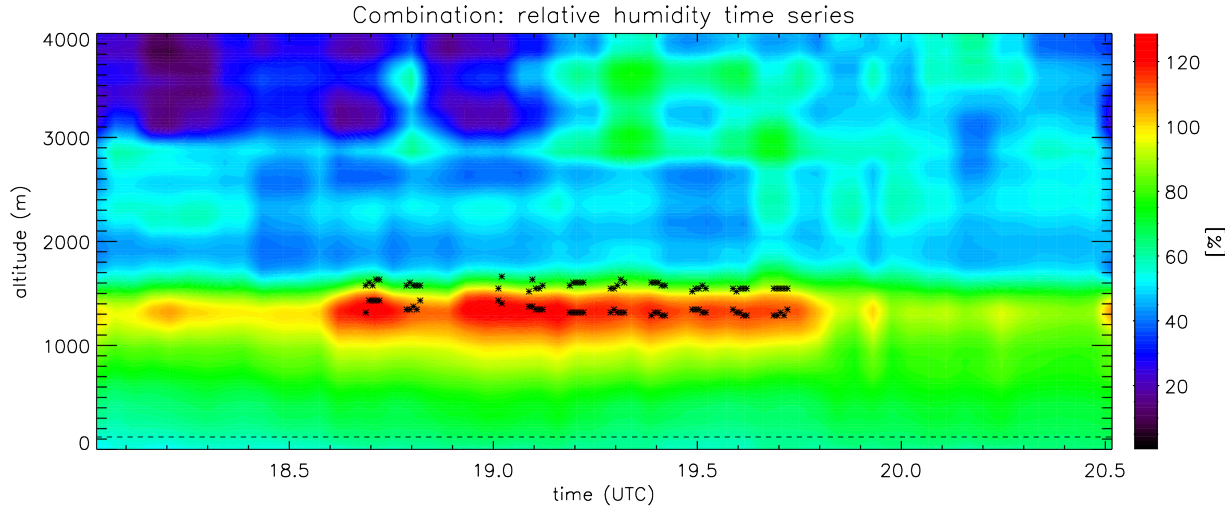

(C)

Figure 6.6: Time series of the retrieved (a) absolute humidity [g/m^3], (b) temperature [K] and (c) relative humidity [%]. The black stars represent the cloud base and top.

6.2 Retrieval in cloudy scenario

During the period under analysis, the MWR directly located at JOYCE, i.e. SUNHAT, did not perform any scans and only its zenith measurements are available. Because MWR elevation scans improve the temperature estimates in the boundary layer (see section 2.2.2), where the RL has a high ZOR for T, the MWR angular information is essential. For this reason, another identical MWR, i.e. HAMHAT, situated ~1 km away from SUNHAT is used to improve the temperature retrieval. This strategy is valid as soon as there is no temperature horizontal variation in a distance of ~1 km from the RL, which in principle is a good approximation. Thus, the angular information from the channels in the V-band from HAMHAT are used together with the SUNHAT zenith observations. Because the V-band frequencies are also sensitive to the water vapor and in order to keep consistent water vapor measurements, not all the angular information from HAMHAT can be taken intro account. Löhnert et al. (2008) showed the influence of a cloud at a certain height on the observed TB. For the case under study, with a cloud at ~1.5 km altitude, an influence larger than 0.1 K in the 54.94 GHz channels at the angles of 90° and 42° is found. These values are thus not taken into account in the retrieval. On the other elevation angles and frequencies, a cloud at 1.5 km altitude has an influence of less than 0.1 K on the measured TB. The rest of the zenith measurements are preferred from SUNHAT because it is collocated right next to the RL.

The MWR forward model needs the cloud top and base as input, which are assumed to be known and are taken from Cloudnet. In addition to the thermodynamic profiles, the LWP will be retrieved within the iterative equation (3.2) as part of the atmospheric state vector x. Within a cloud a RH of 100% can be assumed. Therefore, a saturation constraint has been imposed in the cloud. In addition, the LWC is assumed to be vertically constant between cloud top and cloud base.

The temperature and humidity have been retrieved assuming T-Q correlation (see explanation in section 5.2), which is depicted in the first and fourth quadrants of figure 3.2, and the RH calculated from the retrieved T and AH. The time resolution of the retrieval is the same as the MWR elevation scans, i.e. ~2 minutes. Because the RL has 5 minutes time resolution, the closest RL profile to the MWR scan is used. The MWR zenith measurements, which have 1 second resolution, are averaged over the 2 minutes interval and this mean value is used in the observation vector.

6.2.1 Thermodynamic profiles

The results of LIME SOAP are shown in figure 6.6, where the AH, T and RH time series are presented. Figure 6.6a shows how the higher moisture is confined in the boundary layer, in the lowest ~1.7 km. Below this altitude, the RL is able to capture the water vapor structures, e.g. the highest AH is found close to the surface from 18.6-19 UTC, with values around 8 g/m^3. After

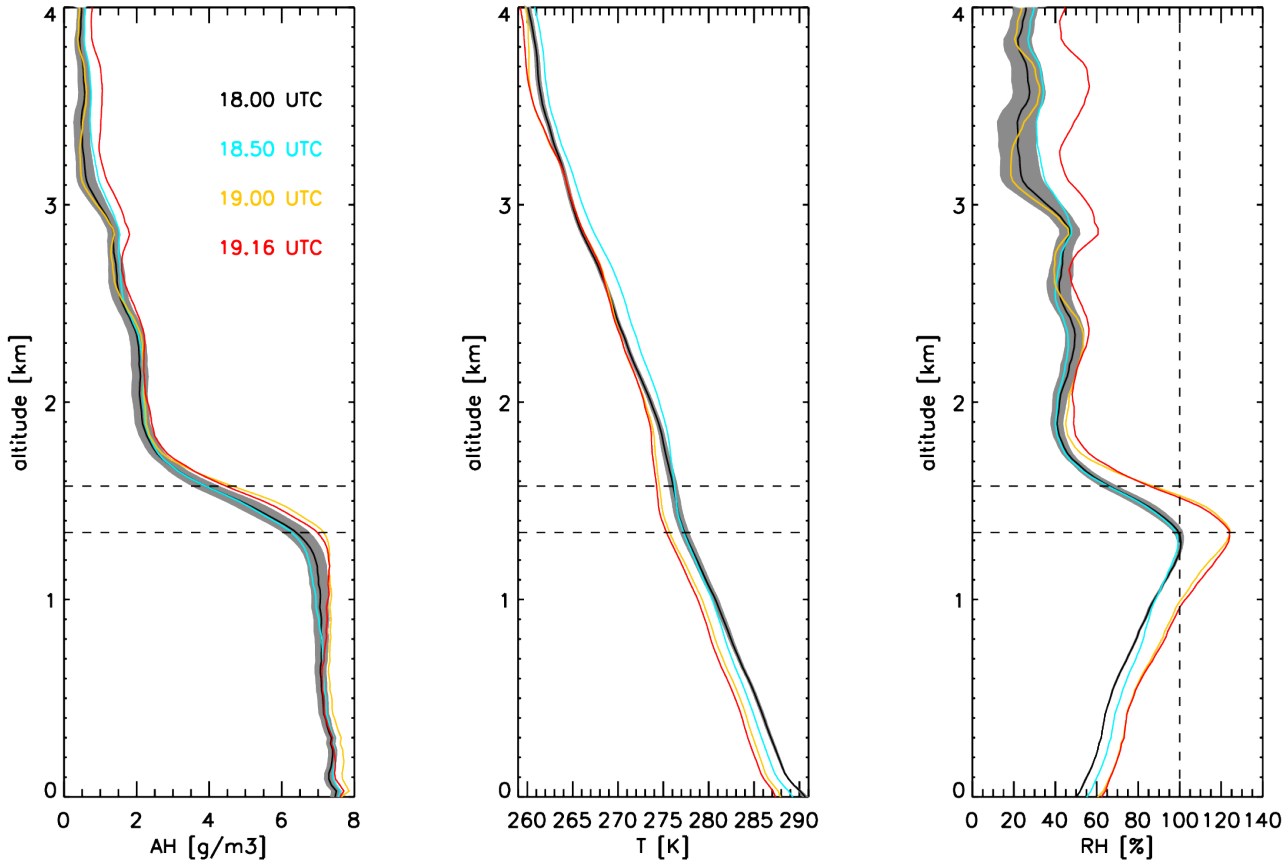

Figure 6.7: From left to right, profiles of AH, T and RH at 18 (black), 18.5 (blue), 19.0 (yellow) and 19.16 UTC (red). The shaded grey area represents the retrieval uncertainty for the profile at 18 UTC. The dashed horizontal lines are the average cloud base and top from 18.7 to 19.7 UTC.

this time, the AH at the surface starts decreasing. At the same time the planetary boundary layer temperature decreases (figure 6.6b) with time due to the presence of a cloud and increasing solar zenith angles. Inside the cloud, AH has values close to 5 g/m^3 and temperature around 275 K. This is translated to a relative humidity which is larger than 100%. The calculated RH (figure 6.6c) shows values of ~60-70 % in the lowest 1.7 km, and some structures in the region from 2 to 4 km. These structures are most probably artifacts. Nevertheless, note that the uncertainty for RH is higher in this region (see figure 6.7), with values around ±10%. The RH is enhanced in the region under the cloud, i.e. from ~750 meters up to the cloud base. Note that in this region, the RH uncertainty is small, i.e. ~5%, because accurate values of WVMR are provided by the RL. The enhancement could be associated with the twilight zone: a belt of forming and evaporating cloud fragments and hydrated aerosols extending from the clouds into the so-called cloud-free zone (Koren et al., 2007).

The retrieved AH, T and RH profiles are shown in figure 6.7 for the same times of the TSI images in figure 6.3, i.e. 18, 18.5, 19 and 19.16 UTC. The figure shows how the two profiles within

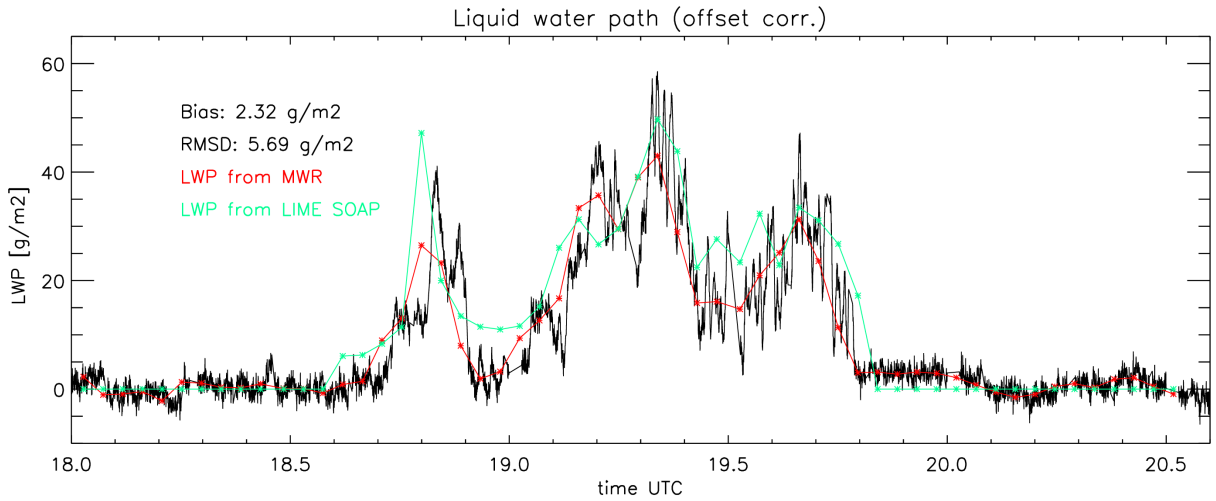

Figure 6.8: LWP time series. In black, the LWP from the MWR statistical retrieval with 1 second resolution. In red, the averaged values of the latter into the retrieval time resolution. The green line is the LWP retrieved within LIME SOAP. The bias and RMSD are calculated between the red and the green lines.

the cloud, i.e. at 19 and 19.16 UTC, present a RH larger than 100% in the cloudy area and below, which is unrealistic. In addition, below the cloud these profiles are 2-3 K colder and the AH is ~1.5 g/m^3 higher than the two clear sky profiles. The uncertainty associated to the products is relatively small, e.g. maximum uncertainty of ~1.6 K for T, of ~0.5 $g/m3$ for AH and of ~10% for RH. This is because a very specific a priori for the day under study was calculated, and thus its associated uncertainty is also small (section 3.2.1.2).

6.2.2 Liquid water path and integrated water vapor

The offset corrected LWP from the statistical MWR retrieval, with 1 second time resolution is shown in figure 6.8. The LIME SOAP LWP values present a bias of 2.32 g/m^2 and a root mean square difference (RMSD) of 5.69 g/m^2 to the LWP statistical retrieval, which lies within the uncertainty of the product, i.e. 20 g/m^2 (see section 2.2.2). Figure 6.8 illustrates the importance of high time resolution measurements for cloudy scenarios, where clearly 5 minutes resolution is too coarse to capture the high temporal variability of LWP.

The IWV has been calculated from the retrieved AH profiles and therefore it serves as consistency check for the retrieval. The result is shown in figure 6.9, together with the IWV from the MWR statistical retrieval and the GPS station (section 2.4.2). The RMSD of the retrieved IWV are 0.51 and 0.28 k/m^2, with respect to the GPS and statistical MWR respectively. The retrieval lies in the GPS uncertainty of 1-2 kg/m^2 (Gendt et al., 2004) and the MWR product of $\sim 0.5 - 1$ kg/m^2 (Steinke et al., 2014a).

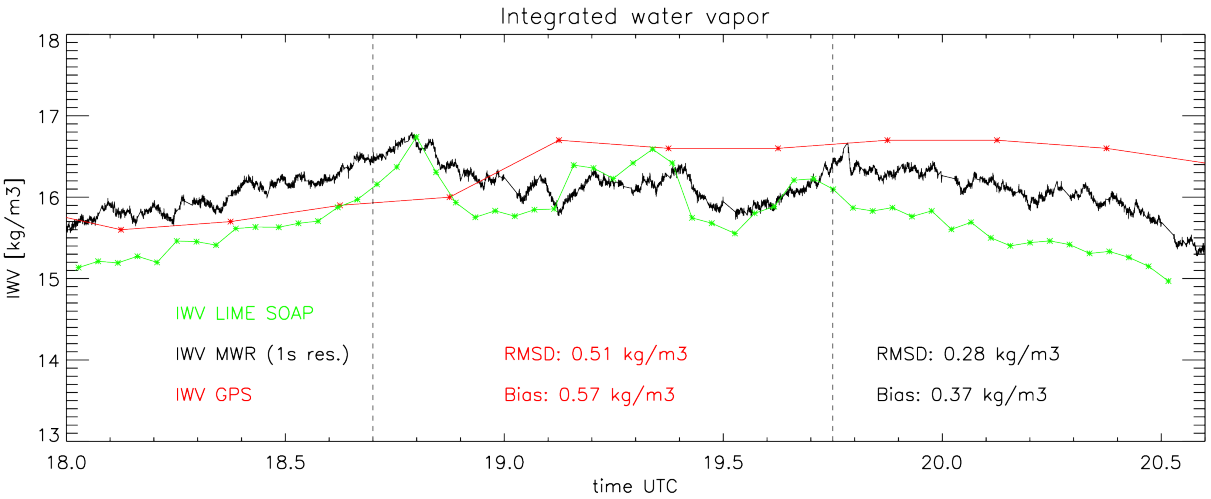

Figure 6.9: Integrated water vapor time series. In black, the IWV from the MWR statistical retrieval, with 1 second time resolution. In red, IWV from GPS, with 15 minutes resolution. In green, the calculated IWV from the AH retrieved in LIME SOAP. Red bias and RMSD are calculated between red and green lines. Black bias and RMSD are calculated between black and green line. The dashed vertical lines separate the clear sky from the cloudy periods.

6.3 Summary

A simple application of LIME SOAP to a cloudy scenario has been presented in this chapter. In addition to thermodynamic profiles, i.e. RH, AH and T, the liquid water path in the cloud has been retrieved as well. The cloud under study is a broken single layer liquid water cloud, with an approximate thickness of 200 m and an average LWP of ~20 g/m^2, though highly variable. For this specific study, the RL data has 5 minutes temporal resolution, which is coarse when investigating cloud formation processes. Using the higher temporal resolution of the MWR data instead represents a strong advantage since the high temporal variability of liquid water can be captured. Here results for 2 minutes retrieval grid have been presented, but the time resolution could be lowered down even up to 1 second. Unfortunately, the evaluation of the retrieval with other independent measurements is not possible. Nevertheless, the calculation of the LIME SOAP IWV shows a good consistency with simultaneous GPS observations, with a 0.51 kg/m^2 RMSD with respect to the IWV from GPS.

The application of LIME SOAP to clouds opens new and interesting research possibilities. Here, a simple case study was shown, but further improvements are possible in the algorithm, e.g. extending it to more complex cloudy situations.

7

Application to airborne data: HALO

Up to now, LIME SOAP has been applied to the ground based perspective: chapter 4 and 5 presented the retrieval of clear sky absolute humidity (AH), temperature (T) and relative humidity (RH) profiles, while chapter 6 retrieved these variables in the presence of a cloud. The current chapter describes the application of LIME SOAP to the airborne scenario for clear sky thermodynamic profiling.

In this new scenario, challenges including the instruments' viewing geometry, difficulties related to the lack of a priori data in the study area and instrument calibration need to be solved. This chapter will start with a short overview of these challenges and how to overcome them (section 7.1). Section 7.2 presents the algorithm applied to AH retrievals. T and RH retrievals will be evaluated in section 7.3 and section 7.4 respectively.

While the AH retrievals are based on the DIAL+MWR combination, the T retrieval uses only MWR measurements since the lidar on HALO, i.e. WALES, provides only water vapor mixing ratio profiles. Because the available MWR data is a very preliminary version, simulated measurements (SM) will be used for HAMP, i.e. the MWR on HALO. This will allow to identify the benefit of the DIAL+MWR synergy isolating possible problems related to the real MWR measurements. In order to demonstrate the applicability of LIME SOAP to real MWR measurements, a case study using re-calibrated MWR TB will be presented in section 7.5.

7.1 The airborne perspective

In chapters 4, 5 and 6, LIME SOAP was applied to ground based instruments. In the ground based scenario, the strongest advantage of the RL+MWR combination was experienced in the lowest atmospheric layers, where the MWR has a higher sensitivity and, due to OVF problems, the RL is *blind* (zero overlap region (ZOR)). Because this region, i.e. the atmospheric boundary layer, experiences the strongest variations in T and Q due to the energy transfer at the surface,

introducing the information from MWR was specially advantageous.

Nevertheless, from the airborne perspective, the lidar ZOR is situated in the upper atmosphere, where the water vapor amount is low. Consequently, the inclusion of the MWR information, in principle, does not lead to a significant improvement in the ZOR, as happened in the ground based case. The strongest improvement is expected to be on the cloudy scenario, when the lidar signal gets attenuated in the presence of trade winds clouds, very common in the study area.

In contrast to the Raman lidar used in the ground based scenario, the DIAL WALES does not provide information on the T profile. Thus, within LIME SOAP, thermodynamic profiles will be retrieved with high vertical resolution, in the absence of lidar temperature, which is in principle not essential (see section 5.2). In the RH retrieval, we benefit not only from the high vertical information provided by the lidar, which allows to accurately capture the water vapor variations, but also from the MWR temperature profiling capability.

As discussed in section 3.2.1.3, the airborne AH is retrieved using its logarithmic value (log(AH)), in order to avoid the retrieval of negative AH values. The HAMP information used for that comes from the 7 channels on the K-band (along the 22 GHz water vapor absorption line) and the 7 frequencies of the G-band (centered at 183.31 GHz). As already shown in Aires et al. (2015), these are the channels most sensitive to water vapor, though with different sensitivities depending on the altitude range (see figure 2.6). The retrieval of T profiles is calculated with the 19 frequencies measured by the HAMP module in the V, W, F and G bands, because all of them are sensitive to T variations (Aires et al., 2015). A summary of the frequency bands was presented in table 2.1. The relative humidity profile will be calculated from the previously retrieved AH and T profiles.

Before applying LIME SOAP, preparatory steps are required, such as the a priori definition, or the preparation of the instrument measurements, explained in the next sections.

7.1.1 A priori

In chapters 4, 5 and 6, the a priori information x_a and S_a was calculated from RS, because during HOPE a large set of RS ($\sim$ 300) was available. Its average and standard deviation (STD) adequately represent the weather variations during the 2 months campaign. In contrast, during the NARVAL experiment, only 34 clear sky dropsondes (DS) are available in the study region. In addition, the data availability over the ocean is typically restricted to satellites, with a couple of overpasses a day. For these reasons, it was initially decided to calculate the a priori from reanalysis data. Figure 3.4 presented the correlation matrix obtained using ERA-INTERIM reanalysis (ERA-I) data (see section 2.4.6), which is frequently referred to as the best model estimate of the atmospheric state (Dee et al., 2011).

When a priori from ERA-I is used, the algorithm convergence presents problems. An example

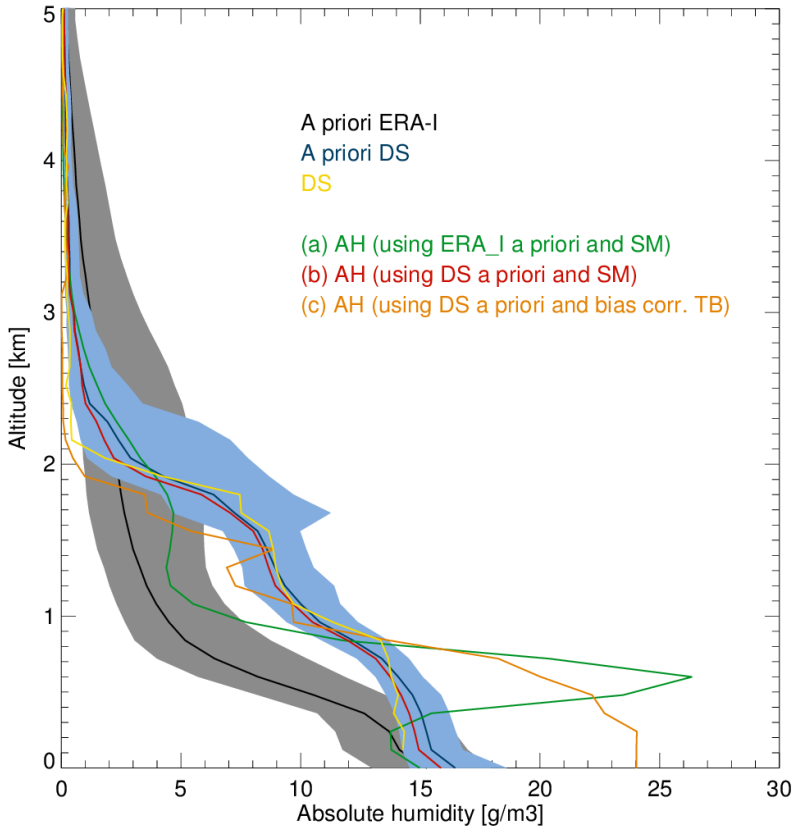

Figure 7.1: Retrieval performance using different a priori informations: the a priori profile calculated from ERA-I data, together with its uncertainty (black); blue represents the a priori calculated from DS. Green, red and orange profiles represent the absolute humidity retrievals for 19th December 2013 at 20 UTC using (a) ERA-I prior and SM, (b) DS prior and SM and (c) DS prior and bias corrected brightness temperatures, respectively. In yellow, the DS on the 5th research flight at 19.9 UTC (see figure 2.3), used as a reference of the *true* atmospheric state.

of this is depicted in figure 7.1, showing the a priori absolute humidity profile x_a, together with its uncertainty and the DS on the 5th research flight at 19.9 UTC (see figure 2.3) used as reference. The algorithm finds convergence [1] and even if the retrieved profile is consistent with the SM, it is not with the *real* atmospheric situation.

The retrieved profile in figure 7.1 is not an isolated example: it represents the general retrieval behavior when using the ERA-I a priori. The explanation for this is that the model a priori does not represent the atmospheric state during the NARVAL campaign. As figure 7.1 shows, the *true* profile is outside the a priori uncertainty. In addition, the atmospheric behavior in the region from 0.5-2 km is not properly captured by the model. This is most probably due to the coarse

[1] Simulated MWR measurements are introduced in LIME SOAP to isolate the a priori problems from others (i.e. bias in the measurements). The SM are calculated from DS data: the forward model (FM) is applied to the dropsonde profile and additional random noise based on the instrument specifications is added to the SM.

vertical and horizontal model resolution.

Therefore another approach for the a priori calculation was chosen: to use the dropsondes, even if the amount is limited. Figure 3.5 in chapter 3 shows the new correlation matrix calculated from the 34 clear sky DS released in the region from 10-23 degrees latitude. The atmospheric description provided by these 34 clear sky profiles, properly represents the atmospheric situation during the campaign. Using the DS a priori, the retrieved absolute humidity profile better fits to the reference, as can be seen in figure 7.1. For these reasons, the DS a priori will be used in the following.

7.1.2 MWR measurement bias

Another difficulty found through the definition of the algorithm are instability issues with the MWR measurements. A very preliminary version of the MWR data is used in this study, so a bias correction must be performed. A first attempt to estimate a bias correction for the MWR channels is performed by comparing the instrument measurements with clear sky dropsondes. The DS profile, which represents the *real* atmospheric state, is introduced in the FM. As a result, one obtains the TBs that the instrument would measure. These serve as reference and are compared with the real MWR TB.

The biases on the measurements depend on the instrument calibration, which is performed before each flight in NARVAL (see section 2.2.3). Because of that, a bias and STD are calculated for each flight. Even if the calculated biases are large (see figure 1 and 2 in Appendix), they would not represent a problem as soon as they were constant during the whole flight. In this case, one could simply correct the MWR measurements by subtracting the value of the bias. Nevertheless, the standard deviations present high values as well (up to $\sim 6K$), which indicate that the bias is not constant during each flight. The reason for the varying biases could be found in an instability of the instrument itself, as well as in the way the reference TBs have been calculated. For example, a mismatch between the atmospheric column sampled by the DS and the radiometer and/or errors in the calculation of the emitted surface radiation. The latter can be due to uncertainties in the sea surface temperature or the emissivity of the ocean.

Still, one could try to correct the MWR measurements with the calculated bias. An example of this is presented in figure 7.1. The retrieved profile belongs to the 5th research flight. Note that, for the absolute humidity retrieval, only the K and G bands have been used. The result shows that, as a compensation for the water vapor underestimation above $\sim$ 2 km, an increase of the humidity in the layers close to the ground is induced. For example, at the surface a value of $\sim$ 24 g/m^3 is retrieved, while the reference presents values of $\sim$ 16 g/m^3. This example shows again the general behavior for the bias corrected MWR measurements during all flights, except for the third research flight. This can be explained because said flight presents the smallest standard deviations in all frequency bands (see figures 1 and 2 in Appendix), which indicates stability in

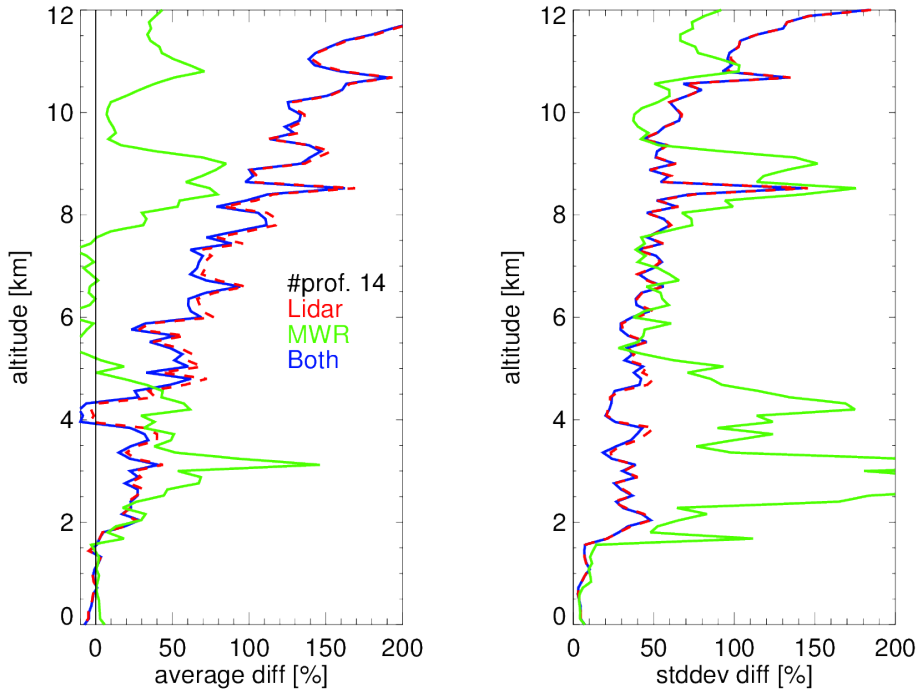

Figure 7.2: Relative difference average (left) and standard deviation (right) in percentage [%], for the retrieval using only lidar (red), only MWR (green) and the combination of the two instruments (blue). The difference is calculated with respect to the DS and averaged over 14 profiles.

the measurements. Because of that, the research flight number 3 will be used in section 7.5 to show a short time series retrieval using bias-corrected measurements.

Further investigation on the MWR bias correction must be performed before using *real* measurements. However, this topic is out of the scope of the thesis and the analysis of the measurements is performed in studies by others. Because the aim of this chapter is to investigate the benefits of LIME SOAP from the airborne perspective, simulated measurements will be used in the following to illustrate the algorithm performance. Note that DIAL real measurements will be considered since they present a good quality when compared to RS profiles.

7.2 Absolute humidity retrieval

7.2.1 Comparison to DS

The AH retrieval is applied in all the cases during NARVAL-South with a collocated clear-sky DS, i.e. a total of 15. Because the behavior of the algorithm for a single profile was presented in detail in previous chapters, the results will be focused now on studying an ensemble of profiles.

The difference between the retrieved profile and the reference (the DS) is calculated for each case and an average difference for 14 cases (in one case convergence was not achieved) is presented

in 7.2 for the three instrument combinations. When dealing with AH, showing the difference relative to the amount of water vapor at each altitude is preferred due to the inhomogeneous water vapor distribution: the differences in regions with low water vapor (upper layers) are better represented when normalized to the AH value of the reference.

The result in figure 7.2 suggests that MWR can perform best in the region above ~ 5 km, where the instrument has higher sensitivity. For example, at an altitude of 10 km, the average relative difference is reduced from 120% for the only-DIAL and MWR+DIAL cases, to the 10% for the only-MWR case. Nevertheless, from ground to ~ 5 km altitude, the MWR presents a larger deviation to the DSs, with a specially large standard deviation: when lidar is taken into account, the STD presents values smaller than 50%, while for only-MWR, it adopts values larger than 200% relative difference.

The results must be carefully interpreted, because MWR simulated measurements, which are calculated from the DS, are used. Furthermore, the DS may present a dry bias when measuring low temperatures, as already studied by Miloshevich et al. (2001). In addition, the dropsonde RH measurements have an error of 1-2%, as specified by the manufacturer (see section 2.4.1). These numbers, when translated to the relative difference for absolute humidity, represent an uncertainty of ~50-100% in the region from 6 to 8 km, and ~30-60% from 8 to 12 km.

7.2.2 Information content

Following the same approach than previous chapters, an *a posteriori* analysis of the retrieval is performed. Here, the information content is assessed presenting the cumulative degrees of freedom (CDOF) and the theoretical error as a function of the altitude, for the three cases: only-MWR, only-DIAL and MWR+DIAL.

The maximum average number of DOF for the only-MWR case is ~ 3, when using 14 channels (figure 7.3a). On the other hand, the only-DIAL retrieval provides up to ~ 28.5 DOF per profile on average. This result is similar to the outcome presented previously for the ground based scenario in chapters 4 and 5.

Nevertheless, while in the ground based case the combination MWR+RL improved the amount of DOF with respect to the only-lidar case, here there is not such improvement. This is due to the fact that the lidar profile typically reaches the ground, and it is not affected by the background noise, as happens to the ground based Raman lidar systems. It implies that the lidar is able to provide already *complete* information on the water vapor profile and, in principle, the MWR only adds redundant information.

The same result is highlighted when one analyses the theoretical error average profiles. Figure 7.3b shows that the only-DIAL theoretical error remains almost the same when the MWR is added. Note that this plot is presented as the logarithm of the absolute humidity because the retrieved variable is the log(AH) and thus, the a posteriori error has the same units.

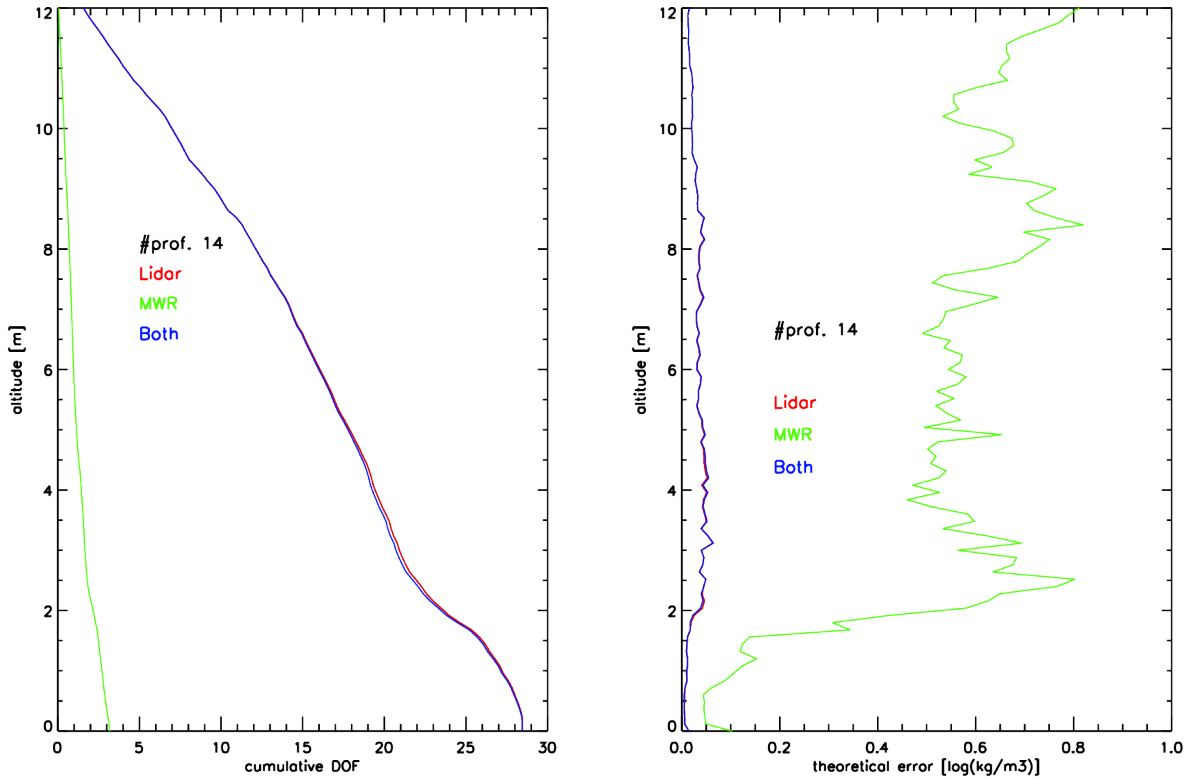

(A) Cumulative degrees of freedom

(B) Theoretical error

Figure 7.3: Information content analysis for absolute humidity retrieval. Average over 14 profiles. Left represents the cumulative degrees of freedom and right, the theoretical error (logarithmic scale), both as a function of the altitude. In green the only-MWR case is presented; in red, the only-DIAL case and in blue, the combination MWR+DIAL. For MWR, simulated measurements are used.

7.3 Temperature retrieval

7.3.1 Comparison to DS

Since the lidar does not provide any information on the temperature profile, the T retrieval is performed using only the MWR frequencies. Similar to section 7.2, the algorithm is applied when a collocated clear sky DS is found, using SM. The difference between the retrieved temperature and the DS T profile is calculated for 15 cases and averaged. Figure 7.4 shows these results.

The retrieval shows a satisfactory behavior. The average deviation to the DS shows always values between ~ -1 and ~ 3 K, being positive above 2 km altitude, and negative below. This change of sign in the average difference suggests that the inversion of the boundary layer is not well captured, which is due to the limited MWR vertical resolution.

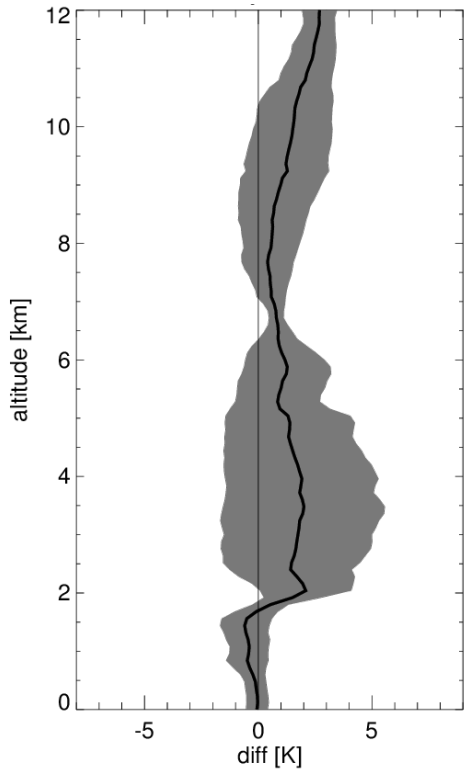

Figure 7.4: Averaged difference and standard deviation [K] for the temperature retrieval using MWR simulated measurements. The difference is calculated with respect to the DS and averaged over 15 profiles.

7.3.2 Information content

The assessment of the information content is performed, same as in section 7.2.2, via the CDOF and the a posteriori error. Figure 7.5a presents the average CDOF, showing how the information content does not increase linearly from the aircraft to the sea. There is a stronger contribution in the layers around 1-2 km. This is also reflected in the reduction of retrieval uncertainty in the area below 2 km, which can be seen both in figure 7.4 and figure 7.5b.

Figure 7.5b shows the average theoretical error for 15 temperature profiles. It adopts values around 1 K, and it is only below $\sim$ 2 km that its value is reduced to less than 0.5 K. The standard deviation estimated in figure 7.4 presents similar values, except for the region from 2-7 km, where the standard deviation is higher than the theoretical error (more than a factor of two).

7.4 Relative humidity retrieval

The relative humidity is calculated from the independent temperature and absolute humidity retrievals. Same than in section 5.2, and because the RH is not the output value of LIME SOAP, an a posteriori evaluation of the RH retrieval is not possible.

A comparison to the DS is performed, similarly to the previous sections. In total, among the

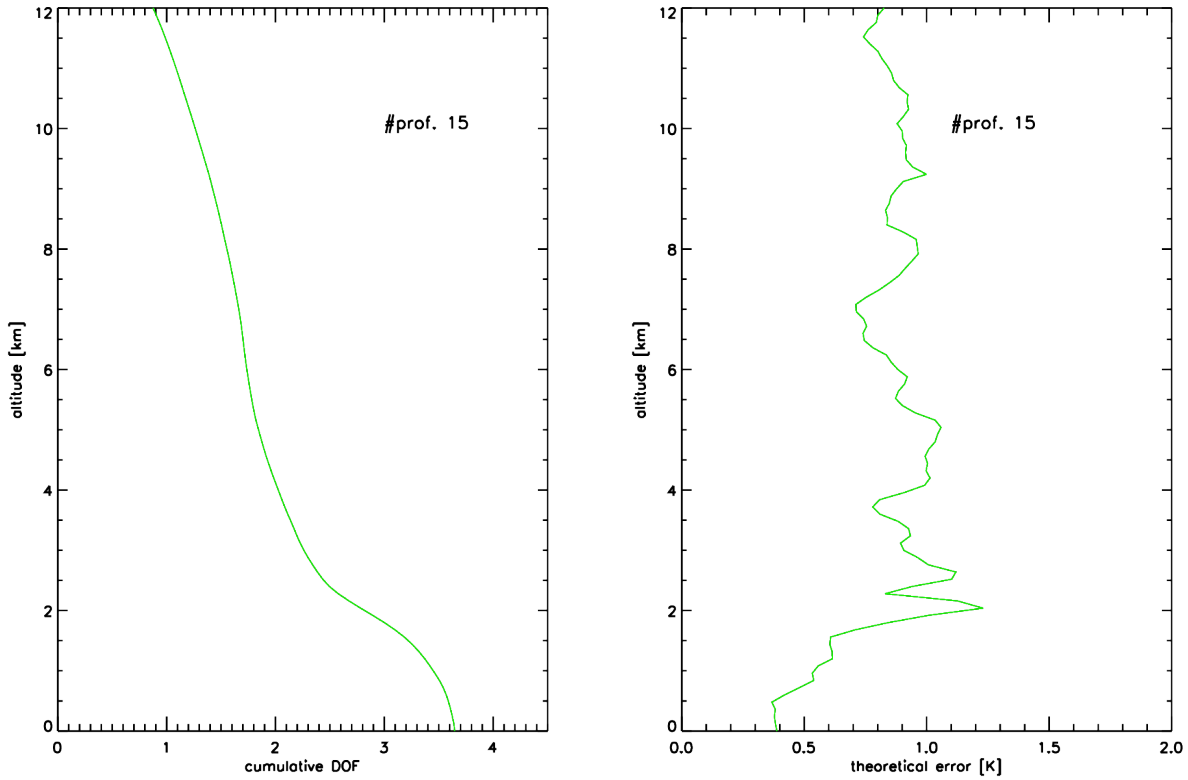

(A) Cumulative degrees of freedom

(B) Theoretical error

Figure 7.5: Information content analysis for temperature retrieval. Average over 15 profiles. Left represents the cumulative degrees of freedom and right, the theoretical error, both as a function of the altitude. Temperature is retrieved using only MWR information.

15 clear sky collocated DS, 12 simultaneous AH and T retrievals are found. The results presented in figure 7.6 agree with the conclusions discussed in sections 7.2 and 7.3. The only-MWR RH retrieval, presents low deviations (< 5%) to the DS from 2.5 km above. The MWR+DIAL retrieval presents a larger deviation above 9 km altitude (up to ~ 30%). Nevertheless, and similarly to results shown in figure 7.2, the only-MWR retrieval shows larger STD from ground up to 5 km. Due to the same reasons explained in section 7.2.1, these results must be interpreted carefully.

Due to the use of SM, the results presented in these sections provide and upper limit of what can be expected from the combination of aircraft-based lidar and MWR. Further work related to the MWR bias correction needs to be performed before applying the algorithm to the full NARVAL campaign.

7.5 Time series

As already mentioned in section 7.1.2, the MWR module presents its most stable measurements during research flight 3 (see figure 3.8). Because of that, an application of the algorithm to real

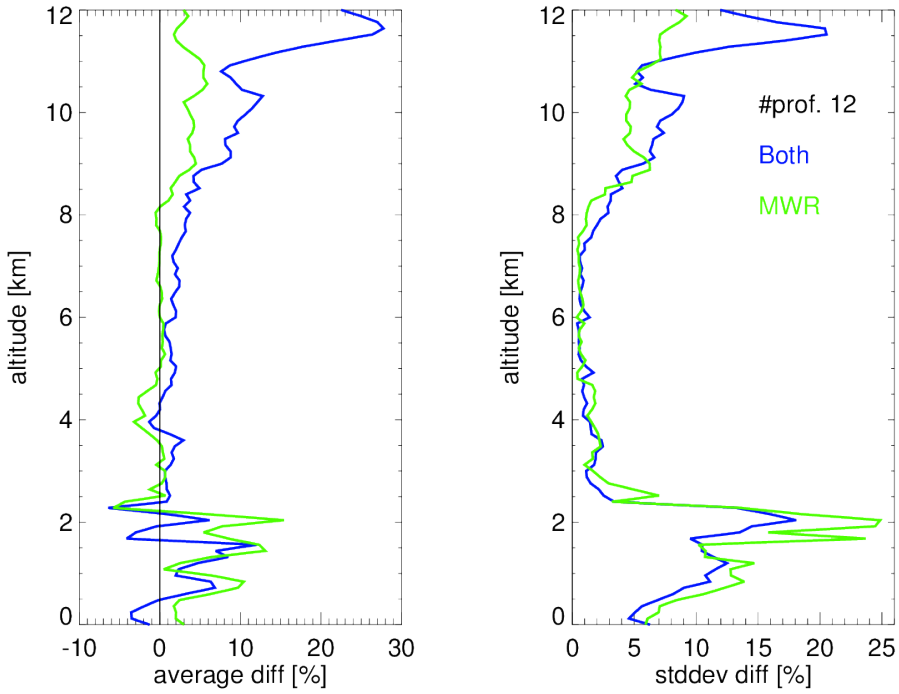

Figure 7.6: Averaged difference (left) and standard deviation (right) in percentage [%], for the RH retrieval using only MWR (green) and the combination of the two instruments (blue). The difference is calculated with respect to the DS and averaged over 12 profiles.

measurements is possible. The MWR brightness temperatures have been corrected using the biases in figure 1 in Appendix. A short clear sky time series of ~ 4.2 minutes is presented in figure 7.7. If HALO is flying at an average speed of ~ 200 m/s, this time series corresponds in space approximately to 45 km. The figure nicely shows the absolute humidity variations in the atmosphere (captured by the DIAL), which find correspondence in the RH. The temperature time series remains stable in this short time interval, though small variations can be seen.

The time interval has been chosen such that there was a clear sky DS, at 17.63 UTC (see figure 2.3). This DS can be used as a reference to compare the real-measurement retrieval results. Figure 7.8 presents the coincident AH, T and RH retrievals together with the DS profiles. The agreement is good for the three retrievals, specially for the AH profiles. Nevertheless, the T retrieval presents a deviation to the DS of around 4 K from 7 km above, which is most probably due to the MWR bias instability. Because of the limited MWR vertical resolution, the retrieved profile is not able to capture the temperature inversion at ~ 1.7 km, which leads to a discrepancy between DS and the RH retrieval of about 10-20 % below ~ 1.7 km.

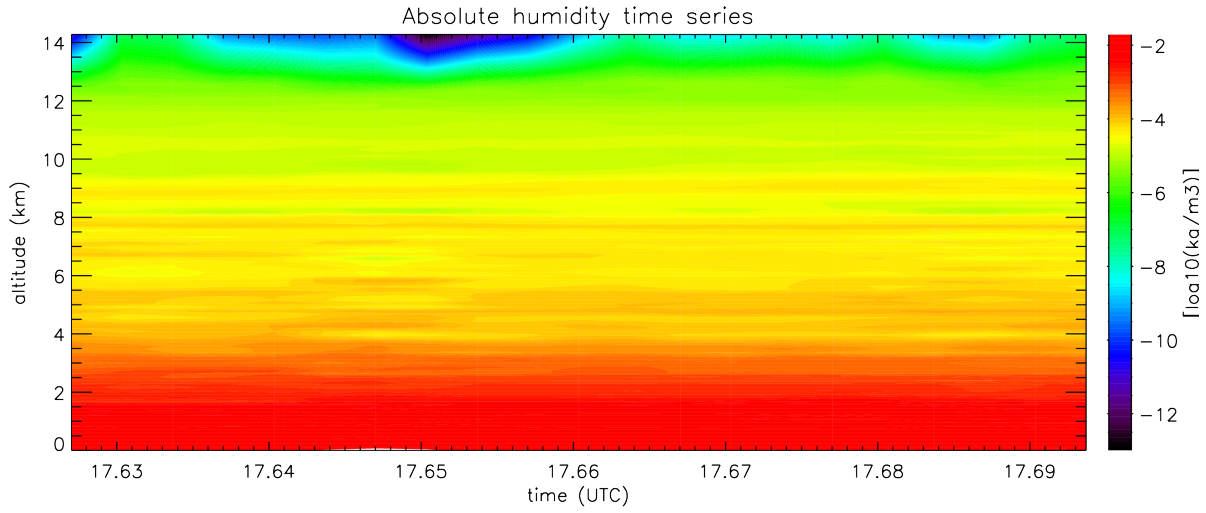

(A)

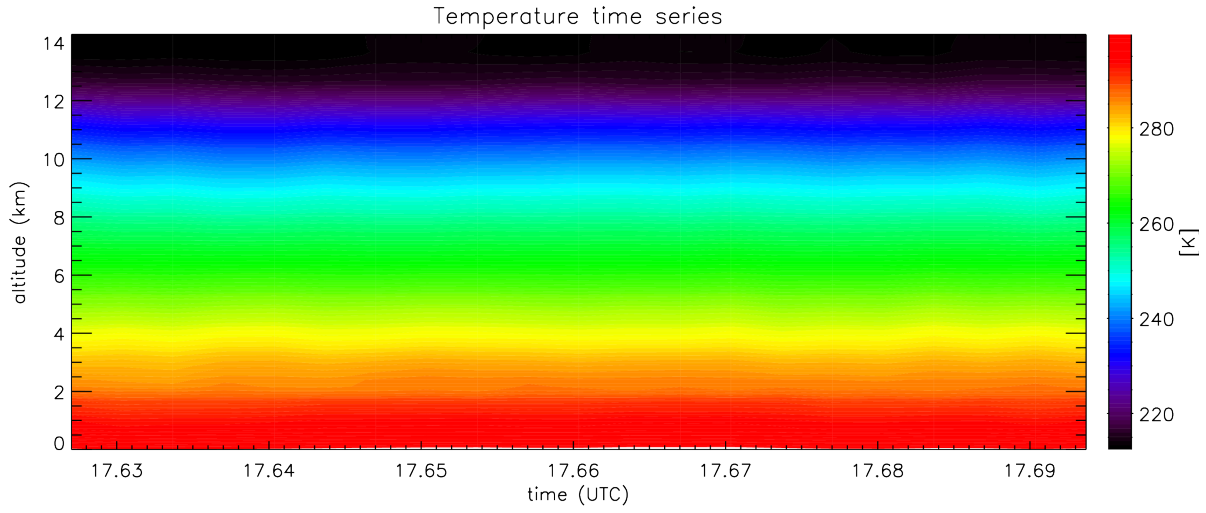

(B)

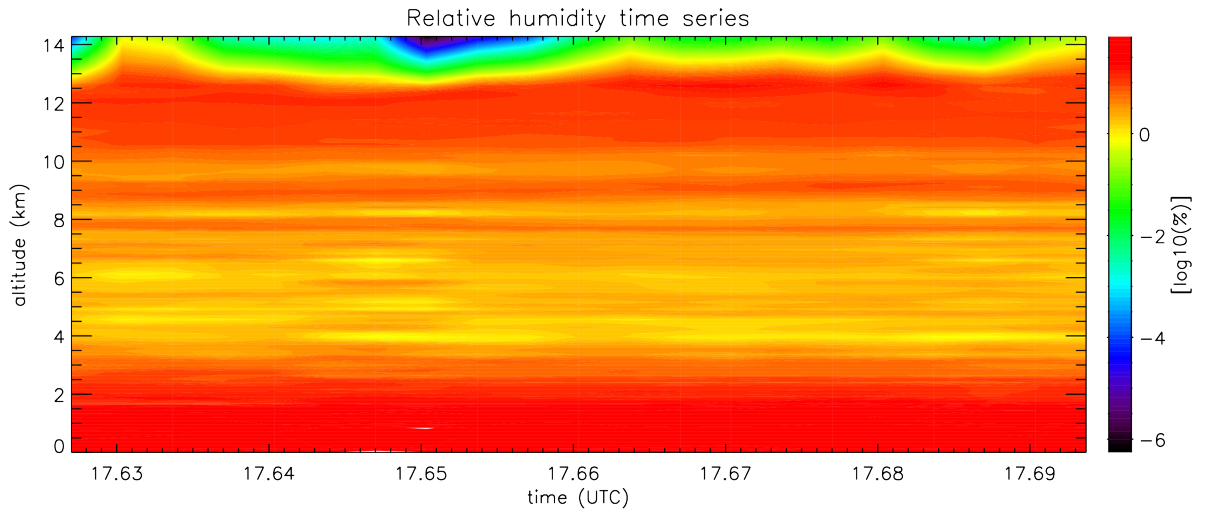

(C)

Figure 7.7: Time series of (a) absolute humidity [$log_{10}(kg/m^3)$], (b) temperature [K] and (c) relative humidity [$log_{10}(\%)$]. Logarithmic scale is used for humidity because it allows to better appreciate the water vapor variability than the linear scale.

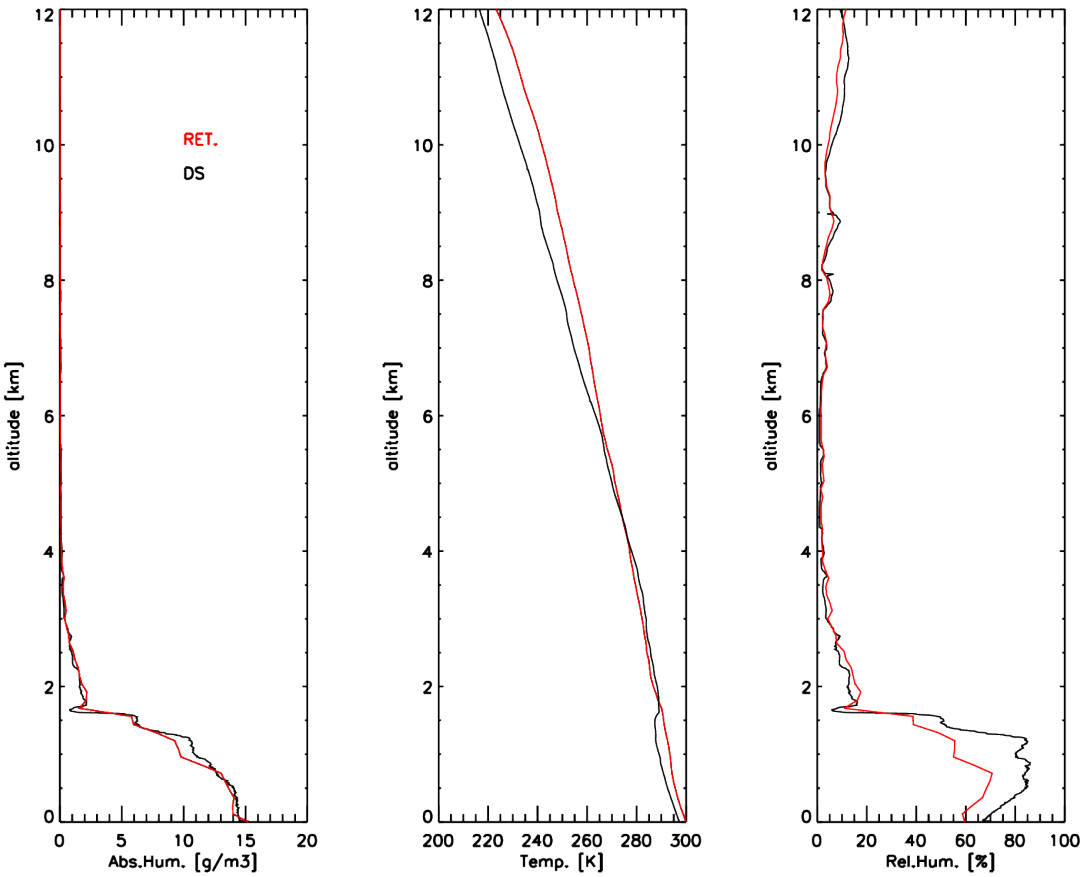

Figure 7.8: From left to right: retrieval of AH, T and RH for the DIAL+MWR combination (in red). In black, the collocated DS launched at 17.63 UTC is presented.

7.6 Summary

In the current chapter, LIME SOAP has been applied to the airborne scenario of HALO. The data used in this study for the MWR module, i.e. HAMP, is a very preliminary version and some bias are detected. Because the aim of this study is to demonstrate the algorithm performance, and in order to isolate possible problems related to biases in the measurements, synthetic measurements are used for the MWR.

The MWR+lidar synergy is presented from the airborne viewpoint for AH, T and RH profiles. Comparisons with independent measurements, i.e. dropsondes, and information content analysis of the retrieved profiles, i.e. degrees of freedom and theoretical error, serve for evaluating the synergy benefits.

Only in section 7.5 real bias corrected MWR measurements are used, applied to a short ~4.2 minutes time series of AH, T and RH profiles. Further studies will be based on implementing improvements in the algorithm, e.g. a better estimation of the sea surface temperature, and satellite product evaluation.

8

Conclusions

Atmospheric temperature and humidity are essential variables for the description of any meteorological process. Highly resolved, accurate and continuous measurements of these parameters are required for a deeper understanding of many atmospheric phenomena. However, nowadays there is no single instrument, which can provide all of the following requirements simultaneously: complete vertical coverage, high vertical and temporal resolution of the atmospheric profiles and satisfactory performance under all weather conditions. That is the reason why the synergy of different sensors has become more and more into focus in the last years.

In this thesis, a new, flexible and robust method to combine lidar profiles and multi-frequency brightness temperatures from microwave radiometer has been presented: the LIME SOAP (Lidar and Microwave Synergetic Optimal Atmospheric Profiler). The joint algorithm that combines the two sensors is based on an Optimal Estimation Method and is applied to the retrieval of thermodynamic profiles, i.e. absolute humidity (AH), temperature (T) and relative humidity (RH). For that, the data collected during HOPE, a two-months campaign deployed at Jülich, Germany, is used. In addition to this ground based application, the retrieval algorithm is extended to the airborne sensors on board of HALO, flying during the NARVAL campaign, in December 2013 over the tropical and subtropical Atlantic ocean. During both field experiments a wide variety of measurements have been collected, and used in this thesis to evaluate the algorithm.

To implement LIME SOAP, a robust definition of an a priori atmospheric information is required. This a priori serves to constrain the infinite number of solutions in the atmospheric state space to a physically meaningful subset. In this study, the a priori is defined using radiosonde data, numerical weather prediction model re-analysis or Cloudnet (Illingworth et al., 2007) climatology, depending on the scenario and data availability in the area of study. It is demonstrated that the resulting retrieval is degraded by the a priori definition if the same does not offer a proper description of the atmospheric state. In addition, the a priori covariance matrix S_a plays

an important role on the vertical distribution of the information because its off-diagonal elements establish a relation within the different atmospheric layers.

The instrument measurements, i.e. MWR TB and lidar profiles of water vapor mixing ratio (WVMR) and/or T, are introduced in LIME SOAP, together with their measurement uncertainty description. This uncertainty must be carefully addressed, since it acts as weight for the measurements, i.e. providing more relevance to the measurements with smaller associated uncertainty and vice versa. A proper forward model associating the instrument measurements with the atmospheric state is needed, e.g. given a AH profile, what TB would the MWR measure. In the case of the MWR a forward model involving radiative transfer calculations is used. The lidars use simpler forward models, since RL raw data, i.e. photon counts, are not used, but products, i.e. mixing ratio or temperature profiles, are used instead.

With the proper definition of all these ingredients, the algorithm finds the optimal atmospheric state, i.e. the solution, using an iterative method based on Bayesian probability theory. A major advantage of using this method, is that it allows to define an a posteriori error (or theoretical error) associated to the retrieved solution. In addition, the information content assessment is feasible by means of parameters like the degrees of freedom per signal or the vertical resolution. All these parameters served to evaluate the LIME SOAP retrievals, highlighting the advantages of the MWR+lidar synergy.

The first application of LIME SOAP is the AH retrieval from the ground based perspective in clear sky scenarios during HOPE (chapter 4). To investigate the synergy advantages, LIME SOAP is applied to the complete HOPE period, i.e. a total of ~53 clear sky measurement hours. Statistical comparisons with RS, theoretical errors, DOF and vertical resolution, serve to demonstrate the optimal combination of the MWR and RL measurements. The results show that on average the AH uncertainty can be reduced up to 60% (38%) with respect to the retrieval using only-MWR (only-RL) data. In addition, IWV is calculated from the AH retrievals and compared to the IWV derived from GPS, showing that, though the RL is essential for AH profiling, it does not provide additional information on the IWV, which is already accurately provided by the MWR.

The T retrieval is also possible within LIME SOAP because both MWR and RL provide T information. Chapter 5 presents how these T and RH retrievals are performed in the ground based scenario. Due to the use of MWR brightness temperatures at multiple elevation angles, the MWR provides significant information below the lidar overlap region as shown by the degrees of freedom for signal. Because the T RL signal exhibits a large non-overlap region, i.e. the first usable height can vary from 500 up to 1700 m, the MWR+RL combination becomes an essential tool to provide complete information on T and RH. This affirmation is demonstrated by means of comparisons to RS, theoretical errors and DOF. For temperature, it is shown that the error is reduced by 47.1% (24.6%) with respect to the only-MWR (only-RL) profile, when comparing the retrievals to a radiosonde profile. In the RH retrieval, correlation between T and AH is included, which indicates improvements in the retrieved RH with respect to the case when T and AH

are calculated independently. In addition, and because the RL temperature data is often not available, a retrieval without RL T is performed. The result for the specific case study shows that the RL T is not essential for the T and RH retrievals and using only the MWR temperature information provides satisfactory results. Due to the restricted RL temperature data availability, the evaluation of the RH estimates is performed with a single case study. Because of that, a larger data set to deeper study the relative humidity retrievals could be desiderable.

Building on the AH, T and RH clear sky retrievals, an application for a simple cloudy case study is presented (chapter 6), where the synergy is expected to have the most important improvements as lidar is attenuated in the cloud. Additional information is required to implement the retrieval, e.g. the cloud base and top, which are taken from ceilometer and radar measurements respectively. Furthermore, the LWP is retrieved within the algorithm. Unfortunately, the evaluation of the retrieved AH, RH and T profiles with other independent measurements is not possible. Nevertheless, the results for the LWP retrieval are successful when compared to the LWP retrieved from MWR alone with a simple statistical method. In addition, the IWV is calculated from the retrieved AH profiles and used as consistency check. The resulting IWV is compared to GPS and IWV from MWR statistical retrieval, presenting standard deviations lower than 0.6 kg/m^2 for the both cases. For this specific study, the RL data has 5 minutes temporal resolution, which is coarse when investigating cloud formation processes. Using this temporal resolution for the lidar, but including the up to 1 second resolution MWR data, which captures the high liquid water variations, represents a strong advantage.

After the LIME SOAP application to the ground based scenario, the algorithm is applied to the airborne perspective of HALO (chapter 7). Because the available HALO MWR data is a very preliminary version, synthetic measurements (SM) are used to demonstrate the algorithm performance. LIME SOAP is applied for the T, AH and RH retrievals in the subtropical region using a priori information calculated from dropsondes. The results are evaluated with the same parameters than the previous LIME SOAP applications. From the airborne perspective, the lidar non-overlap region is situated in the upper troposphere, where the amount of water vapor is reduced. Thus, the MWR improvement in the blind lidar region has less impact than in the ground based scenario.

In general, the improvements of the synergy have been analyzed in terms of several parameters, like the reduction of the theoretical error and the vertical resolution, or the increase of DOF, showing significant advantages with respect to the two instruments working separately. The synergy presents its strongest advantages in the regions where lidar data is not available, i.e. non-overlap region, high background noise or cloudy scenarios, whereas in the regions where both instruments are available, the lidar dominates the retrieval. In addition, LIME SOAP can be used as data quality indicator because, in order to find convergence and once defined a proper a priori information, the measurements of the two sensors need to be consistent.

Outlook

The strongest advantages of the synergy MWR+lidar are found to be in cloudy situations, where the lidar presents limited vertical coverage. The cloudy scenario analyzed in chapter 6 presents only a simple case study. In this study, the cloud is a single layer water cloud and its top and base heights are taken from ceilometer and radar data, respectively. Further studies will be focused on the extension of LIME SOAP to more complex cloudy situations, e.g. multi-layer clouds. In addition, the current definition of the algorithm can be improved. For example, so far a vertically constant LWC is assumed in the cloud, but a more sophisticated liquid water distribution could be considered, specially for thicker clouds. A further improvement could be to retrieve the cloud base and cloud top, associating as uncertainty to these parameters the vertical resolution of the instruments used to detect the cloud boundaries. The improvement of LIME SOAP for cloudy applications can be of great help towards a better understanding of cloud phenomena.

In the LIME SOAP airborne application, there is also room for improvement. For example, as discussed in chapter 7, temperature inversions close to the surface are difficult to capture by the MWR. This can induce a large error in the calculations of the relative humidity in the boundary layer. A possible solution to improve this situation could be to use the closest DS profile as a priori x_a in the retrieval, instead of an average over all the clear sky DS. Nevertheless, this approach presents the challenge of defining a proper uncertainty estimate for x_a, which might not be straightforward. In addition, the sea surface temperature (SST) still represents a source of uncertainty in the retrieval. In chapter 7, the closest SST in time and space from reanalysis data has been used, which could lead to errors. A better approach could be to include the SST in LIME SOAP as a parameter to retrieve. However, the real challenge concerning the airborne perspective is the proper assessment of clouds. From ground base, the cloud boundary estimates are available at JOYCE. Nevertheless, the cloud base detection for low clouds from HALO can be an issue, since the radar has low sensitivity in the lowest atmosphere and in addition, might be affected by drizzle.

Additionally, due to the LIME SOAP flexible design, more instrument measurements could be incorporated to the retrieval algorithm, including a proper uncertainty and forward model definition, e.g. a radar, which could supply valuable information on cloud properties. This incorporations could help to provide a even more robust and complete picture of the atmospheric state.

Moreover, the expansion of the ground based network of atmospheric profiling stations will make possible the application of LIME SOAP at several sites under different climate conditions.

Bibliography

Adam, S., Schwitalla, T., Hammann, E., Behrendt, A., and Wulfmeyer, V.: Composite temperature profiles from Raman Lidar and Microwave Radiometer, in: 27th International Laser Radar Conference, 2015 New York, 2015.

Aires, F., Prigent, C., Orlandi, E., Milz, M., Eriksson, P., Crewell, S., Lin, C., and Kangas, V.: Microwave hyperspectral measurements for temperature and humidity atmospheric profiling from satellite: The clear-sky case, Journal of Geophysical Research: Atmospheres, 120, doi: 10.1002/2015JD023331, 2015.

Althausen, D., Müller, D., Ansmann, A., Wandinger, U., Hube, H., Clauder, E., and Zörner, S.: Scanning 6-wavelength 11-channel aerosol lidar, Journal of Atmospheric and Oceanic Technology, 17, 1469–1482, 2000.

Behrendt, A., Wulfmeyer, V., Hammann, E., Muppa, S. K., and Pal, S.: Profiles of second- to fourth-order moments of turbulent temperature fluctuations in the convective boundary layer: first measurements with rotational Raman lidar, Atmospheric Chemistry and Physics, 15, 5485–5500, doi:10.5194/acp-15-5485-2015, 2015.

Bevis, M., Businger, S., Herring, T. A., Rocken, C., Anthes, R. A., and Ware, R. H.: GPS meteorology: Remote sensing of atmospheric water vapor using the global positioning system, Journal of Geophysical Research: Atmospheres, 97, 15 787–15 801, doi:10.1029/92JD01517, 1992.

Bianco, L., Cimini, D., Marzano, F., and Ware, R.: Combining microwave radiometer and wind profiler radar measurements for high-resolution atmospheric humidity profiling, Journal of Atmospheric and Oceanic Technology, 22, 949–965, 2005.

Cimini, D., Westwater, E., and Gasiewski, A.: Temperature and Humidity Profiling in the Arctic Using Ground-Based Millimeter-Wave Radiometry and 1DVAR, Geoscience and Remote Sensing, IEEE Transactions on, 48, 1381–1388, doi:10.1109/TGRS.2009.2030500, 2010.

Crewell, S. and Löhnert, U.: Accuracy of Boundary Layer Temperature Profiles Retrieved With Multifrequency Multiangle Microwave Radiometry, Geoscience and Remote Sensing, IEEE

Transactions on, 45, 2195–2201, doi:10.1109/TGRS.2006.888434, 2007.

Crook, N. A.: Sensitivity of moist convection forced by boundary layer processes to low-level thermodynamic fields, Monthly Weather Review, 124, 1767–1785, 1996.

Deblonde, G. and English, S.: One-Dimensional Variational Retrievals from SSMIS-Simulated Observations, Journal of Applied Meteorology, 42, 1406–1420, doi:10.1175/1520-0450(2003)042<1406:OVRFSO>2.0.CO;2, 2003.

Dee, D. P., Uppala, S. M., Simmons, A. J., Berrisford, P., Poli, P., Kobayashi, S., Andrae, U., Balmaseda, M. A., Balsamo, G., Bauer, P., Bechtold, P., Beljaars, A. C. M., van de Berg, L., Bidlot, J., Bormann, N., Delsol, C., Dragani, R., Fuentes, M., Geer, A. J., Haimberger, L., Healy, S. B., Hersbach, H., Hólm, E. V., Isaksen, L., Kållberg, P., Köhler, M., Matricardi, M., McNally, A. P., Monge-Sanz, B. M., Morcrette, J.-J., Park, B.-K., Peubey, C., de Rosnay, P., Tavolato, C., Thépaut, J.-N., and Vitart, F.: The ERA-Interim reanalysis: configuration and performance of the data assimilation system, Quarterly Journal of the Royal Meteorological Society, 137, 553–597, doi:10.1002/qj.828, 2011.

Delanoe, J. and Hogan, R. J.: A variational scheme for retrieving ice cloud properties from combined radar, lidar, and infrared radiometer, Journal of Geophysical Research: Atmospheres, 113, n/a–n/a, doi:10.1029/2007JD009000, d07204, 2008.

Di Girolamo, P., Marchese, R., Whiteman, D. N., and Demoz, B. B.: Rotational Raman lidar measurements of atmospheric temperature in the UV, Geophysical Research Letters, 31, n/a–n/a, doi:10.1029/2003GL018342, l01106, 2004.

Di Girolamo, P., Summa, D., and Ferretti, R.: Multiparameter Raman Lidar Measurements for the Characterization of a Dry Stratospheric Intrusion Event, Journal of Atmospheric and Oceanic Technology, 26, 1742–1762, doi:10.1175/2009JTECHA1253.1, 2009.

Di Girolamo, P., Summa, D., Bhawar, R., Di Iorio, T., Cacciani, M., Veselovskii, I., Dubovik, O., and Kolgotin, A.: Raman lidar observations of a Saharan dust outbreak event: Characterization of the dust optical properties and determination of particle size and microphysical parameters, Atmospheric Environment, 50, 66–78, doi:10.1016/j.atmosenv.2011.12.061, 2012.

Dick, G., Gendt, G., and Reigber, C.: First experience with near real-time water vapor estimation in a German {GPS} network, Journal of Atmospheric and Solar-Terrestrial Physics, 63, 1295 – 1304, doi:http://dx.doi.org/10.1016/S1364-6826(00)00248-0, 2001.

Dunbar, T., Barlow, J., and Belcher, S.: An Optimal Inverse Method Using Doppler Lidar Measurements to Estimate the Surface Sensible Heat Flux, Boundary-layer meteorology, 150, 49–67, 2014.

Ebell, K., Orlandi, E., Hünerbein, A., Löhnert, U., and Crewell, S.: Combining ground-based with satellite-based measurements in the atmospheric state retrieval: Assessment of the information content, Journal of Geophysical Research: Atmospheres, 118, 6940–6956, doi:10.1002/jgrd.50548, 2013.

Foth, A., Baars, H., Di Girolamo, P., and Pospichal, B.: Water vapour profiles from Raman lidar

automatically calibrated by microwave radiometer data during HOPE, Atmospheric Chemistry and Physics, 15, 7753–7763, doi:10.5194/acp-15-7753-2015, 2015.

Gendt, G., Dick, G., Reigber, C., Tomassini, M., Liu, Y., and Ramatschi, M.: Near Real Time GPS Water Vapor Monitoring for Numerical Weather Prediction in Germany, Journal of the Meteorological Society of Japan. Ser. II, 82, 361–370, 2004.

Görsdorf, U., Lehmann, V., Bauer-Pfundstein, M., Peters, G., Vavriv, D., Vinogradov, V., and Volkov, V.: A 35-GHz Polarimetric Doppler Radar for Long-Term Observations of Cloud Parameters—Description of System and Data Processing, Journal of Atmospheric and Oceanic Technology, 32, 675–690, 2015.

Han, Y. and Westwater, E. R.: Analysis and improvement of tipping calibration for ground-based microwave radiometers, Geoscience and Remote Sensing, IEEE Transactions on, 38, 1260–1276, 2000.

Han, Y., Westwater, E. R., and Ferrare, R. A.: Applications of Kalman Filtering to Derive Water Vapor Profiles from Raman Lidar and Microwave Radiometers, Journal of Atmospheric and Oceanic Technology, 14, 480–487, doi:10.1175/1520-0426(1997)014<0480:AOKFTD>2.0.CO;2, 1997.

Heidinger, A. K. and Pavolonis, M. J.: Gazing at cirrus clouds for 25 years through a split window. Part I: Methodology, Journal of Applied Meteorology and Climatology, 48, 1100–1116, 2009.

Hewison, T.: 1D-VAR Retrieval of Temperature and Humidity Profiles From a Ground-Based Microwave Radiometer, Geoscience and Remote Sensing, IEEE Transactions on, 45, 2163–2168, doi:10.1109/TGRS.2007.898091, 2007.

Hoff, R. and Hardesty, R.: Thermodynamic profiling technologies workshop report to the National Science Foundation and the National Weather Service. NCAR Tech, Tech. rep., Note NCAR/TN-4881STR, 2012.

Illingworth, A., Hogan, R., O'connor, E., Bouniol, D., et al.: Cloudnet, Bulletin of the American Meteorological Society, 88, 883, 2007.

Janssen, M.: Atmospheric remote sensing by microwave radiometry, Wiley-interscience publication, Wiley, New York, 1993.

Klepp, C., Ament, F., Bakan, S., Hirsch, L., and Stevens, B.: NARVAL campaign report, Tech. rep., Max-Planck-Institut fur Meteorologie, 2014.

Koren, I., Remer, L. A., Kaufman, Y. J., Rudich, Y., and Martins, J. V.: On the twilight zone between clouds and aerosols, Geophysical Research Letters, 34, doi:10.1029/2007GL029253, l08805, 2007.

Küchler, N., Turner, D. D., LÃűhnert, U., and Crewell, S.: Calibrating Ground-Based Microwave Radiometers: Uncertainty and Drifts, Radio Science, pp. n/a–n/a, doi:10.1002/2015RS005826, 2015RS005826, 2016.

Liebe, H., Hufford, G., and Manabe, T.: A model for the complex permittivity of water at frequencies below 1 THz, International Journal of Infrared and Millimeter Waves, 12, 659–675,

doi:10.1007/BF01008897, 1991.

Liou, K.-N.: An Introduction to Atmospheric Radiation, Academic Press, Inc., United States of America, 1980.

Löhnert, U. and Crewell, S.: Accuracy of cloud liquid water path from ground-based microwave radiometry 1. Dependency on cloud model statistics, Radio Sci, 38, 8041, 2003.

Löhnert, U. and Maier, O.: Operational profiling of temperature using ground-based microwave radiometry at Payerne: prospects and challenges, Atmospheric Measurement Techniques Meas. Tech., 2012.

Löhnert, U., Crewell, S., and Simmer, C.: An integrated approach toward retrieving physically consistent profiles of temperature, humidity, and cloud liquid water, Journal of Applied Meteorology, 43, 1295–1307, 2004.

Löhnert, U., van Meijgaard, E., Baltink, H. K., Groß, S., and Boers, R.: Accuracy assessment of an integrated profiling technique for operationally deriving profiles of temperature, humidity, and cloud liquid water, Journal of Geophysical Research: Atmospheres, 112, doi:10.1029/2006JD007379, 2007.

Löhnert, U., Crewell, S., Krasnov, O., O'Connor, E., and Russchenberg, H.: Advances in Continuously Profiling the Thermodynamic State of the Boundary Layer: Integration of Measurements and Methods, Journal of Atmospheric and Oceanic Technology, 25, 1251–1266, doi:10.1175/2007JTECHA961.1, 2008.

Löhnert, U., Turner, D. D., and Crewell, S.: Ground-Based Temperature and Humidity Profiling Using Spectral Infrared and Microwave Observations. Part I: Simulated Retrieval Performance in Clear-Sky Conditions, Journal of Applied Meteorology and Climatology, 48, 1017–1032, doi:10.1175/2008JAMC2060.1, 2009.

Löhnert, U., Schween, J. H., Acquistapace, C., Ebell, K., Maahn, M., Barreraverdejo, M., Hirsikko, A., Bohn, B., Knaps, A., O'connor, E., Simmer, C., Wahner, A., and Crewell, S.: JOYCE: Jülich Observatory for Cloud Evolution, Bulletin of the American Meteorological Society, doi:10.1175/BAMS-D-14-00105.1, 2014.

Maschwitz, G., Löhnert, U., Crewell, S., Rose, T., and Turner, D. D.: Investigation of ground-based microwave radiometer calibration techniques at 530 hPa, Atmospheric Measurement Techniques, 6, 2641–2658, doi:10.5194/amt-6-2641-2013, 2013.

Masiello, G., Serio, C., and Antonelli, P.: Inversion for atmospheric thermodynamical parameters of IASI data in the principal components space, Quarterly Journal of the Royal Meteorological Society, 138, 103–117, doi:10.1002/qj.909, 2012.

Mech, M., Orlandi, E., Crewell, S., Ament, F., Hirsch, L., Hagen, M., Peters, G., and Stevens, B.: HAMP - the microwave package on the High Altitude and LOng range research aircraft (HALO), Atmospheric Measurement Techniques, 7, 4539–4553, doi:10.5194/amt-7-4539-2014, 2014.

Meunier, V., Turner, D. D., and Kollias, P.: On the Challenges of Tomography Retrievals of a

2D Water Vapor Field Using Ground-Based Microwave Radiometers: An Observation System Simulation Experiment, Journal of Atmospheric and Oceanic Technology, 32, 116–130, doi: 10.1175/JTECH-D-13-00194.1, 2015.

Miloshevich, L. M., Vömel, H., Paukkunen, A., Heymsfield, A. J., and Oltmans, S. J.: Characterization and correction of relative humidity measurements from Vaisala RS80-A radiosondes at cold temperatures, Journal of Atmospheric and Oceanic Technology, 18, 135–156, 2001.

Navas-Guzmán, F., Fernández-Gálvez, J., Granados-Muñoz, M. J., Guerrero-Rascado, J. L., Bravo-Aranda, J. A., and Alados-Arboledas, L.: Tropospheric water vapour and relative humidity profiles from lidar and microwave radiometry, Atmospheric Measurement Techniques, 7, 1201–1211, doi:10.5194/amt-7-1201-2014, 2014.

Petty, G. W.: A first course in Atmospheric Radiation. Second Edition, Sundog Publishing, United States of America, 2006.

Povey, A. C., Grainger, R. G., Peters, D. M., and Agnew, J. L.: Retrieval of aerosol backscatter, extinction, and lidar ratio from Raman lidar with optimal estimation, Atmospheric Measurement Techniques, 7, 757–776, doi:10.5194/amt-7-757-2014, 2014.

Rocken, C., Van Hove, T., and Ware, R.: Near real-time GPS sensing of atmospheric water vapor, Geophysical Research Letters, 24, 3221–3224, doi:10.1029/97GL03312, 1997.

Rodgers, C.: Inverse Methods for Atmospheric Sounding: Theory and Practice, World Scientific Publishing Company, Incorporated, Singapore, 2000.

Rose, T., Crewell, S., Löhnert, U., and Simmer, C.: A network suitable microwave radiometer for operational monitoring of the cloudy atmosphere, Atmospheric Research, 75, 183 – 200, doi:http://dx.doi.org/10.1016/j.atmosres.2004.12.005, cLIWA-NET: Observation and Modelling of Liquid Water Clouds, 2005.

Rosenkranz, P. W.: Water vapor microwave continuum absorption: A comparison of measurements and models, Radio Science, 33, 919–928, doi:10.1029/98RS01182, 1998.

Rothman, L., Jacquemart, D., Barbe, A., Chris Benner, D., Birk, M., Brown, L., Carleer, M., Chackerian, C. J., Chance, K., Coudert, L., Dana, V., Devi, V., Flaud, J.-M., Gamache, R., Goldman, A., Hartmann, J.-M., Jucks, K., Maki, A., Mandin, J.-Y., Massie, S., Orphal, J., Perrin, A., Rinsland, C., Smith, M., Tennyson, J., Tolchenov, R., Toth, R., Vander, J., Varanasi, P., and Wagner, G.: The *HITRAN* 2004 molecular spectroscopic database, Journal of Quantitative Spectroscopy and Radiative Transfer, 96, 139 – 204, doi:http://dx.doi.org/10.1016/j.jqsrt.2004.10.008, 2005.

Schneebeli, M.: Advancements in Ground-Based Microwave Remote Sensing of the Troposphere - Calibration, Data Retrieval and Applications, Ph.D. thesis, Philosophisch Naturwissenschaftliche Fakultät, Universität Bern, Bern, Switzerland, 2009.

Sica, R. J. and Haefele, A.: Retrieval of temperature from a multiple-channel Rayleigh-scatter lidar using an optimal estimation method, Appl. Opt., 54, 1872–1889, doi:10.1364/AO.54.001872, 2015.

Simmer, C.: Satellitenfernerkundung hydrologischer Parameter der Atmosphäre mit Mikrowellen, Verlag Dr. Kovac, Hamburg, 1994.

Solheim, F., Godwin, J. R., Westwater, E. R., Han, Y., Keihm, S. J., Marsh, K., and Ware, R.: Radiometric profiling of temperature, water vapor and cloud liquid water using various inversion methods, Radio Science, 33, 393–404, doi:10.1029/97RS03656, 1998.

Stankov, B. B.: Multisensor Retrieval of Atmospheric Properties, Bulletin of the American Meteorological Society, 79, 1835–1854, doi:10.1175/1520-0477(1998)079<1835:MROAP>2.0.CO;2, 1998.

Stankov, B. B., Gossard, E. E., Weber, B. L., Lataitis, R. J., White, A. B., Wolfe, D. E., Welsh, D. C., and Strauch, R. G.: Humidity Gradient Profiles from Wind Profiling Radars Using the NOAA/ETL Advanced Signal Processing System (SPS), Journal of Atmospheric and Oceanic Technology, 20, 3–22, doi:10.1175/1520-0426(2003)020<0003:HGPFWP>2.0.CO;2, 2003.

Steinke, S., Eikenberg, S., Löhnert, U., Dick, G., Klocke, D., Di Girolamo, P., and Crewell, S.: Assessment of small-scale integrated water vapour variability during HOPE, Atmospheric Chemistry and Physics Discussions, 14, 22 837–22 879, doi:10.5194/acpd-14-22837-2014, 2014a.

Steinke, S., Lohnert, U., Crewell, S., and Liu, S.: Water Vapor Tomography With Two Microwave Radiometers, IEEE Geoscience and Remote Sensing Letters, 11, 419–423, doi:10.1109/LGRS.2013.2264354, 2014b.

Stephens, G. L., Vane, D. G., Boain, R. J., Mace, G. G., Sassen, K., Wang, Z., Illingworth, A. J., O'Connor, E. J., Rossow, W. B., Durden, S. L., et al.: The CloudSat mission and the A-Train: A new dimension of space-based observations of clouds and precipitation, Bulletin of the American Meteorological Society, 83, 1771–1790, 2002.

Stevens, B. and Bony, S.: Water in the atmosphere, Physics Today, 66, 29, doi:http://dx.doi.org/10.1063/PT.3.2009, 2013.

Turner, D. D. and Löhnert, U.: Information Content and Uncertainties in Thermodynamic Profiles and Liquid Cloud Properties Retrieved from the Ground-Based Atmospheric Emitted Radiance Interferometer (AERI), Journal of Applied Meteorology and Climatology, 53, 752–771, doi:10.1175/JAMC-D-13-0126.1, 2014.

Turner, D. D., Clough, S. A., Liljegren, J. C., Clothiaux, E. E., Cady-Pereira, K. E., and Gaustad, K. L.: Retrieving Liquid Water Path and Precipitable Water Vapor From the Atmospheric Radiation Measurement (ARM) Microwave Radiometers, IEEE Transactions on Geoscience and Remote Sensing, 45, 3680–3690, doi:10.1109/TGRS.2007.903703, 2007.

Weitkamp, C.: Lidar. Range-Resolved Optical Remote Sensing of the Atmosphere, Springer, Singapore, 2005.

Whiteman, D. N.: Examination of the traditional Raman lidar technique. I. Evaluating the temperature-dependent lidar equations, Appl. Opt., 42, 2571–2592, doi:10.1364/AO.42.002571, 2003.

Wilks, D. S.: Statistical Method in the Atmospheric Sciences, Interational Geophysics Series, Elsevier, United States of America, 2006.

Wirth, M., Fix, A., Mahnke, P., Schwarzer, H., Schrandt, F., and Ehret, G.: The airborne multi-wavelength water vapor differential absorption lidar WALES: system design and performance, Applied Physics B, 96, 201–213, doi:10.1007/s00340-009-3365-7, 2009.

Wulfmeyer, V., Bauer, H.-S., Grzeschik, M., Behrendt, A., Vandenberghe, F., Browell, E. V., Ismail, S., and Ferrare, R. A.: Four-dimensional variational assimilation of water vapor differential absorption lidar data: The first case study within IHOP_2002, Monthly weather review, 134, 209–230, 2006.

Appendix

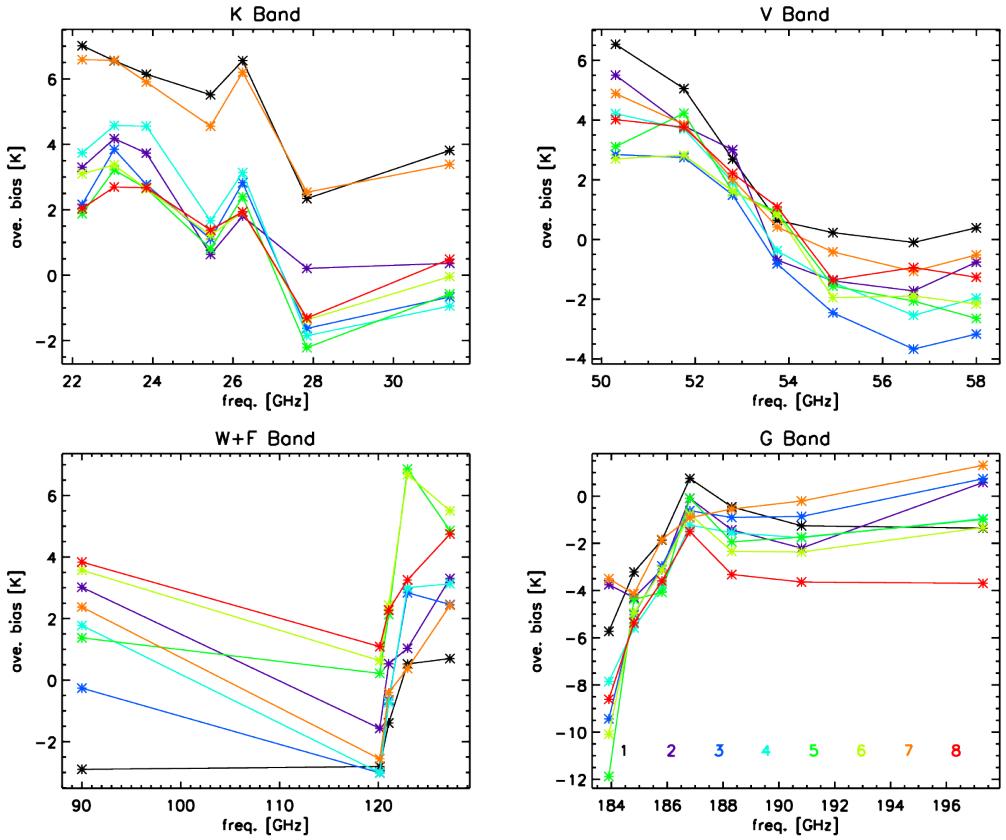

Figure 1: Provisional MWR bias for each channel, calculated with respect to the clear sky DS from preliminary MWR data version. Each color represents a research flight, from 1st to 8th.

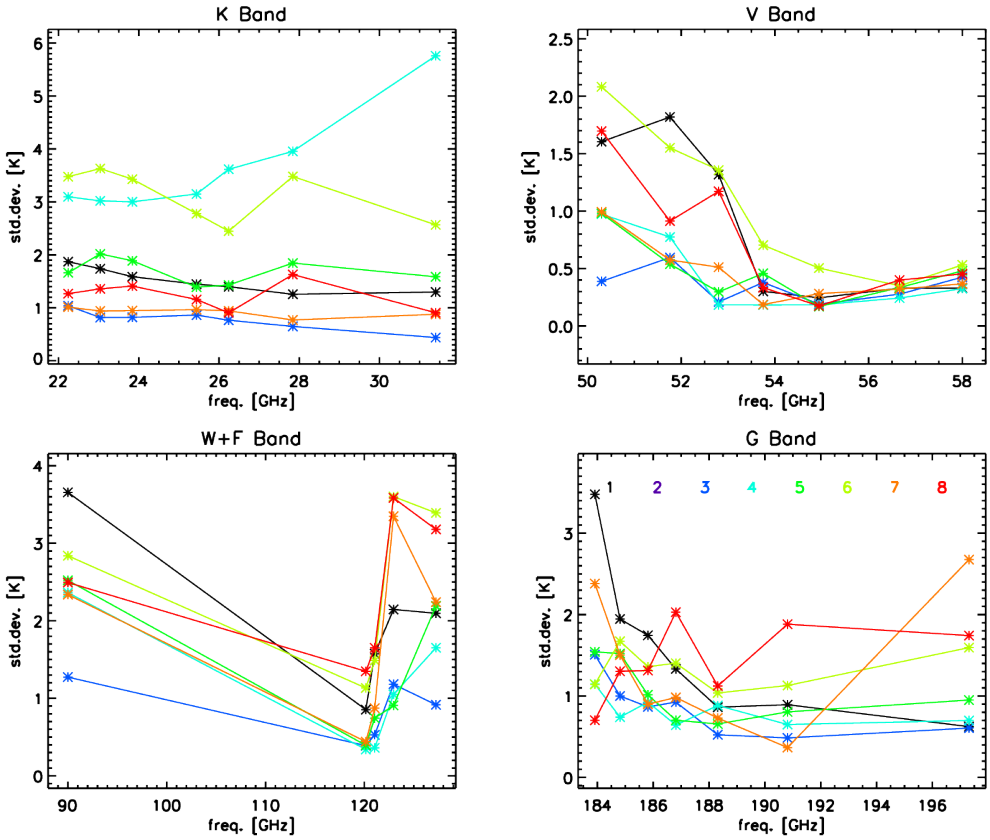

Figure 2: Provisional MWR standard deviation for each channel, calculated with respect to the clear sky DS from preliminary MWR data version. Each color represents a research flight, from 1st to 8th.

Erklärung

Ich versichere, dass ich die von mir vorgelegte Dissertation selbständig angefertigt, die benutzten Quellen und Hilfsmittel vollständig angegeben und die Stellen der Arbeit — einschließlich Tabellen, Karten und Abbildungen —, die anderen Werken im Wortlaut oder dem Sinn nach entnommen sind, in jedem Einzelfall als Entlehnung kenntlich gemacht habe; dass diese Dissertation noch keiner anderen Fakultät oder Universität zur Prüfung vorgelegen hat; dass sie — abgesehen von unten angegebenen Teilpublikationen — noch nicht veröffentlicht worden ist sowie, dass ich eine solche Veröffentlichung vor Abschluss des Promotionsverfahrens nicht vornehmen werde. Die Bestimmungen der Promotionsordnung sind mir bekannt. Die von mir vorgelegte Dissertation ist von Prof. Dr. Susanne Crewell betreut worden.

Köln, den 4.04.2016

María Barrera Verdejo

Teilveröffentlichungen

- Barrera-Verdejo, M., Crewell, S., Löhnert, U., Orlandi, E., and Di Girolamo, P.: Ground-based lidar and microwave radiometry synergy for high vertical resolution absolute humidity profiling, Atmos. Meas. Tech., 9, 4013-4028, doi:10.5194/amt-9-4013-2016, 2016.
- Barrera-Verdejo, M., Crewell, S., Löhnert, U., Orlandi, E., and Di Girolamo, P.: Ground based lidar and microwave radiometry synergy for high vertically resolved thermodynamic profiling, Atmos. Meas. Tech. Discuss., 8, 5467-5509, doi:10.5194/amtd-8-5467-2015, 2015.

About the author

Nov 6, 1986	Born in Granada, Spain
2002 - 2004	Scientific Lyceum, Granada, Spain Summa cum laude
2004 - 2010	Master degree in Telecommunications Engineering, University of Granada, Spain Master thesis " Pre-development of light sources for quantum cryptography "
2010 - 2012	Erasmus Mundus Master degree in Photonics Engineering, Nanophotonics and Biophotonics, Europhotonics partners Studies funded by *La Caixa* Master thesis " Characterization of a Push-Pull Membrane Mirror for an Astronomical Adaptive-Optics System " Summa cum laude
2012 - 2016	Marie E. Curie PhD student as part of the European project ITaRS, at University of Cologne

Acknowledgments

I would like to start giving thanks to my family: Jorge, Encarna and Marina. They gave me (and give me) all. They hug me when I need love and they give me their hands when I fall. Without their support, this thesis would not have been possible. Especial thanks also to my aunts Paqui and Jesus, who inspired me to have big dreams, and even more important, to trust in myself to achieve them. The two other inspiring people are Juan and Encarna. Without them, somethings in life would have no sense at all. Os debo simplemente todo.

A very big (huge) Danke to my dear supervisor Susanne, for her not only scientific support, but also personal one. Thanks to people like her, people like me live unforgettable opportunities. She is THE engine of ITaRS and Inferno. By now, she should know I admire her. Another huge Grazie is for *grande* Emiliano, who dedicated this thesis so much time and effort. Sei molto bravo, Emi, grazie dal cuore. Thanks also to my other supervisor Uli, for sparking me with his experience, wisdom and cookie stories. I feel thankful too with Bjorn Stevens and the people at the Max Planck Institute in Hamburg, who hosted me as guest researcher several times and foster interesting discussions on my research. I deeply appreciate the Marie S. Curie actions, which allowed this work by funding it and in addition, enriched my path with great people and opportunities.

Another XL thanks to our beautiful working group, counting with great people like Kerstin, Rainer, Max, Nils, Sarah, Mario, Sabrina, Cla, Stefan... You all make my days brighter, even when it is cloudy and grey outside. The same than my *familia colona*: I am so lucky to have you in my life! Cologne is more beautiful since you arrived. Thanks also to the Mexican zapatista coffee, the dishwasher in the kitchen and the cleaning staff, who ease (from the silence) our daily lives.

I could write and write saying thanks, because I feel deeply thankful. But I have to stop at some point. And I want to do it leaving *you* for the end. At the beginning of this journey, I encounter in my path one of the most wonderful persons I have ever met. I am so lucky that he accepted to accompany and support me all the way through. If needed, he was cook, comedian,

cheerleader, the cat I never had or shoulder. Everything. Jose, gracias por hacer este camino de la mano conmigo. Tenías razón: esto está guapísimo.